

JEEES

Journal of
Electromagnetic
Engineering and
Science

ISSN 2234-8409 (print)
ISSN 2234-8395 (online)

<http://www.jees.kr>

Volume 19, No. 1
January 2019



JEEES Journal of Electromagnetic Engineering and Science

EDITOR-IN-CHIEF

Sangwon Yun (Sogang University, Korea)
e-mail : swyun@sogang.ac.kr

DEPUTY EDITOR

HyunChul Ku (Konkuk University, Korea)
e-mail : hcku@konkuk.ac.kr

ASSOCIATE EDITORS

EunMi Choi (UNIST, Korea)
Haeng-Seon Lee (Sogang University, Korea)
Jong Won Yu (KAIST, Korea)
Jae-Young Chung
(Seoul National University of Science and Technology, Korea)
Kunio Sakakibara (Nagoya Institute of Technology, Japan)
Nader Behdad (University of Wisconsin, Madison, USA)
Sungtek Kahng (University of Incheon, Korea)
Yong Bae Park (Ajou University, Korea)
Yongshik Lee (Yonsei University, Korea)
Youngoo Yang (Sungkyunkwan University, Korea)
Youngwook Kim (California State University, Fresno, USA)

INTERNATIONAL ADVISORY BOARD

Ikuo Awai (Ryutech Corporation, Japan)
Bumman Kim (POSTECH, Korea)
Dong Chul Park (Chungnam National University, Korea)
John Volakis (Ohio State University, USA)
Huei Wang (National Taiwan University, Taiwan)
Robert Weigel
(Friedrich-Alexander-Universität, Erlangen-Nürnberg, Germany)
Ke Wu (Polytechnique Montréal, Canada)
Richard Ziolkowski (University of Arizona, USA)

EDITOR MEMBERS

ANTENNAS

Andrey K. Sarychev
(Moscow Institute of Physics and Technology, Russia)
Bierng-Chearl Ahn (Chungbuk Nat'l University, Korea)
Gyu-Je Sung (Hankyong Nat'l University, Korea)
Hae-Won Son (Chonbuk Nat'l University, Korea)
Ick-Jae Yoon (Chungnam Nat'l University, Korea)
Junho Yeo (Daegu University, Korea)

PASSIVE COMPONENTS AND CIRCUITS

Dal Ahn (Soonchunhyang University, Korea)
Juseop Lee (Korea University, Korea)
Kang Wook Kim (Kyungpook Nat'l University, Korea)
Truong Vu Bang Giang (Vietnam National University, Vietnam)
Cheng-Wei Qiu (National University of Singapore)

ACTIVE DEVICES AND DEVICE MODELING

Kris Kong (TriQuint Semiconductor, USA)
Shigeo Kawasaki (Japan Aerospace Exploration Agency, Japan)
Kyung Whan Yeom (Chungnam Nat'l University, Korea)
Tae-Yeoul Yun (Hanyang University, Korea)
Chan-Wang Park (Université du Québec à Rimouski, Canada)

RF/WIRELESS SYSTEM AND APPLICATIONS

Chun Sik Chae (NASA Jet Propulsion Laboratory, USA)
Pavel Nikitin (Intermec Technologies Corporation, USA)
Joong-Soo Lim (Baekseok University, Korea)
Sang-Min Han (Soonchunhyang University, Korea)
Seung Yeop Rhee (Chonnam Nat'l University, Korea)

THEORY AND NUMERICAL METHODS

Jay Kyoong Lee (Syracuse University, USA)
Kyung-Young Jung (Hanyang University, Korea)
Seung-Yeup Hyun (Jeju Nat'l University, Korea)
Yong-Heui Cho (Mokwon University, Korea)

ELECTROMAGNETIC INTERFERENCE/ COMPATIBILITY/ENVIRONMENT/MEASUREMENT

Tzong-Lin Wu (National Taiwan University, Taiwan)
Ic-Pyo Hong (Kongju Nat'l University, Korea)
Jae-Yong Kwon (KRISS, Korea)
Seungyoung Ahn (KAIST, Korea)
Tae Weon Kang (KRISS, Korea)

ETHICAL EDITOR

Dongho Kim (Sejong University, Korea)

STATISTICAL EDITOR

Youngje Sung (Kyonggi University, Korea)

MANUSCRIPT EDITOR

Il-Suek Koh (Inha University, Korea)

Aims and Scope

The Journal of Electromagnetic Engineering and Science (JEES) is an official English-language journal of the Korean Institute of Electromagnetic and Science (KIEES). This journal was launched in 2001 and has been published quarterly since 2003. It is currently registered with the National Research Foundation of Korea and also indexed in Scopus, CrossRef, EBSCO, DOI/Crossref, Google Scholar, and Web of Science Core Collection as Emerging Sources Citation Index (ESCI) journal. The objective of JEES is to publish academic as well as industrial research results and discoveries in electromagnetic engineering and science. The particular scope of the journal includes electromagnetic field theory and its applications; high frequency components, circuits, and systems; antennas; electromagnetic wave environments; and relevant industrial developments. In addition to the regular stream of contributed papers, the journal occasionally publishes special issues on specific topics of current interest, to promote a focused coverage of the selected topics. In addition, JEES regularly posts invited review papers by leading researchers in the relevant fields, which will provide an overview of various subjects from their own perspectives. The editors of JEES are aware of the importance of rapid publication for the delivery of new research results to its readers with minimum delay, and fully recognize the need for a short turnaround time. Manuscripts submitted to JEES take about 3–5 months from the initial submission to publication. This rapid process applies to all three types of manuscripts that JEES publishes: regular papers, letters, and invited papers. The publication of submitted manuscripts is subject to peer review, and the final decision by the Editor-in-Chief is regularly made based on three reviews from experts in the relevant area. This journal actively promotes research in electromagnetic wave-related engineering and sciences, and its ultimate aim is to benefit the global electromagnetic engineering and science community.

Subscription Information

JEES is published quarterly in January, April, July, and October. Full text PDF files are available at the official website (<http://www.jees.kr>).

The annual subscription rates for this journal are USD 230 for institutional members, USD 55 for regular members, USD 37 for associate members, and USD 28 for student members.

Published by
The Korean Institute of
Electromagnetic Engineering and Science

04376, #706 Totoo Valley, 217 Saechang-ro, Yongsan-gu, Seoul, Korea

Tel : +82-2-337-9666 / 332-9665

Fax : +82-2-6390-7550

<http://www.kiees.or.kr>

E-mail : kees@kiees.or.kr

Printed January 25, 2019
Published January 31, 2019

Printed by
Guhmok Publishing Company
Tel : +82-2-2277-3324
Fax : +82-2-2277-3390
E-mail : guhmok@guhmok.com

This is an Open-Access article distributed under the terms of the Creative Commons Attribution Non-Commercial License (<http://creativecommons.org/licenses/by-nc/4.0>) which permits unrestricted non-commercial use, distribution, and reproduction in any medium, provided the original work is properly cited.

@This paper meets the requirements of KS X ISO 9706, ISO 9706-1994 and ANSI/NISO Z.39.48-1992 (Permanence of Paper).

©Copyright The Korean Institute of Electromagnetic Engineering and Science. All Rights Reserved.

 KOFST

This journal was supported by the Korean Federation of Science and Technology Societies Grant funded by the Korean Government (MEST).

REGULAR PAPERS

Loop-Type Ground Radiation Antenna for a C-Shaped Ground Plane Hongkoo Lee · Zeeshan Zahid · Hyeongdong Kim	1
An IE-FFT Algorithm to Analyze PEC Objects for MFIE Formulation Seung Mo Seo	6
Estimation of Detection Performance for Vehicle FMCW Radars Using EM Simulations Sungjun Yoo · Hanjoong Kim · Gangil Byun · Hosung Choo	13
Wide and Dual-Band MIMO Antenna with Omnidirectional and Directional Radiation Patterns for Indoor Access Points Insu Yeom · Young Bae Jung · Chang Won Jung	20
Metaheuristic Optimization Techniques for an Electromagnetic Multilayer Radome Design Trung Kien Nguyen · In-Gon Lee · Obum Kwon · Yoon-Jae Kim · Ic-Pyo Hong	31
Dual-Band Circularly Polarized Stack-Ring Antenna Youngje Sung	37
Modified Wilkinson Power Divider Using Transmission Lines for Various Terminated Impedances and an Arbitrary Power Ratio Young-Chul Yoon · Young Kim	42
Toroidal-Shaped Coils for a Wireless Power Transfer System for an Unmanned Aerial Vehicle Jaehyoung Park · Jonghoon Kim · Yujun Shin · Bumjin Park · Won-Seok Kim · Seok-Jong Cheong · Seungyoung Ahn	48
Design Method for Negative Group Delay Circuits Based on Relations among Signal Attenuation Group Delay and Bandwidth Sehun Na · Youn-Kwon Jung · Bomson Lee	56
SFCFOS Uniform and Chebyshev Amplitude Distribution Linear Array Antenna for K-Band Applications Venkata Kishore Kothapudi · Vijay Kumar	64

Loop-Type Ground Radiation Antenna for a C-Shaped Ground Plane

Hongkoo Lee · Zeeshan Zahid · Hyeongdong Kim*

Abstract

In this study, optimum locations for a loop-type ground radiation antenna are evaluated for C-shaped ground planes of two different sizes. To achieve good radiation performance, the antenna needs to be located such that it couples with the dominant current mode of the ground plane. Antenna locations are proposed using the characteristic mode analysis of the ground planes. The measured bandwidths of the antennas at the proposed locations have more than twice the bandwidths of the cases in which the antennas are coupled with non-dominant modes. The operating frequency of the antennas is 2.45 GHz.

Key Words: Characteristic Mode, Ground Radiation Antenna, Radiation Efficiency.

I. INTRODUCTION

The increasing market demand for Internet of Things (IoT) devices has emphasized the need for high-performance antennas for small devices. The performance of an electrically small antenna is determined by its physical size [1]. To design a high-performance antenna on a small ground plane, the antenna should be effectively coupled with the dominant characteristic mode of the ground plane. The loop-type ground radiation antenna (GradiAnt) is a promising option for mobile devices [2, 3]. Previous literature mainly focused on rectangular-shaped ground planes in which the GradiAnt is coupled with the first-order mode. These antennas show good performance for a discontinuous square ring-shaped ground plane [4] in which the dominant mode is the second-order mode. The characteristic mode analysis of various ground plane shapes has been employed in efficient antenna designs [5, 6]. However, the application of the characteristic mode analysis in high-performance GradiAnt design still needs more attention.

In this study, the optimum location for a loop-type GradiAnt is evaluated for a C-shaped ground plane using the characteristic mode analysis. To demonstrate this technique, the locations of the GradiAnt are analyzed for two different C-shaped ground plane sizes. The effect of different antenna locations on the bandwidth and efficiency of the antenna is observed. The antenna location, where it effectively couples with the dominant ground mode, performs significantly better than the other location, where the antenna is coupled with the non-dominant mode. The simulation is conducted using a full wave simulator, and measured data are obtained in a $6\text{ m} \times 3\text{ m} \times 3\text{ m}$ three-dimensional cellular telecommunications and Internet association over the air chamber.

II. ANTENNA DESIGN AND OPERATING MECHANISM

The GradiAnt consists of a rectangular clearance $4\text{ mm} \times 7\text{ mm}$ in size. The feeding loop contains the feeding capacitor (C_f). The resonance capacitor (C_r) is used to control the operat-

Manuscript received November 29, 2017 ; Revised March 22, 2018 ; Accepted September 19, 2018. (ID No. 20171129-069J)

Department of Electronics and Computer Engineering, Hanyang University, Seoul, Korea.

*Corresponding Author: Hyeongdong Kim (e-mail: hdkim@hanyang.ac.kr)

This is an Open-Access article distributed under the terms of the Creative Commons Attribution Non-Commercial License (<http://creativecommons.org/licenses/by-nc/4.0>) which permits unrestricted non-commercial use, distribution, and reproduction in any medium, provided the original work is properly cited.

© Copyright The Korean Institute of Electromagnetic Engineering and Science. All Rights Reserved.

ing frequency of the antenna. Flame Retardant Type-4 (FR-4) ($\epsilon_r = 4.4$, $\tan\delta = 0.02$) with 1 mm thickness is used as a substrate material. Two C-shaped ground plane sizes are considered. The smaller C-shaped ground plane is 30 mm \times 50 mm in size with a 15 mm \times 20 mm empty space at the right edge. The larger C-shaped ground plane is 48 mm \times 80 mm in size with a 24 mm \times 32 mm empty space at the right edge. The geometries of the GradiAnt and the ground planes are shown in Fig. 1. The thickness of the patterns is 0.5 mm. Two GradiAnt locations on the ground plane are evaluated using the characteristic modes of the ground planes. One of the locations (P1) is the middle of the right edge of the ground plane, as shown in Fig. 1(a), and the other location (P2) is the middle of the left edge of the ground plane, as shown in Fig. 1(b).

The GradiAnt behaves as a magnetic coupler, and its radiation performance is attributed to its coupling with the ground plane. Based on the theory of characteristic modes, the total current J on the conducting body can be obtained through the following equation:

$$J = \sum_n \frac{\iiint (E_i \cdot J_n) d\tau}{1 + j\lambda_n} E_n, \quad (1)$$

where $\iiint (E_i \cdot J_n) d\tau$ is the coupling between the impressed field E_i and modal current J_n , and λ_n is the eigenvalue associated with the n^{th} characteristic current mode. λ_n is closely related to the resonance frequency and the radiation performance. The coupling becomes maximum at resonance, when λ_n approaches zero, as the denominator term becomes the smallest. According to Eq. (1), maximum coupling will be achieved if the antenna is located at the maximum current of the dominant ground mode. Moreover, the characteristic mode of the ground plane radiates effectively at resonance. Therefore, good radiation performance will be achieved if the antenna is coupled with the characteristic mode of the ground plane that is resonantly close to the operating frequency. The performance of the antenna at locations P1 and P2 is compared for both ground sizes. The characteristic modes of both ground planes are analyzed in a full wave simulator, and the eigenvalues of the first- and second-order modes of both ground planes are presented in Fig. 2. The resonant frequency of the first-order mode is 1.95 GHz at position 1 (P1), and it is close to the operating frequency of the antenna (2.4–2.5 GHz), making the denominator term of Eq. (1) small. The resonant frequency of the second-order mode is 4.79 GHz, which is far from the operating frequency of the antenna at position 2 (P2), thus making the denominator term of Eq. (1) large and the numerator term of Eq. (1) maximum. The performance of the antenna, coupled with the first- and second-order modes, is predicted on the basis of Eq. (1). According to this equation, the coupling of the antenna with the first-order mode is higher than that with the second order mode. Therefore, on the small C-shaped ground plane,

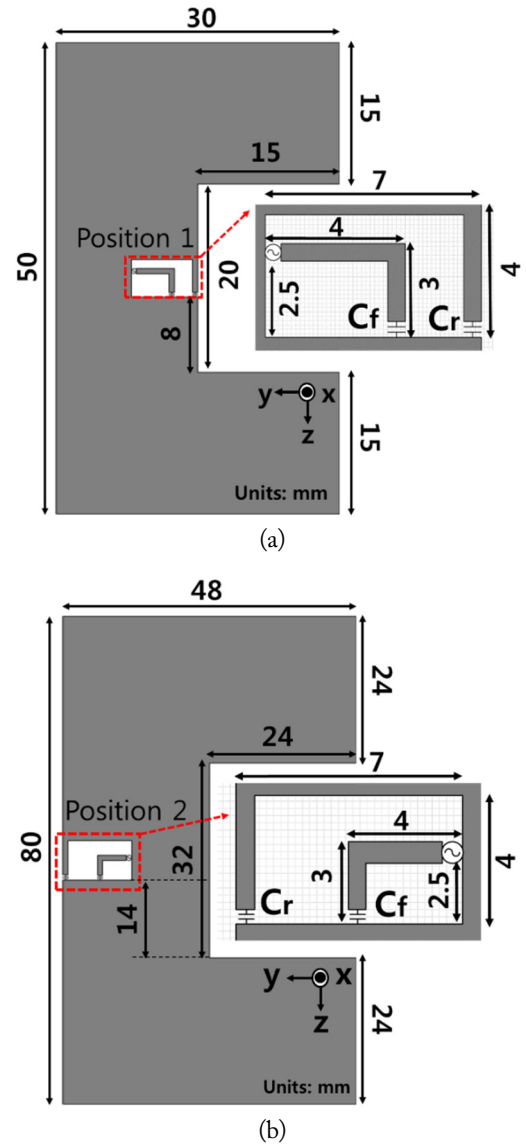


Fig. 1. Configuration of the proposed antenna on (a) a small and (b) a large C-shaped ground plane.

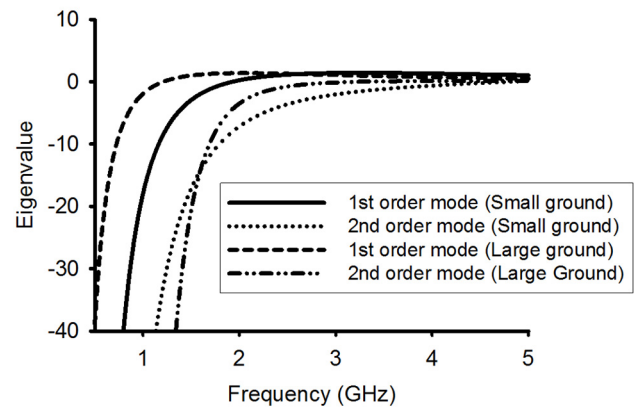


Fig. 2. Eigenvalues of the large and small C-shaped ground planes.

the radiation performance of the antenna at location P1 is expected to be higher than that at P2.

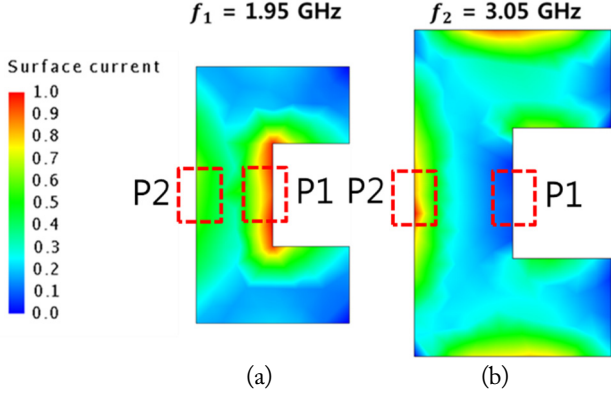


Fig. 3. Current distribution of the (a) small and (b) large C-shaped ground planes.

Conversely, at P1, the first-order mode of the larger ground plane is resonant at 1.23 GHz, which is far from the operating frequency of the antenna, thus making the denominator term of Eq. (1) large. At P2, the resonance frequency of the second-order mode is at 3.05 GHz, which is closer to the operating frequency, thus making the denominator term of Eq. (1) small. Therefore, on the large C-shaped ground plane, the radiation performance of the antenna at P2 is expected to be higher than that at P1.

To improve the radiation performance of the antenna, increasing the numerator term of Eq. (1) is important, and the location of the antenna is a crucial factor in determining the coupling. Therefore, the current distribution is analyzed to determine the position of the antennas. Fig. 3 shows the current distribution of the small and large C-shaped ground planes. The optimum locations for the antennas are decided on the basis of the reaction theorem, which has the characteristic of the current maximum [7].

III. SIMULATION AND EXPERIMENTAL RESULTS

To verify the performance at the proposed locations on the C-shaped ground planes, the designs are simulated and fabricated for measurement. The simulated and measured results are illustrated in Figs. 4 and 5.

Fig. 4 shows the results of the antenna on the small C-shaped ground plane. The simulated impedance bandwidth of the antenna at P1 is 470 MHz (2,260–2,730 MHz) and that at P2 is 230 MHz (2,330–2,560 MHz). The measured bandwidth of the antenna at P1 is 438 MHz (2,303–2,741 MHz) and that at P2 is 175 MHz (2,377–2,552 MHz). The measured results reveal that the bandwidth of the antenna at P1 is 2.5 times more than that at P2.

Fig. 5 shows the results of the antenna on the large C-shaped ground plane. The simulated impedance bandwidth of the antenna at P1 is 120 MHz (2,410–2,530 MHz) and that P2 is

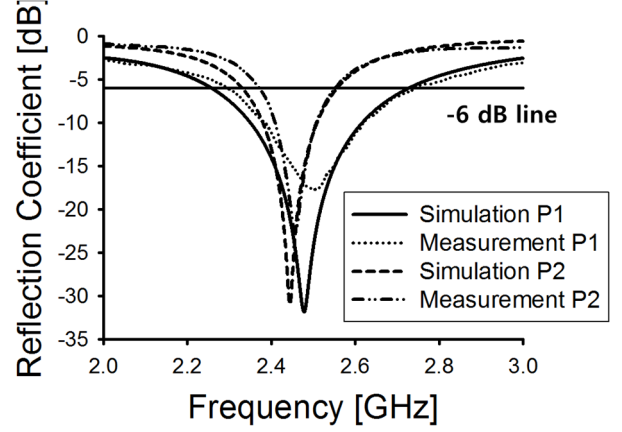


Fig. 4. Return loss characteristics of the small C-shaped ground plane.

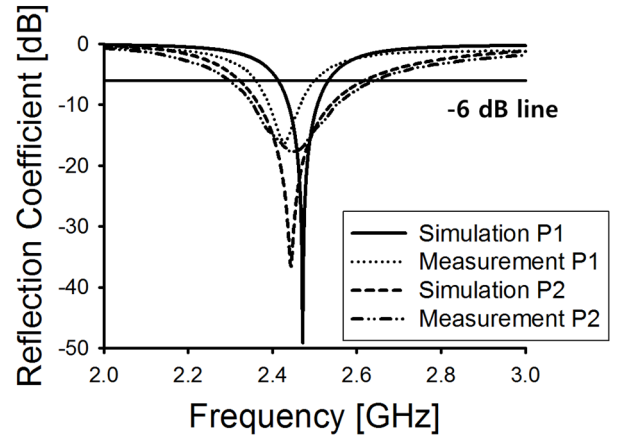


Fig. 5. Return loss characteristics of the large C-shaped ground plane.

300 MHz (2,320–2,620 MHz). The measured bandwidth of the antenna at P1 is 139 MHz (2,361–2,500 MHz) and that at P2 is 352 MHz (2,293–2,645 MHz). In this case, again the measured bandwidth of the antenna at P2 is approximately 2.5 times more than that at P1. Table 1 shows the measured and simulated efficiencies of the antennas. The measured and the simulated total radiation efficiencies of the antennas at P1 and P2 on the small C-shaped ground plane are 90.15%, 78.04%, 88.65%, and 80.00%, respectively. On the larger C-shaped ground plane, the measured and the simulated efficiencies at P1 and P2 are 76.52%, 87.97%, 68.30%, and 83.51% respectively. The measured and the simulated results indicate a significant

Table 1. Measured and simulated total radiation efficiencies of the antennas at P1 and P2 (unit: %)

Ground size	Position 1		Position 2	
	Measured	Simulated	Measured	Simulated
Small	90.15	88.65	78.04	80.00
Large	76.52	68.30	87.97	83.51

difference depending on the position of the antenna. This significant advantage in bandwidth and radiation efficiency verifies the suitability of the proposed antenna locations on the ground planes.

Fig. 6 shows the peak gain of the small and large C-shaped ground planes at P1 and P2. For the small ground plane, the average peak gain is higher at P1, and for the large ground, the average peak gain is also higher at P1. However, the radiation efficiency of the large ground plane is higher at P2 because of the lower directivity.

The measured radiation pattern of the small ground plane at P1 is illustrated in Fig. 7, and the measured radiation pattern of the large ground plane at P2 is presented in Fig. 8. The radiation pattern of the antenna placed at P1 in the case of the small ground plane and that placed at P2 in the case of large ground plane are illustrated because they have better radiation performance. Both antennas show omni-directional radiation patterns.

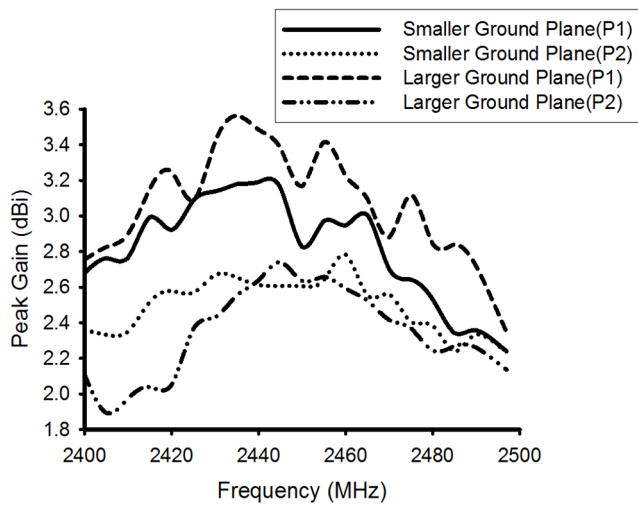


Fig. 6. Peak gain of the small and large C-shaped ground planes at P1 and P2.

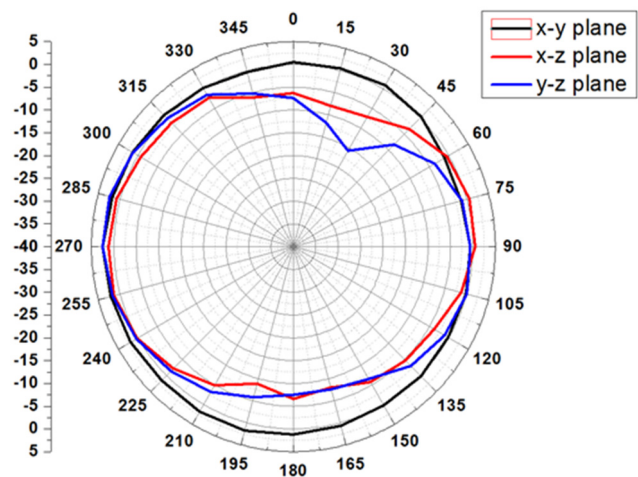


Fig. 7. Measured radiation pattern of the small ground plane at P1.

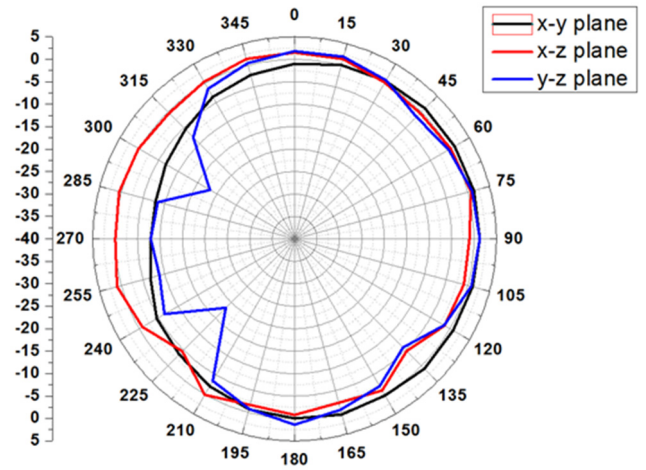


Fig. 8. Measured radiation pattern of the large ground plane at P2.

IV. CONCLUSION

In this study, the optimum location for a loop-type ground radiation antenna was proposed for C-shaped ground planes using the characteristic mode analysis. The simulations and measurements demonstrated that the antenna showed significantly better performance when located at the current maximum of the dominant mode of the ground plane. This analysis can be applied to small IoT devices to enhance the performance of the antenna.

This work was supported by the National Research Foundation of Korea grant funded by the Korean government (MSIP) (No. 2015R1A2A2A15055109).

REFERENCES

- [1] J. S. McLean, "A re-examination of the fundamental limits on the radiation Q of electrically small antenna," *IEEE Transactions on Antennas and Propagation*, vol. 44, no. 5, pp. 672–676, 1996.
- [2] Y. Liu, X. Lu, H. Jang, H. Choi, K. Jung, and H. Kim, "Loop-type ground radiation antenna using resonated loop feeding, intended for mobile devices," *Electronics Letters*, vol. 47, no. 7, pp. 426–427, 2011.
- [3] O. Cho, H. Choi, and H. Kim, "Loop-type ground radiation antenna using capacitor," *Electronics Letters*, vol. 47, no. 1, pp. 11–12, 2011.
- [4] Z. Zahid and H. Kim, "Loop-type ground radiation antenna for discontinuous ring-shaped ground plane," *Electronics Letters*, vol. 53, no. 12, pp. 760–762, 2017.
- [5] M. Cabedo-Fabres, E. Antonino-Daviu, A. Valero-Nogueira, and M. F. Bataller, "Theory of characteristic modes revisited: a contribution to the design of the antennas for

modern applications," *IEEE Transactions on Antennas and Propagation Magazine*, vol. 49, no. 5, pp. 52–68, 2007.

[6] I. Szini, A. Tatomirescu, and G. F. Pedersen, "On small terminal MIMO antennas, harmonizing characteristic modes

with ground plane Geometry," *IEEE Transactions on Antennas and Propagation*, vol. 63, no. 4, pp. 1487–1497, 2015.

[7] R. F. Harrington, *Time-Harmonic Electromagnetic Fields*. New York, NY: Wiley, 2001.

Hongkoo Lee



received his B.S., M.S., and Ph.D. degrees in electrical engineering from the Department of Electronics and Computer Engineering, Hanyang University, Seoul, Republic of Korea, in 2012, 2014, and 2018, respectively. He is currently working as a researcher at Samsung Electronics. His research interest is mobile antenna using the characteristic mode analysis.

Hyeongdong Kim (S'89-M'91)



was born in Kwang-ju, Republic of Korea. He received his B.S. and M.S. degrees from the Seoul National University, Seoul, Republic of Korea, in 1984 and 1986, respectively, and his Ph.D. degree from the University of Texas at Austin, in 1992. From May 1992 to February 1993, he was a Post-Doctoral Fellow at the University of Texas at Austin. In 1993, he worked as a professor at the Department of Electrical and Computer Engineering, Hanyang University, Seoul, Republic of Korea. His current research interest are various antenna theories and designs based on ground characteristic mode analysis, namely, wide-band, high-efficiency, circular polarization, MIMO, and high-sensitivity antennas.

Zeeshan Zahid



received his M.S. degree in electronics from Quaid-i-Azam University, Islamabad, Pakistan in 2006. He joined the National University of Sciences and Technology (NUST) as a lecturer and was promoted to assistant professor in 2012. He received the "Best Teacher of the Year" award in 2012. He received his Ph.D. degree from Hanyang University, South Korea, in 2017. Currently, he serves as an assistant professor at the Department of Electrical Engineering, College of Signals, NUST, Rawalpindi campus. His main research interests include high-efficiency antenna design for mobile devices, circularly polarized antennas for mobile devices, MIMO antennas, and ultra-wide band antennas.

An IE-FFT Algorithm to Analyze PEC Objects for MFIE Formulation

Seung Mo Seo*

Abstract

An IE-FFT algorithm is implemented and applied to the electromagnetic (EM) solution of perfect electric conducting (PEC) scattering problems. The solution of the method of moments (MoM), based on the magnetic field integral equation (MFIE), is obtained for PEC objects with closed surfaces. The IE-FFT algorithm uses a uniform Cartesian grid to apply a global fast Fourier transform (FFT), which leads to significantly reduce memory requirement and speed up CPU with an iterative solver. The IE-FFT algorithm utilizes two discretizations, one for the unknown induced surface current on the planar triangular patches of 3D arbitrary geometries and the other on a uniform Cartesian grid for interpolating the free-space Green's function. The uniform interpolation of the Green's functions allows for a global FFT for far-field interaction terms, and the near-field interaction terms should be adequately corrected. A 3D block-Toeplitz structure for the Lagrangian interpolation of the Green's function is proposed. The MFIE formulation with the IE-FFT algorithm, without the help of a preconditioner, is converged in certain iterations with a generalized minimal residual (GMRES) method. The complexity of the IE-FFT is found to be approximately $O(N^{1.5})$ and $O(N^{1.5}\log N)$ for memory requirements and CPU time, respectively.

Key Words: Fast Fourier Transform (FFT), Integral Equation (IE), Method of Moments (MoM).

I. INTRODUCTION

In this paper, we introduce a fast method of moments (MoM) [1] solution for three-dimensional (3D) perfect electric conducting (PEC) scattering problems. The electric field integral equation (EFIE) has been a popular choice. The solution derived from the EFIE has higher accuracy compared to that of the magnetic field integral equation (MFIE). However, the impedance matrix of MFIE has a better convergence rate when solved with an iterative solver. The traditional MoM solutions from the EFIE or MFIE suffer from prohibitive $O(N^2)$ complexities of memory requirements and CPU time to assemble the impedance matrix and perform the matrix-vector multiplication with an iterative matrix solver. For complex structures,

the convergence of the impedance matrix is a big issue. Many researchers are interested in the MFIE formulation having better accuracy [2, 3].

For electrically large problems, several fast algorithms have been developed to overcome these numerical complexities. Multilevel fast multipole method (MLFMM) [4] is the most powerful algorithm, which has $O(N)$ and $O(N\log N)$ complexities for memory and the matrix-vector multiplication time, respectively. However, it has a strong dependence on integral kernels. There are several algorithms that are less kernel-dependent. The algebraic methods, such as IE-QR [5] and adaptive cross approximation (ACA) [6], have been developed to compress merely the impedance matrix. From the physical point of view, there are equivalent source approximations and Green's function

Manuscript received March 15, 2018 ; Revised May 1, 2018 ; Accepted September 28, 2018. (ID No. 20180315-028J)

Agency for Defense Development, Daejeon, Korea.

*Corresponding Author: Seung Mo Seo (e-mail: seungmos@gmail.com)

This is an Open-Access article distributed under the terms of the Creative Commons Attribution Non-Commercial License (<http://creativecommons.org/licenses/by-nc/4.0>) which permits unrestricted non-commercial use, distribution, and reproduction in any medium, provided the original work is properly cited.

© Copyright The Korean Institute of Electromagnetic Engineering and Science. All Rights Reserved.

approximations, which are both employed on a uniform Cartesian grid. Among the equivalent source approximation methods, the precorrected fast Fourier transform (p-FFT) [7] and the adaptive integral method (AIM) [8] are the most well-known algorithms.

This paper extends an IE-FFT algorithm [9] into the MFIE formulation for 3D PEC geometries with closed surfaces. The IE-FFT algorithm uses algebraically simple Lagrange polynomials for the free-space Green's function on a Cartesian grid. Through separation variables, the gradient of the Green's function consists of one coefficient matrix and two $\mathbf{\Pi}$ matrices; one is for the integrand of the product of the curl of the basis functions and Lagrange polynomials, and the other is for the integrand of the cross-product of the basis functions and the gradient of the Lagrange polynomials. This results in a non-symmetric MFIE formulation. The proposed algorithm leads to $O(N^{1.5})$ complexity for the memory requirement and $O(N^{1.5}\log N)$ complexity for the matrix-vector multiplication. Even though the MFIE has an accuracy problem, it can yield reliable solutions with careful treatment.

This paper is organized as follows. Section II provides a description of the MFIE formulation. The detailed implementation of the IE-FFT algorithm is described in Section III. Through numerical examples, Section IV demonstrates the accuracy and performance of the proposed method. Finally, the paper is concluded in Section V.

II. MFIE FORMULATION

The MFIE formulation is briefly shown for an arbitrarily shaped 3D PEC object. The formulation is directly used in the computation of the near-field correction for the IE-FFT algorithm to ensure its accuracy. The MFIE formulation can be written from the boundary condition for the tangential magnetic field on closed surfaces as

$$\begin{aligned} \hat{n} \times \vec{H}_{inc}(\vec{r}) &= \frac{1}{2} \vec{J}_h(\vec{r}) - \hat{n} \times \int_{\Gamma_h} \nabla g(\vec{r}; \vec{r}') \times \vec{J}_h(\vec{r}') d\Gamma' \\ &= \frac{1}{2} \vec{J}_h(\vec{r}) - \hat{n} \times \int_{\Gamma_h} \vec{J}_h(\vec{r}') \times \nabla' g(\vec{r}; \vec{r}') d\Gamma' \end{aligned} \quad (1)$$

To begin with, the discrete Galerkin statement for MFIE is shown below:

$$\begin{aligned} \text{Find } \vec{J}_h(\vec{r}) \in \mathbf{X}_h \subset \mathbf{H}_{\parallel}^{-1/2}(\mathbf{div}_{\Gamma}; \Gamma) \text{ such that} \\ \frac{1}{2} \int_{\Gamma_h} \vec{\lambda}_h(\vec{r}) \cdot \vec{J}_h(\vec{r}) d\Gamma \\ - \int_{\Gamma_h} (\vec{\lambda}_h(\vec{r}) \times \hat{n}) \cdot \int_{\Gamma_h} \vec{J}_h(\vec{r}') \times \nabla' g(\vec{r}; \vec{r}') d\Gamma' d\Gamma \\ = \int_{\Gamma_h} \vec{\lambda}_h(\vec{r}) \cdot [\hat{n} \times \vec{H}_{inc}(\vec{r})] d\Gamma \quad \forall \vec{\lambda}_h \in \mathbf{X}_h, \end{aligned} \quad (2)$$

where Γ_h denotes the faceted surface of the PEC object, \mathbf{X}_h is the finite dimensional trial and testing space, and $\vec{\lambda}(\vec{r})$ is the discrete Galerkin testing function.

$\mathbf{H}_{\parallel}^{-1/2}(\mathbf{div}_{\Gamma}; \Gamma) = \left\{ \vec{v} \mid \vec{v} \in (L^2(\Gamma))^2, \mathbf{div}_{\Gamma} \vec{v} \in L^2(\Gamma) \right\}$ is the correct spaces where an unknown current resides. \vec{r} and \vec{r}' are observation and source points, respectively, and $\vec{H}^{inc}(\vec{r})$ represents the incident magnetic field. In the present application, the free-space Green's function, $g(\vec{r}; \vec{r}') = \frac{e^{-jk_0|\vec{r}-\vec{r}'|}}{4\pi|\vec{r}-\vec{r}'|}$, is considered. For the traditional MoM, Eq. (2) could be expressed as

$$\begin{aligned} \frac{1}{2} \int_{\Gamma_h} \vec{\lambda}_h(\vec{r}) \cdot \vec{J}_h(\vec{r}) d\Gamma \\ - \int_{\Gamma_h} (\vec{\lambda}_h(\vec{r}) \times \hat{n}) \cdot \int_{\Gamma_h} (\vec{J}_h(\vec{r}') \times \hat{R}) \left(jk_0 + \frac{1}{R} \right) g(\vec{r}; \vec{r}') d\Gamma' d\Gamma \\ = \int_{\Gamma_h} \vec{\lambda}_h(\vec{r}) \cdot [\hat{n} \times \vec{H}_{inc}(\vec{r})] d\Gamma \end{aligned} \quad (3)$$

The unknown current density induced on the surface is

$$\vec{J}_h(\vec{r}') = \sum_{i=0}^{N-1} J_i \vec{\alpha}_i(\vec{r}'), \quad (4)$$

where $\vec{\alpha}_i(\vec{r})$ represents surface div-conforming Rao-Wilton-Glisson (RWG) vector basis functions [10]. The entries of the impedance matrix, \mathbf{Z} , are given by

$$Z_{ij} = \frac{1}{2} D_{ij} - P_{ij}, \quad 0 \leq i, j \leq N-1 \quad (5)$$

where

$$\begin{aligned} D_{ij} &= \frac{1}{2} \int_{\text{supp}(\vec{\alpha}_i)} \vec{\alpha}_i(\vec{r}) \cdot \vec{\alpha}_j(\vec{r}) d\Gamma \\ P_{ij} &= \int_{\text{supp}(\vec{\alpha}_i)} (\vec{\alpha}_i(\vec{r}) \times \hat{n}_i) \cdot \int_{\text{supp}(\vec{\alpha}_j)} \vec{\alpha}_j(\vec{r}') \times \nabla' g(\vec{r}; \vec{r}') d\Gamma' d\Gamma \end{aligned} \quad (6)$$

and

$$V_i = \int_{\text{supp}(\vec{\alpha}_i)} \vec{\alpha}_i(\vec{r}) \cdot [\hat{n} \times \vec{H}^{inc}(\vec{r})] d\Gamma, \quad (7)$$

where N is the number of unknowns; note that $\text{supp}()$ indicates the finite support of every non-boundary, edge-related basis function. Here, D_{ij} and P_{ij} are singular and coupling entries of the impedance matrix from the discrete Galerkin statement.

III. IE-FFT ALGORITHM

The IE-FFT algorithm makes a hexahedron bounding box that encloses the entire geometry in Fig. 1. A non-uniform triangular mesh for the RWG basis functions and a uniform Cartesian grid for the free-space Green's functions are shown in

two discretizations. Note that α is a constant used to define the near-field correction region, and λ is the wavelength. d is the sampling resolution. Here, L is the size of the second order Cartesian element.

The details of the IE-FFT algorithm are shown below.

1. A Uniform Cartesian Representation of Free-Space Green's Function using Lagrange Polynomials

The free-space Green's function is written in the matrix form:

$$g(\vec{r}; \vec{r}') = (\boldsymbol{\beta}(\vec{r}))^T \cdot \mathbf{G} \cdot \boldsymbol{\beta}(\vec{r}'), \quad (8)$$

where

$$\boldsymbol{\beta}(\vec{r}) = \begin{bmatrix} \beta_0^p(\vec{r}) & \beta_1^p(\vec{r}) & \cdots & \beta_{N_g-1}^p(\vec{r}) \end{bmatrix} \\ = \begin{bmatrix} \beta_0^p(x) \beta_0^p(y) \beta_0^p(z) \\ \beta_1^p(x) \beta_0^p(y) \beta_0^p(z) \\ \vdots \\ \beta_{N_g-1}^p(x) \beta_{N_g-1}^p(y) \beta_{N_g-1}^p(z) \end{bmatrix}^T, \quad (9)$$

$$\mathbf{G} = \begin{bmatrix} g_{0,0} & g_{0,1} & \cdots & g_{0,N_g} \\ g_{1,0} & g_{1,1} & \cdots & g_{1,N_g} \\ \vdots & \vdots & \ddots & \vdots \\ g_{N_g,0} & g_{N_g,1} & \cdots & g_{N_g,N_g} \end{bmatrix}, \quad (10)$$

and where the number of grid points is $N_g = N_x \times N_y \times N_z$. Also, the dimensional indices could be expressed as $n = (i, j, k)$ and $n' = (i', j', k')$, where $0 \leq i, i' < N_x$, $0 \leq j, j' < N_y$, and $0 \leq k, k' < N_z$. The p^{th} order interpolation basis functions, β_n^p , are the 3D tensor products form of the one-dimensional piecewise Lagrange polynomials on a Cartesian grid:

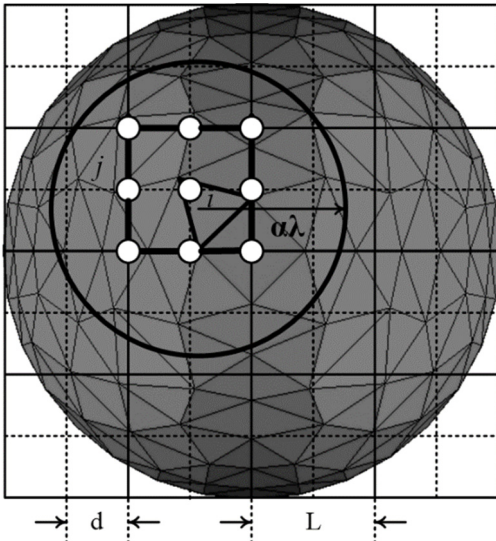


Fig. 1. Two discretizations for unknown current density and the free-space Green's function.

$$\beta_n^p(\vec{r}) = \beta_i^p(x) \cdot \beta_j^p(y) \cdot \beta_k^p(z). \quad (11)$$

The entries of \mathbf{G} are the 3D block-Toeplitz matrix. Combined with Eqs. (6) and (8),

$$P_{ij} \approx \int_{\text{supp}(\vec{\alpha}_i)} (\vec{\alpha}_i(\vec{r}) \times \hat{n}_i) \cdot \int_{\text{supp}(\vec{\alpha}_j)} \vec{\alpha}_j(\vec{r}') \\ \times \nabla' \left[\sum_{n=0}^{N_g-1} \sum_{n'=0}^{N_g-1} \beta_n^p(\vec{r}) g_{n,n'} \beta_{n'}^p(\vec{r}') \right] d\Gamma' d\Gamma, \quad (12)$$

where $g_{n,n'}$ is the Lagrange coefficients of the free-space Green's function. Interchanging summation and integration orders leads to

$$P_{ij} \approx \sum_{n=0}^{N_g-1} \sum_{n'=0}^{N_g-1} \int_{\text{supp}(\vec{\alpha}_i)} [(\vec{\alpha}_i(\vec{r}) \times \hat{n}_i) \beta_n^p(\vec{r})] d\Gamma \cdot g_{n,n'} \\ \cdot \int_{\text{supp}(\vec{\alpha}_j)} (\vec{\alpha}_j(\vec{r}') \times \nabla' \beta_{n'}^p(\vec{r}')) d\Gamma' \quad (13)$$

2. Representation of the $\bar{\mathbf{\Pi}}$ Matrices

There are two projection matrices needed in the IE-FFT. They are:

$$\bar{\mathbf{\Pi}}_A = \int_{\Gamma} \begin{bmatrix} \vec{\alpha}_0(\vec{r}) \times \hat{n}_0 \\ \vec{\alpha}_1(\vec{r}) \times \hat{n}_1 \\ \vdots \\ \vec{\alpha}_{N-1}(\vec{r}) \times \hat{n}_{N-1} \end{bmatrix} \begin{bmatrix} \beta_0^p(\vec{r}) & \beta_1^p(\vec{r}) & \cdots & \beta_{N_g-1}^p(\vec{r}) \end{bmatrix} d\Gamma \quad (14)$$

and

$$\bar{\mathbf{\Pi}}_P = \int_{\Gamma} \begin{bmatrix} \vec{\alpha}_0(\vec{r}) \\ \vec{\alpha}_1(\vec{r}) \\ \vdots \\ \vec{\alpha}_{N-1}(\vec{r}) \end{bmatrix} \times \begin{bmatrix} \nabla \beta_0^p(\vec{r}) & \nabla \beta_1^p(\vec{r}) & \cdots & \nabla \beta_{N_g-1}^p(\vec{r}) \end{bmatrix} d\Gamma, \quad (15)$$

respectively. In contrast to Eq. (3), $\nabla' g(\vec{r}; \vec{r}')$ only depends on the Lagrange polynomials, i.e., $\nabla' \beta_n^p(\vec{r}')$. The gradient of the 3D tensor product, $\nabla \beta_n^p(\vec{r})$, is expressed in

$$\nabla \beta_n^p(\vec{r}) = \hat{x} \{ \nabla_x \beta_n^p(\vec{r}) \} + \hat{y} \{ \nabla_y \beta_n^p(\vec{r}) \} + \hat{z} \{ \nabla_z \beta_n^p(\vec{r}) \}, \quad (16)$$

where

$$\nabla_x \beta_n^p(\vec{r}) = \frac{\beta_i^p(x)}{\partial x} \cdot \beta_j^p(y) \cdot \beta_k^p(z) \\ \nabla_y \beta_n^p(\vec{r}) = \beta_i^p(x) \cdot \frac{\beta_j^p(y)}{\partial y} \cdot \beta_k^p(z) \cdot \\ \nabla_z \beta_n^p(\vec{r}) = \beta_i^p(x) \cdot \beta_j^p(y) \cdot \frac{\beta_k^p(z)}{\partial z} \quad (17)$$

The entries of $\bar{\mathbf{\Pi}}_P$ are

$$\begin{aligned}
 \bar{\Pi}_p^{i,n} &= \int_{\Gamma} \bar{\alpha}_i(\vec{r}) \times \nabla \beta_n^p(\vec{r}) d\Gamma \\
 &= \hat{x} \left\{ \int_{\Gamma} [\bar{\alpha}_{i,y}(\vec{r}) \cdot \nabla_z \beta_n^p(\vec{r}) - \bar{\alpha}_{i,z}(\vec{r}) \cdot \nabla_y \beta_n^p(\vec{r})] d\Gamma \right\}, \\
 &+ \hat{y} \left\{ \int_{\Gamma} [\bar{\alpha}_{i,z}(\vec{r}) \cdot \nabla_x \beta_n^p(\vec{r}) - \bar{\alpha}_{i,x}(\vec{r}) \cdot \nabla_z \beta_n^p(\vec{r})] d\Gamma \right\} \\
 &+ \hat{z} \left\{ \int_{\Gamma} [\bar{\alpha}_{i,x}(\vec{r}) \cdot \nabla_y \beta_n^p(\vec{r}) - \bar{\alpha}_{i,y}(\vec{r}) \cdot \nabla_x \beta_n^p(\vec{r})] d\Gamma \right\} \quad (18)
 \end{aligned}$$

where $\bar{\alpha}_{i,x}(\vec{r})$, $\bar{\alpha}_{i,y}(\vec{r})$, and $\bar{\alpha}_{i,z}(\vec{r})$ are the vectors of the RWG basis function at the x -, y -, z -directions, respectively. Note that $\bar{\Pi}_p$ is a vector-valued and sparse matrix.

3. Near-Field Correction

In Fig. 1, the near-field interaction terms within $\alpha\lambda$ should be appropriately corrected to guarantee the accuracy. The correction entries are given as:

$$Z_{ij}^{corr} = Z_{ij}^{MoM} + (\bar{\Pi}_A)_{iI} G_{IJ} (\bar{\Pi}_P)_{Jj}^T, \quad (19)$$

where $0 \leq i < N$, $j \in L_{neig}$, and L_{neig} comprise the set of the near-field interaction elements.

4. Fast Matrix Vector Multiplication

$$\begin{aligned}
 \mathbf{y} &= \mathbf{Z}^{corr} \cdot \mathbf{x} \\
 &= \bar{\Pi}_A \cdot IFFT \left\{ FFT(\overline{\mathbf{G}_A}) \cdot FFT((\bar{\Pi}_P)^T \cdot \mathbf{x}) \right\}. \quad (20)
 \end{aligned}$$

The complexities of the \mathbf{Z}^{corr} and $\bar{\Pi}$ matrices concerning the memory requirements and the matrix fill-in time are $O(N)$. With the help of the FFT, the complexity of the matrix-vector multiplication of the \mathbf{G} matrix leads to $O(N^{1.5} \log N)$. The memory requirement of the \mathbf{G} matrix is $O(N^{1.5})$.

IV. NUMERICAL RESULTS

To demonstrate the efficiency of the proposed algorithm, a PEC sphere with a radius of 1.0 m is considered. The geometry of the PEC sphere is shown in Fig. 2. The triangular meshes

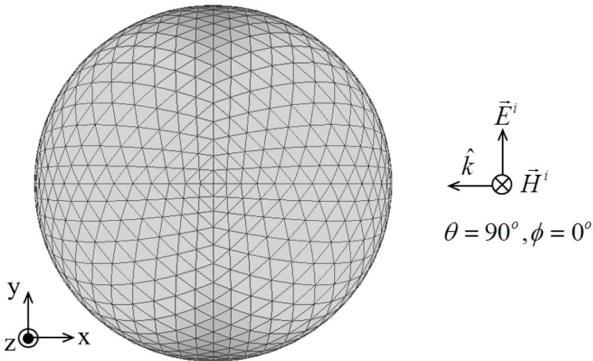


Fig. 2. The geometry of a PEC sphere.

are built so that there are at least $\lambda/7$. All numerical experiments are carried out on a 2 GB RAM Intel Pentium M processor 1.60 GHz. All computations have been performed in single precision arithmetic. Third-order Lagrange polynomials are used to interpolate the free-space Green's function.

The results of the IE-FFT algorithm with the MFIE formulation are compared to those of the Mie series. Fig. 3 shows the results of the bistatic RCS at a frequency of 300 MHz. Three results of the Mie series, the conventional MoM, and the proposed approach are compared. In Fig. 3(a), the results between the Mie series and the MoM approaches are seen to be slightly different around 180° . However, the results between the traditional MoM and the IE-FFT algorithm have very good agreements on both the E-plane and the H-plane. Inaccuracy comes from the numerical integration in the hyper-singular part. The IE-FFT algorithm does not deteriorate the accuracy. The results of the bistatic RCS at a frequency of 600 MHz are shown in Fig. 4. The results from the Mie series and the IE-FFT algorithm also have reasonable agreements on both the E-plane and the H-plane. The largest difference between the two results is obtained around 160° – 180° from the effects of the numerical integration. Fig. 5 shows the results of bistatic RCS at a frequency of 1,200 MHz. Both results are reasonable agreements.

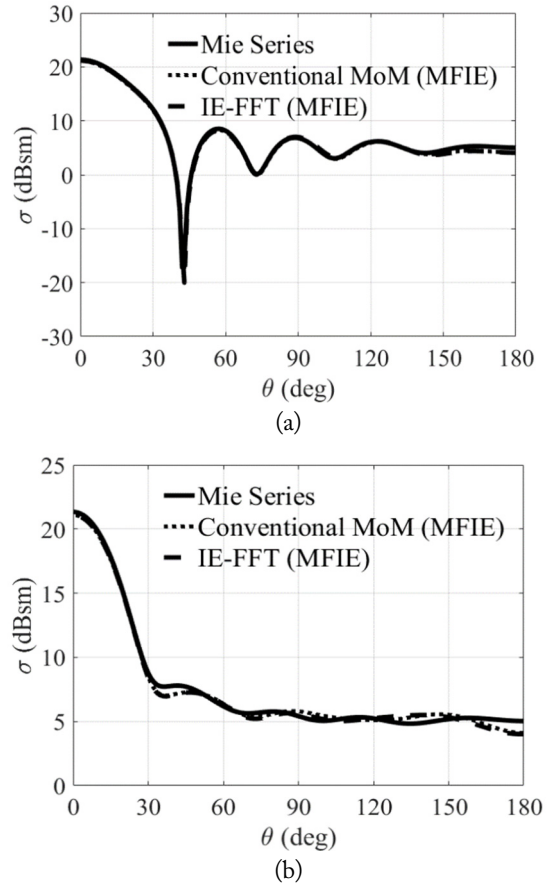


Fig. 3. The bistatic RCS for a 1-m PEC sphere at a frequency of 300 MHz. (a) E-plane and (b) H-plane.

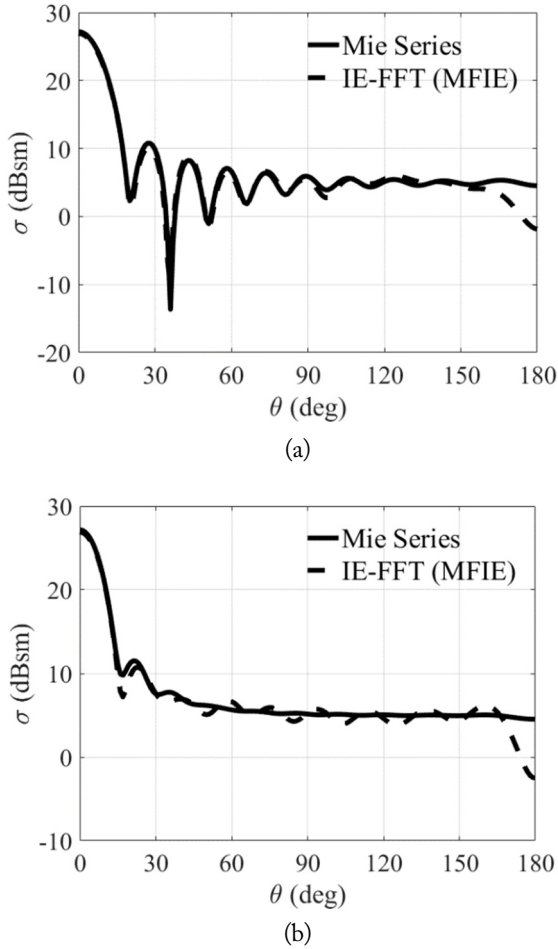


Fig. 4. The bistatic RCS for a one-meter PEC sphere at a frequency of 600 MHz. (a) E-plane and (b) H-plane.

Table 1 summarizes the memory requirements of the IE-FFT algorithm for third-order Lagrange polynomials. All units are Megabytes. The memory of the correction matrix, \mathbf{Z}^{corr} , and the $\mathbf{\Pi}$ matrices shows $O(N)$ complexity. However, the coefficient of the free-space Green's function is $O(N^{1.5})$ complexity.

Table 2 summarizes the CPU time and the number of iterations of the IE-FFT algorithm with third-order Lagrange polynomials. The CPU time for the matrices fill-in has $O(N)$ complexity. The CPU time for the matrix vector multiplication (MXV) is $O(N^{1.5}\log N)$ complexity.

Table 1. Memory requirement of the IE-FFT algorithm for scattering from a PEC sphere with a radius of 1 m

Freq. (MHz)	N	\mathbf{Z}^{corr}	$\bar{\mathbf{\Pi}}_A + \bar{\mathbf{\Pi}}_P$	\mathbf{G}
300	3,072	22	11	0.26
600	12,288	90	42	2.10
1,200	49,152	365	169	16.78

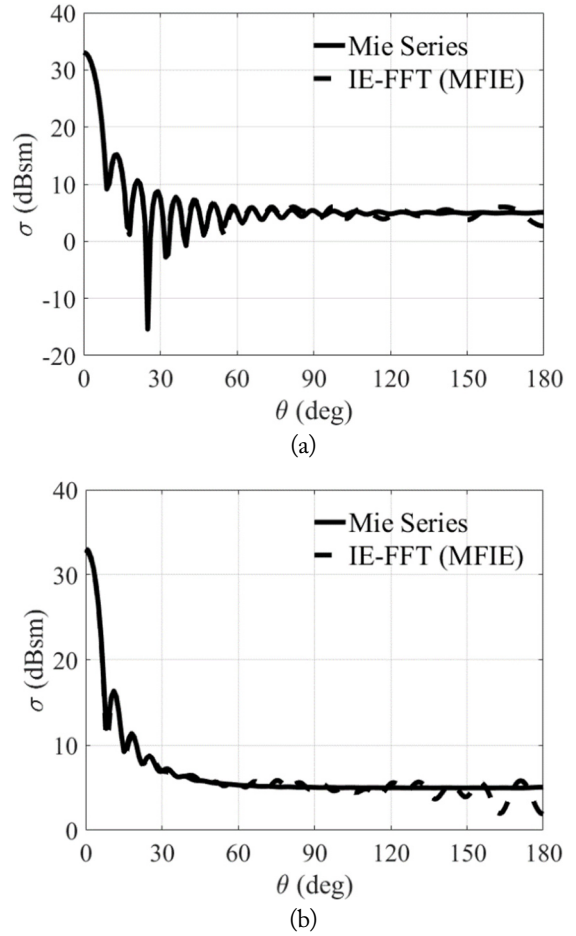


Fig. 5. The bistatic RCS for a one-meter PEC sphere at a frequency of 1,200 MHz. (a) E-plane and (b) H-plane.

Table 2. The CPU time and the number of iterations of the IE-FFT algorithm for scattering from a PEC sphere with a radius of 1 m

Freq. (MHz)	N	\mathbf{Z}^{corr}	$\bar{\mathbf{\Pi}}_A + \bar{\mathbf{\Pi}}_P$	MXV/iteration	No. of iteration
300	3,072	130	4	0.26	19
600	12,288	540	17	2.10	79
1,200	49,152	2,105	19	16.78	96

The memory requirement versus the number of unknowns is given in Fig. 6(a) for third-order Lagrange polynomials. The memory requirements of the correction, $\mathbf{\Pi}$ matrices, and the coefficients of the free-space Green's function are plotted with circles, squares, and diamonds, respectively. The $O(N)$ and $O(N^{1.5})$ complexities are plotted as dashed and dotted lines for references, respectively. The CPU time for the matrix-fill-in and the matrix vector multiplication per iteration versus the number of unknowns are plotted in Fig. 6(b). As an iterative solver, a generalized minimal residual method (GMRES) [11] is used when the matrix vector products are performed. There is

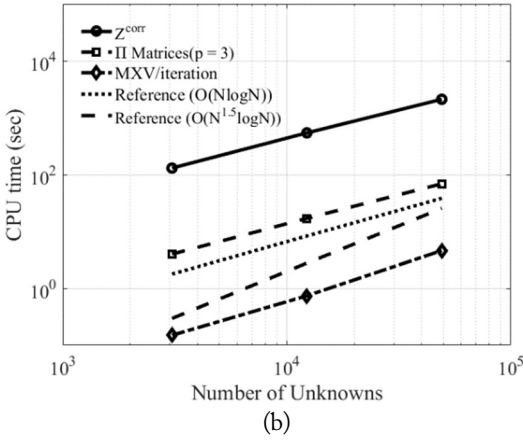
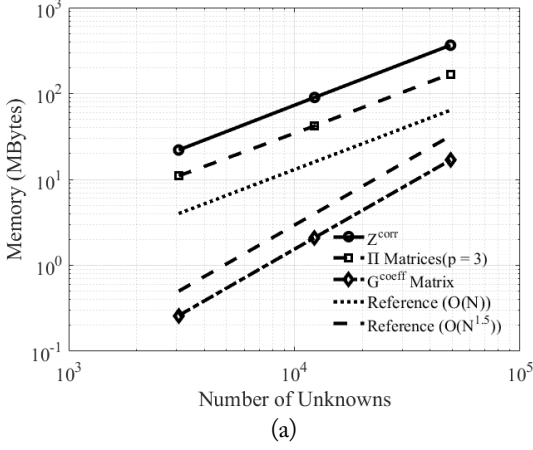


Fig. 6. The numerical complexities versus the number of unknowns ($p = 3$) (a) Memory requirements. (b) The CPU time for the matrix-fill-in and matrix-vector products per iteration.

no preconditioner. The tolerance of GMRES is 10^{-3} . The dashed and dotted lines of the $O(N)$ and $O(N^{1.5}\log N)$ complexities are plotted as references, respectively. The CPU time for assembling the correction $\mathbf{\Pi}$ matrices is $O(N)$ complexity. The CPU time of MXV is approximately $O(N^{1.5}\log N)$.

The accuracy of the IE-FFT algorithm for the MFIE formulation is addressed. The root mean square (RMS) error of the bistatic RCS is defined as

$$\eta(A) = \sqrt{\frac{\int_0^{2\pi} \int_0^\pi |RCS_A(\theta, \phi) - RCS_{Mie}(\theta, \phi)|^2 \sin \theta d\theta d\phi}{\int_0^{2\pi} \int_0^\pi |RCS_{Mie}(\theta, \phi)|^2 \sin \theta d\theta d\phi}}. \quad (21)$$

where θ and ϕ are the azimuth and elevation angles, $RCS_A(\theta, \phi)$ is the RCS value of the conventional MoM, the IE-FFT algorithm [9], and other numerical methods. First, we calculate the RMS error of the conventional MoM, relative to the Mie series solution versus the sampling segments per wavelength. The value of the error is the maximum error bound of the IE-FFT. For example, the RMS error of the bistatic RCS for a one-meter PEC sphere at a frequency of 600 MHz is

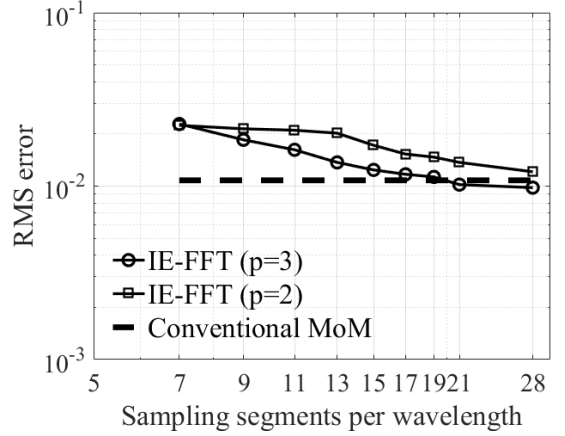


Fig. 7. The RMS errors of the bistatic RCS calculations versus the sampling segments per wavelength ($p = 2, 3$).

0.0108. Due to the hyper-singular integral of the MFIE formulation, the RMS error is much larger than that of the EFIE. The RMS errors of the IE-FFT, relative to the Mie series sampling segments per wavelength, are plotted in Fig. 7. The dashed line is the RMS error of the conventional MoM as a reference. The dash-dotted line with square markers and the solid line with circular markers represent the RMS error of the IE-FFT for the second- and third-order Lagrange polynomials, respectively. The RMS error of the second-order polynomials is converged with that of the conventional MoM with approximately 28 sampling segments. However, the RMS error of the third-order polynomials is converged with 19 elements. In this case, the RMS error for the MFIE is approximately 0.01. Some discrepancies are not the problem of the IE-FFT but that of the conventional MoM. The accuracy of the IE-FFT algorithm can be compared to that of the conventional MoM.

V. CONCLUSION

The IE-FFT algorithm with MFIE formulation achieves $O(N^{1.5})$ and $O(N^{1.5}\log N)$ complexities for required memory and CPU time, respectively. Also, it is shown that the proposed algorithm is highly efficient without the help of a preconditioner. The IE-FFT algorithm with MFIE formulation provides a high convergence rate as well. For better accuracy, a new scheme of hyper-singular integration should be further considered.

REFERENCES

- [1] R. F. Harrington, *Field Computation by Moment Methods*. New York, NY: The Macmillan Company, 1968.
- [2] R. E. Hodges and Y. Rahmat-Samii, "The evaluation of MFIE integrals with the use of vector triangle basis functions," *Microwave and Optical Technology Letters*, vol. 14, no.

- 1, pp. 9–14, 1997.
- [3] O. Ergul and L. Gurel, "Improved testing of the magnetic-field integral equation," *IEEE Microwave and Wireless Components Letters*, vol. 15, no. 10, pp. 615–617, 2005.
- [4] J. M. Song and W. C. Chew, "Multilevel fast-multipole algorithm for solving combined field integral equations of electromagnetic scattering," *Microwave and Optical Technology Letters*, vol. 10, no. 1, pp. 14–19, 1995.
- [5] S. M. Seo and J. F. Lee, "A single-level low rank IE-QR algorithm for PEC scattering problems using EFIE formulation," *IEEE Transactions on Antennas and Propagation*, vol. 52, no. 8, pp. 2141–2146, 2004.
- [6] K. Zhao, M. N. Vouvakis, and J. F. Lee, "Application of the multilevel adaptive cross-approximation on ground plane designs," in *Proceedings of 2004 International Symposium on Electromagnetic Compatibility (EMC)*, Silicon Valley, CA, 2004, pp. 124–127.
- [7] J. R. Phillips and J. K. White, "A precorrected-FFT method for electrostatic analysis of complicated 3-D structures," *IEEE Transactions on Computer-Aided Design of Integrated Circuits and Systems*, vol. 16, no. 10, pp. 1059–1072, 1997.
- [8] E. Bleszynski, M. Bleszynski, and T. Jaroszewicz, "AIM: adaptive integral method for solving large-scale electromagnetic scattering and radiation problems," *Radio Science*, vol. 31, no. 5, pp. 1225–1251, 1996.
- [9] S. M. Seo, C. Wang, and J. F. Lee, "Analyzing PEC scattering structure using an IE-FFT algorithm," *ACES Journal (The Applied Computational Electromagnetic Society Journal)*, vol. 24, no. 2, pp. 116–128, 2009.
- [10] S. Rao, D. Wilton, and A. Glisson, "Electromagnetic scattering by surfaces of arbitrary shape," *IEEE Transactions on Antennas and Propagation*, vol. 30, no. 3, pp. 409–418, 1982.
- [11] G. H. Golub and C. F. Van Loan, *Matrix Computations*. Baltimore, MD: The Johns Hopkins University Press, 1996.

Seung Mo Seo



received the B.S. degree from Hongik University in 1998 and the M.S. and Ph.D. degrees from the Ohio State University in 2001 and 2006, respectively, all in electrical engineering. From 1999 to 2006, he was a Graduate Research Associate with the ElectroScience Laboratory (ESL) in the Department of Electrical and Computer Engineering, the Ohio State University, Columbus, where he focused on the development of fast integral equation methods. From 2007 to 2010, he was Senior Engineer at the Digital Media and Communication (DMC) R&D Center of Samsung Electronics, where he developed RF circuit and antenna designs and simulations. From 2011 to the present, he has worked as a Senior Researcher at the Agency for Defense Development. His current research interest is computational electromagnetics.

Estimation of Detection Performance for Vehicle FMCW Radars Using EM Simulations

Sungjun Yoo¹ · Hanjoong Kim² · Gangil Byun³ · Hosung Choo^{1,*}

Abstract

This paper proposes a systematic method for estimating detection performances of a frequency-modulated continuous wave radar using electromagnetic simulations. The proposed systematic method includes a radar system simulator that can obtain range-Doppler images using the electromagnetic (EM) simulations in conjunction with a test setup employed for performance evaluation of multiple targets at different velocities in a traffic environment. This method is then applied for optimizing the half-power beamwidths of the antenna array using an evaluation metric defined to improve the detection strengths for the multiple targets. The optimized antenna has vertical and horizontal half-power beam widths of 10° and 60°, respectively. The results confirm that the proposed systematic method is suitable to improve the radar detection performance with the enhanced radar-Doppler images.

Key Words: FMCW Radar, Radar Performance Estimation, Vehicle Antenna.

I. INTRODUCTION

Recent radars are frequently used in vehicles with other sensors to assist the driver in obtaining information about the driving environment, which includes pedestrians, traffic lanes, other vehicles, and traffic sign recognition [1, 2]. In particular, frequency-modulated continuous wave (FMCW) radar systems have often been used as main sensors in various automotive radar applications because of their low cost, simple implementation, and high reliability in harsh weather conditions [3]. The FMCW radar system usually consists of a radio frequency (RF) device, a signal-processing module, and an antenna array. Since the signal-to-noise ratio (SNR) significantly affects the detecting performance of the radar system, the properties of the antenna array for the radar system, such as the gain, radiation pat-

tern, and half-power beamwidth (HPBW), should be carefully determined to maximize the strength of the signal transmitted and received through the antenna array. Thus, a systematic method for optimizing antenna characteristics of the FMCW radar is necessary to obtain the proper antenna performance in real traffic environments. However, most previous studies have focused on improving signal processing techniques and enhancing antenna gains, and in-depth studies of the radar estimation method for vehicle radars in a traffic environment have not been fully conducted yet [4, 5].

In this paper, we propose a novel systematic estimation method for the FMCW radar using electromagnetic (EM) simulations. The proposed systematic method is used to estimate detection performance based on the EM simulation in conjunction with a test setup employed for the evaluation of

Manuscript received March 13, 2018 ; Revised September 3, 2018 ; Accepted October 7, 2018. (ID No. 20180313-029J)

¹School of Electronic and Electrical Engineering, Hongik University, Seoul, Korea.

²Korea Aerospace Industries Ltd., Sacheon, Korea.

³School of Electrical & Computer Engineering, Ulsan National Institute of Science and Technology (UNIST), Ulsan, Korea.

*Corresponding Author: Hosung Choo (e-mail: hschoo@hongik.ac.kr)

This is an Open-Access article distributed under the terms of the Creative Commons Attribution Non-Commercial License (<http://creativecommons.org/licenses/by-nc/4.0>) which permits unrestricted non-commercial use, distribution, and reproduction in any medium, provided the original work is properly cited.

© Copyright The Korean Institute of Electromagnetic Engineering and Science. All Rights Reserved.

multiple targets with different velocities. In the test setup, the targets represent the surrounding objects in the real driving environment and are placed by considering the maximum detection range required for the FMCW radar. This radar system simulator is adopted to obtain range-Doppler images, which requires signal processing algorithms using data obtained from the EM simulations. In our EM simulation, the detailed antenna geometry and the targets are modeled as piece-wise mesh triangles, and the backscattered signals received by the antenna are accumulated for different frequencies. The range-Doppler images are completed by taking the two-step Fourier transform with the windowing, clipping, and filtering processes to improve the quality of the images. This systematic procedure is then applied to optimize the HPBW of the antenna array with an evaluation metric using an average and standard deviation of the detection strengths for the multiple targets. We also observe the variation of the images according to steering angles of the antenna array, and the results demonstrate that the proposed systematic method is suitable for use in estimating and optimizing the performance of FMCW radars in automotive applications.

II. PROPOSED SYSTEMATIC OPTIMIZATION PROCESS

Fig. 1 shows a flow chart of the proposed estimation method for evaluating the detection performance of an FMCW radar using the FEKO EM simulation software (Altair Engineering Inc., Troy, MI, USA). The procedure begins with modeling

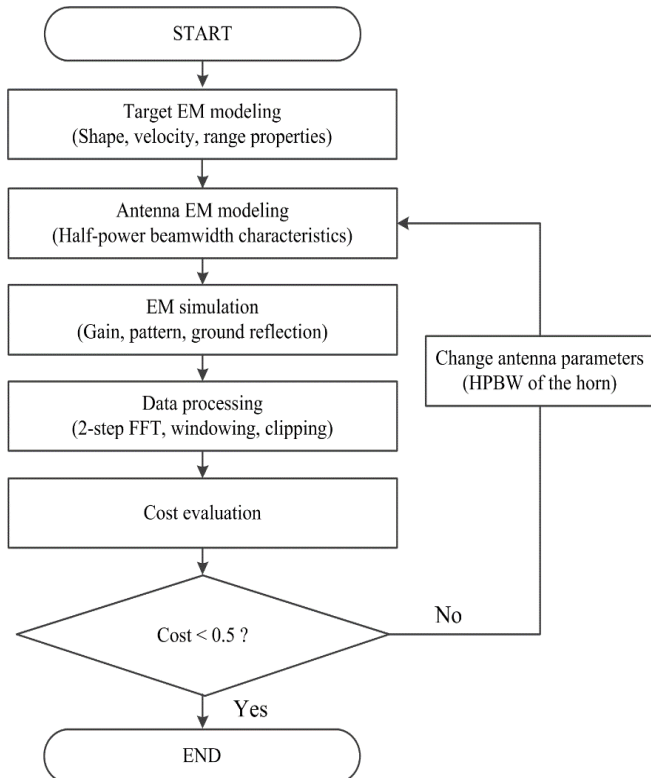


Fig. 1. Flow chart of the radar system simulator.

processes of radar targets and antennas to use in the radar system simulation, and their detailed design parameters are properly determined to improve the detection performance of the radar system. For example, if a horn antenna is used for the FMCW radar system, the width and the length of its aperture should be considered as the most important parameters for antenna characteristics, such as the gain, radiation pattern, and HPBW. In the EM simulation step, a test setup that includes targets, ground, and antenna is imported to obtain the transmitted and receive signal. The received signals for each chirp are used to calculate a range-Doppler map in the data processing step. This process is repeated to improving the detection performance of the antenna which has the optimal HPBW.

Fig. 2 presents the geometry of a horn antenna used in our approach. The antenna has a pyramidal shape, and the width and the height of the aperture are determined by a_x and a_y . The antenna is fed by a rectangular waveguide having a width of 3 mm and a height of 2 mm with a WR2810ADP adapter (Patentix Ltd., Ashkelon, Israel), and the total length of the antenna is about 74 mm [6]. The values of a_x and a_y are important to adjust the vertical and horizontal HPBWs as well as the bore-sight gain.

For example, if a_x varies from 19.2 mm to 4.1 mm, the vertical HPBW increases from 10° to 50° , and the horizontal HPBW becomes broader from 20° to 60° , when a_y is changed from 30 mm to 3.8 mm. The antenna and target models are then imported as piecewise mesh triangles, and the ground plane is assumed to be an infinite substrate with dielectric properties of $\epsilon_r = 4.5$ and $\tan\delta = 0.97$. In the EM simulation process, the transmit antenna pattern is imported as a far-field source to

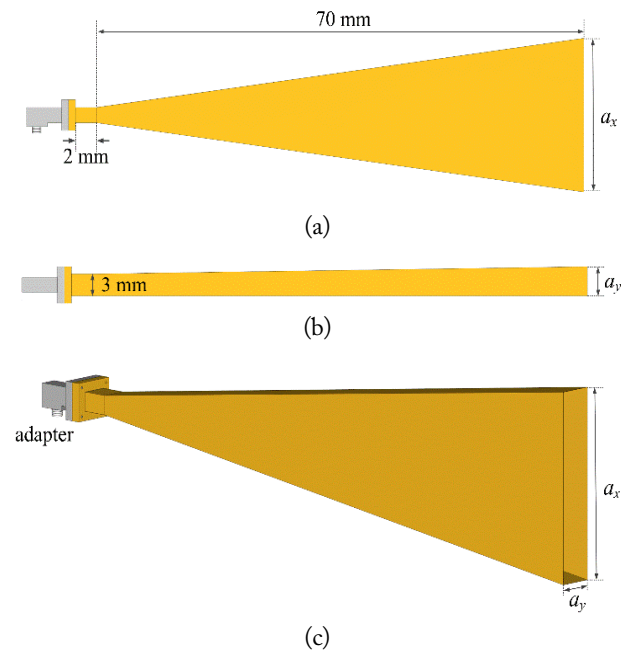


Fig. 2. Geometry of the basic pyramidal horn antenna. (a) Side view, (b) top view, and (c) perspective view.

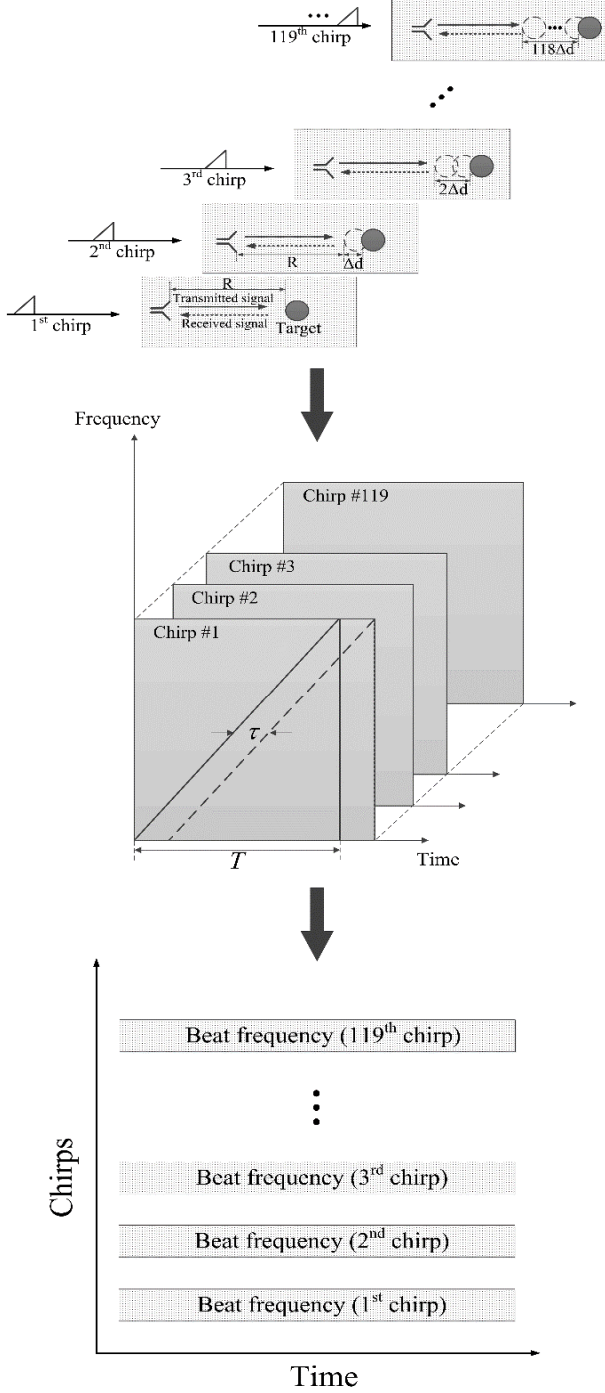


Fig. 3. EM simulation process for moving targets in FMCW radar system.

obtain the amplitude and phase information of the backscattered electromagnetic waves for every chirp duration [7], as illustrated in Fig. 3. The received signal contains the information of electromagnetic properties, such as gain of the transmitting antenna, reflectivity of targets, space losses due to target positions (R), and ground reflections. Then, the received signals are used to calculate the beat frequencies for the chirps, and these calculated data are stacked in sequence as a 2D matrix. Finally, the range-Doppler map is obtained using the matrix through the two-step fast Fourier transform (FFT), and the quality of

the image can be further improved by applying the windowing, clipping, and filtering techniques [7]. It is assumed that the FMCW radar operates at a frequency of 77.5 GHz with a bandwidth of 200 MHz. The chirp duration of the transmitted signal is 33 μ s, and 119 chirps are transmitted to plot range-Doppler images. At each chirp, the simulation based on the physical optic analysis is conducted at 165 frequency points, which implies a frequency interval of 5 MHz. In this case, the size of the 2D matrix with the beat frequency data becomes 165 \times 119 for each range-Doppler image. Using the proposed systematic method, we optimize HPBW's of the antenna array using an evaluation metric that is defined to well visualize the multiple targets with a high average and a lower standard deviation of the target strengths as in (1).

$$Cost = c \cdot (\alpha \cdot \sigma - \beta \cdot \mu) + 1, \quad (1)$$

$$\sigma = \sqrt{\frac{\sum_{k=1}^{N_{target}} (A_k - \mu)^2}{N_{target}}}, \quad \mu = \frac{\sum_{k=1}^{N_{target}} A_k}{N_{target}}, \quad (2)$$

where σ is the standard deviation, and μ is the average value of the amplitude. k is an index of each target, and A_k shows the k -th amplitude of the A_k . We fixed α , β , and c as 0.02, 0.75, and 10 to obtain the positive value of the cost. The goal of 0.5 is empirically determined by the consideration of the detection performance to well visualize the multiple targets while the range and velocity property of all targets are clearly detected in the proposed system. When the cost value does not meet our goal of 0.5, we iterate this process by changing the values of the design parameters.

Fig. 4 shows the proposed test setup, which is composed of

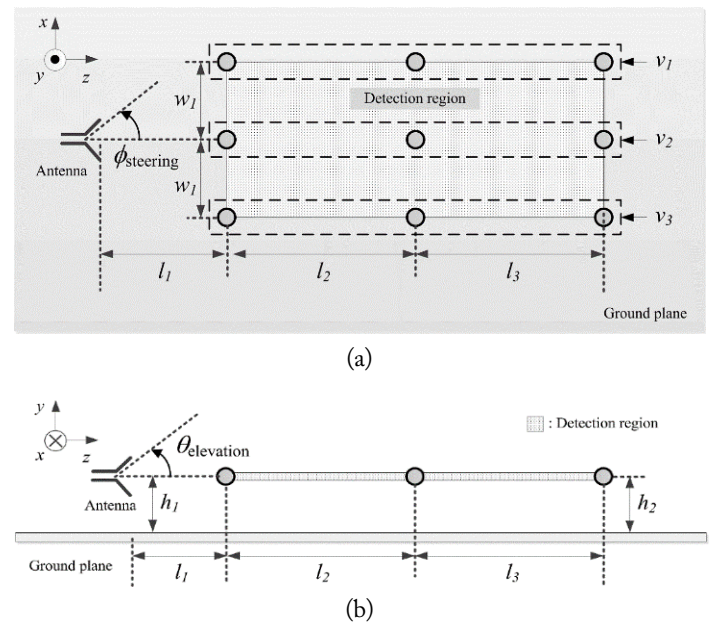


Fig. 4. Geometry of the proposed test setup. (a) Top view and (b) side view.

Table 1. Parameters for the test setup in the detection region

Parameter	Value
v_1	10 m/s
v_2	0 m/s
v_3	-10 m/s
l_1	5 m
l_2	20 m
l_3	25 m
w_1	10 m
h_1	1 m
h_2	1 m
$\theta_{elevation}$	0°
$\phi_{steering}$	0°

one antenna and nine multiple targets. Each target has a spherical shape with a diameter of 50 mm, and the 3×3 targets are located in the detection region, which has a horizontal and vertical spacing of $w_1=10$ m, $l_2=20$ m, and $l_3=25$ m. The distance between the transmitting antenna and the first column targets is l_1 , and a steering angle is $\phi_{steering}$. The velocities of targets in the three rows, denoted as v_1 , v_2 , and v_3 , are set differently to distinctly visualize all the targets on the range-Doppler image. The amplitudes at the target positions on the image represent the detection performance of a radar system. Note that this scenario is based on real driving environments as listed in Table 1, and thus the ground material is assumed as concrete with a relative dielectric constant of 7 and a conductivity of 0.08 S/m [8].

III. RESULTS AND ANALYSIS

To obtain the optimum HPBW of the antenna with the improved detection performances of the radar system, the vertical and horizontal HPBWs of the antenna are varied from 10° to 50° and from 20° to 60° , respectively. Fig. 5 presents the cost values of the radar images calculated at an interval of 10° , and the maximum value of the costs is 0.82 when the vertical

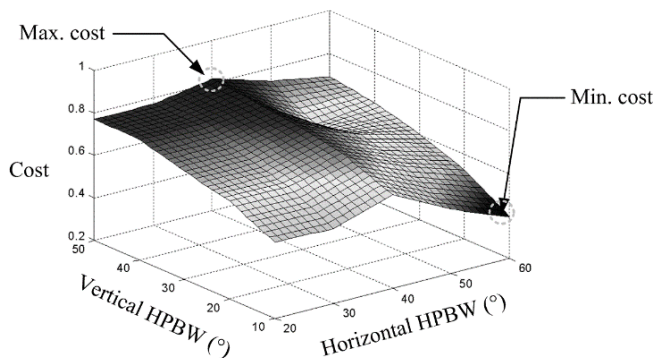


Fig. 5. 3D-plot of the costs with vertical and horizontal HPBWs.

and horizontal HPBWs of the antenna are 50° and 40° . The optimal vertical and horizontal HPBWs with minimum cost of 0.40 are 10° and 60° , respectively.

Fig. 6 shows the comparison between the proposed antenna with minimum cost and the antenna with maximum cost. The proposed antenna, which has optimal vertical and horizontal HPBWs to improve the detection performances, is specified as the solid line with circle, and the solid line with triangle indicates the antenna with maximum cost. The bore-sight gain and HPBW of the proposed antenna are 17 dBi and 60° at 77 GHz, which are 12.4 dBi and 40° higher than greater than those of the maximum cost antenna, respectively. The comparison of the 3D radiation patterns is illustrated in Fig. 7(a) and (b). As ex-

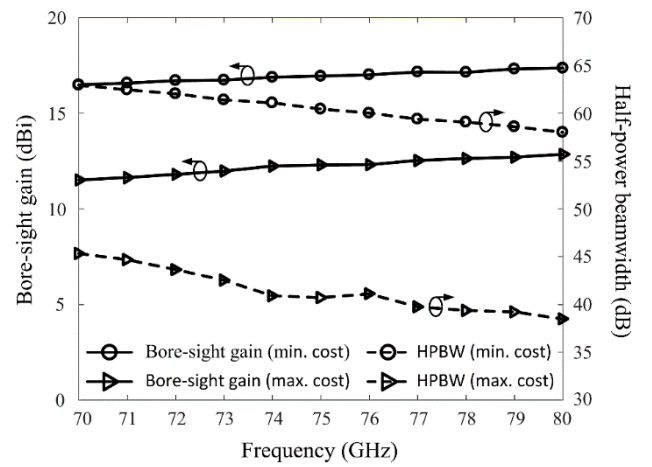
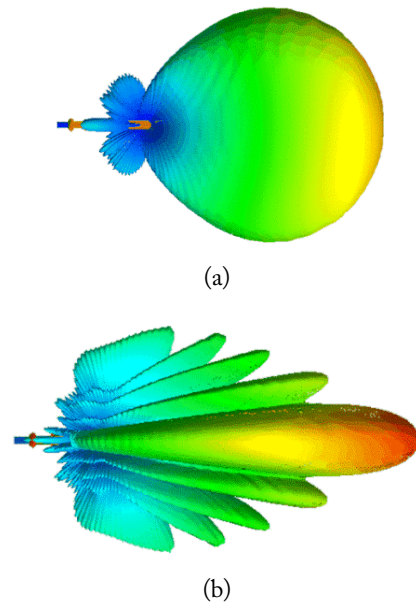


Fig. 6. Comparison of the antenna properties between minimum cost and maximum cost antennas.


 Fig. 7. Comparison of the 3D patterns of the antenna. (a) Vertical and horizontal HPBWs of 50° and 40° (max. cost antenna) and (b) vertical and horizontal HPBWs of 10° and 60° (min. cost antenna).

pected, the pattern of the proposed antenna has broader beamwidth and higher gain compared with the antenna with maximum cost in the horizontal direction (xz -plane).

Fig. 8(a) shows radiation patterns of the horn antenna with maximum cost, which has a bore-sight gain of 12.4 dBi and vertical and horizontal HPBW of 50° and 40° . The HPBW of the antenna with minimum cost are 10° and 60° , and the aperture size is $19.2 \text{ mm} \times 3.8 \text{ mm}$ with the bore-sight gain of 17 dBi as presented in Fig. 8(b).

Fig. 9(a) and (b) represent the comparison range-Doppler image according to different antenna characteristics. Fig. 9(a) shows the range-Doppler image with vertical and horizontal HPBW of 50° and 40° . The nine targets are detected separately according to their ranges and velocities, and the strengths of the targets with the velocity of 0 m/s are greater because they are placed in the main lobe direction of the transmitting antenna. On the other hand, other targets with non-zero velocities are detected with weaker strengths because the antenna gain of the side direction is lower than that of the bore-sight direction. Fig. 9(b) presents the range-Doppler image using an antenna with

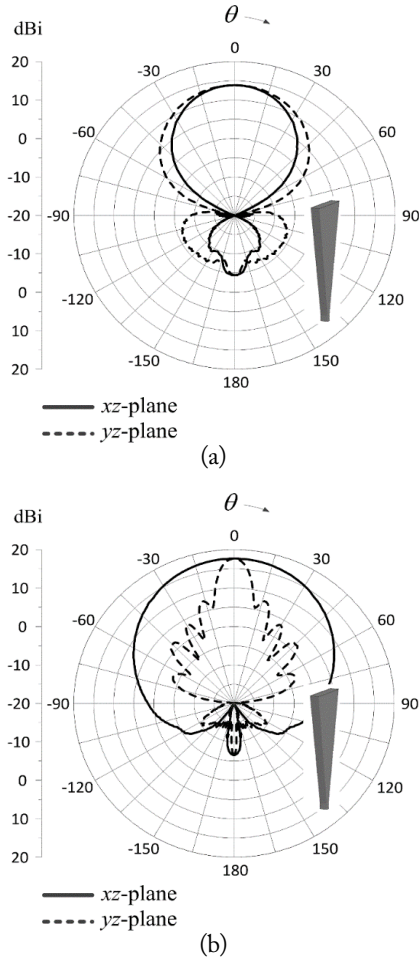


Fig. 8. Comparison of the 2D patterns. (a) Vertical and horizontal HPBW of 50° and 40° (max. cost antenna) and (b) vertical and horizontal HPBW of 10° and 60° (min. cost antenna).

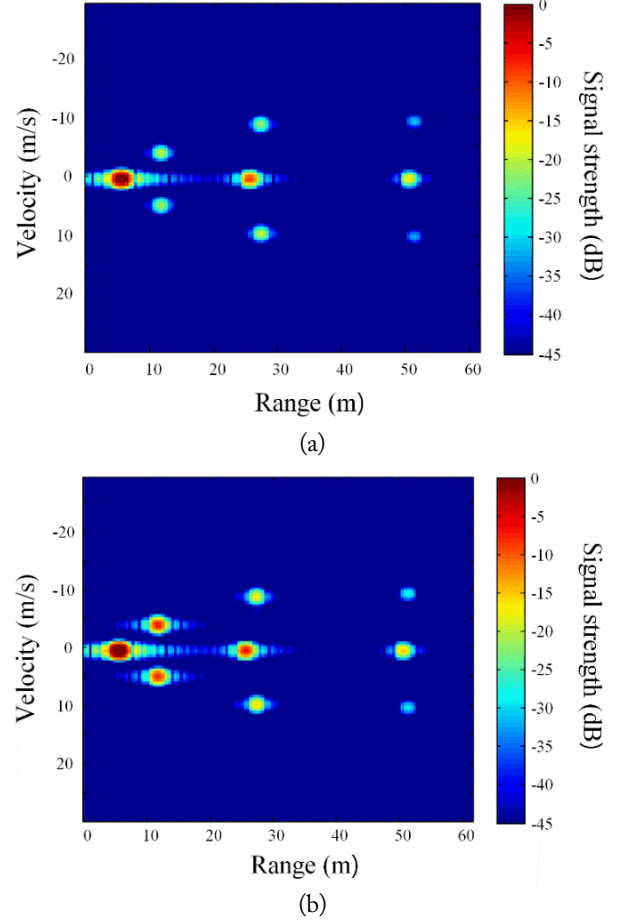


Fig. 9. Comparison range-Doppler images. (a) Range-Doppler image with vertical and horizontal HPBW of 50° and 40° and (b) range-Doppler image with vertical and horizontal HPBW of 10° and 60° .

the optimum HPBW. The minimum cost values result in the improvement of target strengths, especially for the boundary targets at the upper and lower rows, which is obvious when compared to the results provided in Fig. 9(a).

To verify the applicability of the proposed systematic estimation scheme to other scenarios, we change the parameters of the test setup, such as distance between targets (l_2 and l_3) as shown in Fig. 10. The distance of l_2 is varied from 20 to 5 with l_3 of 10 to place the targets close together, and the nine targets are detected with greater strength using the optimal HPBW antenna with lower cost value compared to the antenna with the maximum cost. To observe the feasibility of the beam steering of the proposed radar system, we adopted a four-element array as shown in Fig. 11. The phase information of the individual elements is implemented to steer the beam direction of the array antenna, and the main-beam direction is varied from 0° to 15° without significant pattern degradation. The results indicate that the arrays are suitable to use with FMCW radar antennas to improve detection performance.

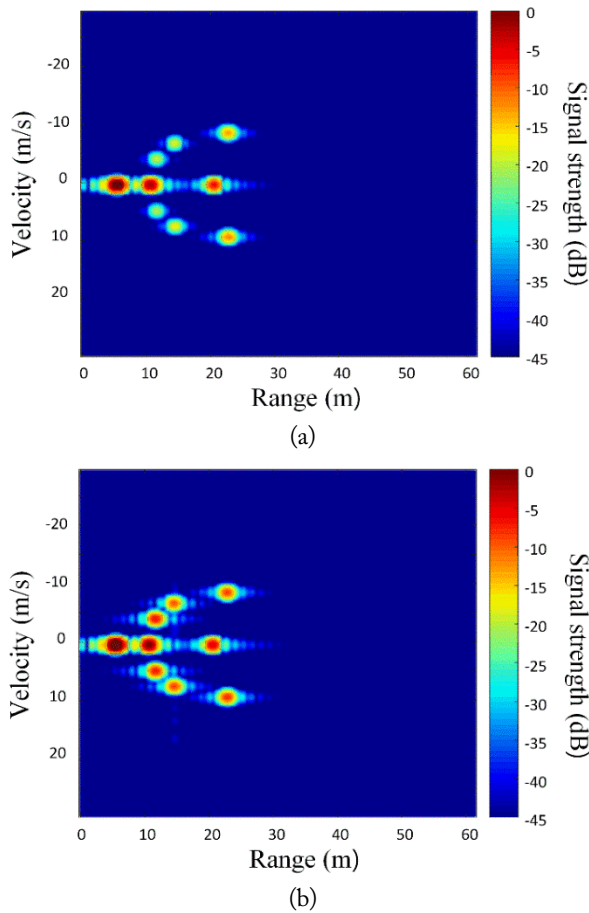


Fig. 10. Comparison range-Doppler image using another scenario. (a) Range-Doppler image with vertical and horizontal HPBWs of 50° and 40° and (b) range-Doppler image with vertical and horizontal HPBWs of 10° and 60°.

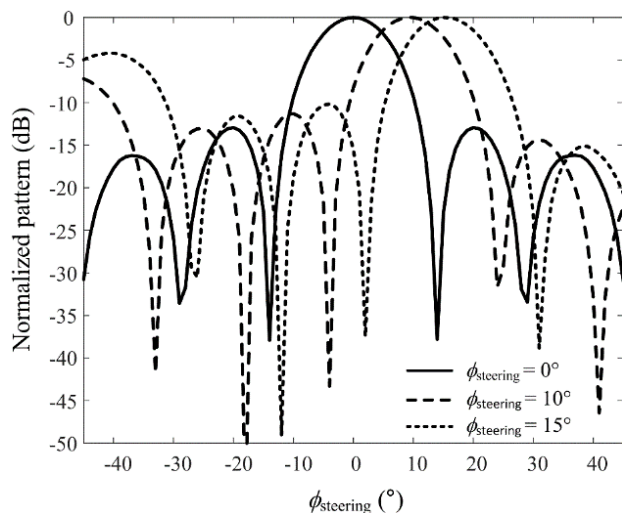


Fig. 11. Radiation patterns of the horn antenna array.

IV. CONCLUSION

We have investigated the systematic method for estimating detection performances of the FMCW radar using EM simula-

tions. The proposed method was adopted to obtain range-Doppler images using signal processing algorithms and was also used to optimize the HPBW of the antenna array with the evaluation metric. The optimized antenna has vertical and horizontal HPBWs of 10° and 60° with the evaluation metric value of 0.4. To verify the variation of the images according to the steering angle of the antenna array, the steered array beam pattern was adopted to the test setup for obtaining the range-Doppler image. The results confirmed that the proposed systematic estimation method is suitable for use in estimating and optimizing the performance of FMCW radars.

This work was supported by the research fund of Signal Intelligence Research Center supervised by Defense Acquisition Program Administration and Agency for Defense Development of Korea.

REFERENCES

- [1] T. N. Luo, C. H. Wu, and Y. J. E. Chen, "A 77-GHz CMOS automotive radar transceiver with anti-interference function," *IEEE Transactions on Circuits and Systems I: Regular Papers*, vol. 60, no. 12, pp. 3247–3255, 2013.
- [2] M. S. Lee and Y. H. Kim, "Design and performance of a 24-GHz switch-antenna array FMCW radar system for automotive applications," *IEEE Transactions on Vehicular Technology*, vol. 59, no. 5, pp. 2290–2297, 2010.
- [3] L. Giuhholini, "A multistatic microwave radar sensor for short range anticollision warning," *IEEE Transactions on Vehicular Technology*, vol. 49, no. 6, pp. 2270–2275, 2000.
- [4] I. E. Lager, C. Trampuz, M. Simeoni, and L. P. Ligthart, "Interleaved array antennas for FMCW radar applications," *IEEE Transactions on Antennas and Propagation*, vol. 57, no. 8, pp. 2486–2490, 2009.
- [5] A. Laloue, J. C. Nallatamby, M. Prigent, M. Camiade, and J. Obregon, "An efficient method for nonlinear distortion calculation of the AM and PM noise spectra of FMCW radar transmitters," *IEEE Transactions on Microwave Theory and Techniques*, vol. 51, no. 8, pp. 1966–1976, 2003.
- [6] "ALLDATASHEET: datasheet search site for electronic components," 2018; <http://www.alldatasheet.com>.
- [7] A. Naqvi and H. Ling, "A study of radar features of wind turbines in the HF band," *Progress in Electromagnetics Research*, vol. 143, pp. 605–621, 2013.
- [8] T. Bourdi, J. E. Rhazi, F. Boone, and G. Ballivy, "Modeling dielectric-constant values of concrete: an aid to shielding effectiveness prediction and ground-penetrating radar ave technique interpretation," *Journal of Physics D: Applied Physics*, vol. 45, no. 40, article no. 405401, 2012.

Sungjun Yoo



for adaptive beamforming.

received the B.S. and M.S. degrees in electronic and electrical engineering from Hongik University, Seoul, Korea, in 2014 and 2016, respectively. He is currently working toward the Ph.D. degree in electronics and computer engineering at Hongik University, Seoul, Korea. His research interests include the global positioning system antennas, antenna arrays, and position optimization of array elements

Gangil Byun



Computer Engineering (ECE). Dr. Byun's principal areas of research are in the design and analysis of small antenna arrays for adaptive beamforming applications, such as direction of arrival estimation, interference mitigation, and radar. His recent research interests also include circularly-polarized antennas, vehicular and aeronautic antennas, global positioning system antennas, and array configuration optimization.

received his B.S. and M.S. degrees in electronic and electrical engineering from Hongik University, Seoul, Korea in 2010 and 2012, respectively, and his Ph.D. degree in electronics and computer engineering from Hanyang University, Seoul, Korea in 2015. He joined the faculty of Ulsan National Institute of Science and Technology (UNIST) in February 2018 and is currently Assistant Professor of Electrical and

Hanjoong Kim



received his B.S. and M.S. degrees in electronic and electrical engineering from Hongik University, Seoul, Korea in 2013 and 2015, respectively. He joined the Korea Aerospace Industries (KAI), Sacheon, Korea in 2015 and is currently in charge of the design and test for the unmanned air vehicles (UAVs) system. His fields of research include the design and analysis of the antennas and radar systems for the vehicles.

Hosung Choo



principal areas of research are the use of the optimization algorithm in developing antennas and microwave absorbers. His studies include the design of small antennas for wireless communications, reader and tag antennas for RFID, and on-glass and conformal antennas for vehicles and aircraft.

received the B.S. degree in radio science and engineering from Hanyang University in Seoul in 1998, and the M.S. and Ph.D. degrees in electrical and computer engineering from the University of Texas at Austin, in 2000 and 2003, respectively. In September 2003, he joined the school of electronic and electrical engineering, Hongik University, Seoul, Korea, where he is currently a full professor. His

Wide and Dual-Band MIMO Antenna with Omnidirectional and Directional Radiation Patterns for Indoor Access Points

Insu Yeom¹ · Young Bae Jung² · Chang Won Jung^{1,*}

Abstract

A wide-band multiple-input multiple-output (MIMO) antenna with dual-band (2.4 and 5 GHz) operation is proposed for premium indoor access points (IAPs). Typically, an omni-directional pattern is used for dipole antennas and a directional radiation pattern is used for patch antennas. In this paper, both antenna types were used to compare their performance with that of the proposed 2×2 MIMO antenna. We simulated and measured the performance of the MIMO antenna, including the isolation, envelope correlation coefficient (ECC), mean effective gain (MEG) for the IAPs, and the throughput, in order to determine its communication quality. The performance of the antennas was analyzed according to the ECC and MEG. The proposed antenna has sufficient performance and excellent characteristics, making it suitable for IAPs. We analyzed the communication performance of wireless networks using the throughput data of a typical office environment. The network throughput of an 802.11n device was used for the comparison and was conducted according to the antenna type. The results showed that the values of the ECC, MEG, and the throughput have unique characteristics in terms of their directivity, antenna gains, isolation, etc. This paper also discusses the communication performance of various aspects of MIMO in multi-path situations.

Key Words: Access Point, Antenna Diversity, MIMO, Throughput Data, WLAN.

I. INTRODUCTION

The rapidly increasing demand for broadband traffic is driving the need for cellular networks with higher capacity. In these communication systems, high data transmission rates and low bit error probability are common requirements [1–3]. Multiple-input multiple-output (MIMO) systems have been broadly investigated because they can increase the channel capacity without sacrificing additional spectra [4]. Multiple antennas, which are used in wireless local area networks (WLANs), can increase

the channel capacity [5]. Several antennas have been designed with various patterns for indoor access points (IAPs). Omni-directional antennas (such as dipole antennas) and directional antennas (such as patch antennas) are generally useful for a variety of access points (APs), because the radiation patterns of these antennas allow for good transmission and reception from mobile units. Omni-directional antennas feature a radiation pattern that is nearly symmetric [6–8]. The directional pattern in patch antennas affects the radio frequency (RF) coverage by focusing the bulk of the RF energy in a specific direction [9, 10].

Manuscript received April 30, 2018 ; Revised July 11, 2018 ; Accepted October 17, 2018. (ID No. 20180430-038J)

¹Graduate School of Nano · IT · Design Fusion, Seoul National University of Science and Technology, Seoul, Korea.

²Department of Electronics and Control Engineering, Hanbat National University, Daejeon, Korea.

*Corresponding Author: Chang Won Jung (e-mail: changwoj@seoultech.ac.kr)

This is an Open-Access article distributed under the terms of the Creative Commons Attribution Non-Commercial License (<http://creativecommons.org/licenses/by-nc/4.0>) which permits unrestricted non-commercial use, distribution, and reproduction in any medium, provided the original work is properly cited.

© Copyright The Korean Institute of Electromagnetic Engineering and Science. All Rights Reserved.

Dual bands with a broad bandwidth are advantageous for wireless networks in order to allow a greater number of devices to share the available space. However, dipole and patch antennas typically have a narrow bandwidth, and it is particularly difficult to implement a dual-band (2.4 and 5 GHz) patch antenna with a wide band. Several researchers have studied the communication performance of WLANs using the 802.11 MAC protocol. The throughput performance of the 802.11 WLAN has been simulated using many interesting methods. Modelling the throughput performance in a WLAN involves studying parameters such as the packet length and the transmission rate [11, 12]. However, researchers have validated only a predictive model and simulated data transmission with different packet lengths and hotspots [13]. Other researchers have evaluated performance according to different clients with representative 802.11 chipsets [14]. In addition, throughput data has been simulated in terms of beam patterns in a scattering environment [15]. However, no studies have measured throughput data in real multipath conditions or analyzed MIMO performance.

In this paper, two typical antennas that represent omnidirectional and directional radiation patterns were designed to compare the performance of these antennas with that of MIMO in an IAP. The antennas were composed of dual bands (2.4 and 5 GHz) and designed according to their radiation pattern. The frequency covers the entire WLAN band (IEEE 802.11b/g and 802.11a/j) and the antennas have sufficient gain and beam coverage to be applied to a premium access point, which requires the antenna to operate in the full frequency band for WLAN service. First, the dipole antenna with omni-directional pattern was designed. Then, the dipole antenna was designed using back-to-back radiators. The dipole antenna was arrayed to enhance the gain and was optimized with a transformer. The proposed omni-directional antenna operates over a broadband and covers nearly 360 degrees. Further, a dual-band, slot-coupled, patch antenna with a directional pattern was designed. Radiation was used to focus the radio signal in order to direct the energy in specific directions. Patch antennas are generally recommended to be placed down hospital hallways or office corridors. To improve the directivity of the proposed antenna, we used parasitic elements and a reflector. The proposed antenna enhanced the bandwidth by more than 18% at the 5 GHz band [16]. High isolation and a low envelope correlation coefficient (ECC) are required in MIMO systems [17–20]. We analyzed the isolation and the ECC. The mean effective gain (MEG) of the antenna elements has been widely used to describe the diversity performance of multiple-antenna systems in random multipath, which exist in reflection, diffraction, and scattering. The proposed MIMO antenna has high isolation, a low ECC, and a high enough MEG. Next, we evaluated the throughput performance of WLANs according to the gain, directivity, and

isolation in a real office environment.

II. PROPOSED ANTENNA STRUCTURE

1. Dipole Antenna with an Omni-directional Radiation Pattern

Fig. 1 shows a perspective drawing of the dipole antenna. Each dipole is optimized for 2.4 GHz and 5 GHz and includes the upper and lower portions of the antenna, such that the antenna is operable as a standard half-wavelength dipole antenna. In order to maximize the gain of the proposed antenna, the radiating dipole elements were separated by a distance of $0.6\lambda_g$, as shown in Fig. 1(a). The proposed structure is symmetrical on the right and left. Fig. 1(b) also illustrates the geometry and configuration of the proposed dual-band dipole antenna, which is printed on a 0.8-mm thick RF30 (Taconic Inc.). The top plane consists of high-band (5 GHz) and low-band (2.4 GHz) radiating elements; the line of the high-band element is 11 mm, and the line of the low-band element is 23 mm. The distance between the high-band elements is 8 mm and the distance between the low-band elements is 11 mm. A quarter-wave transformer was implemented to match the $70.7\ \Omega$ and $100\ \Omega$ lines with the $50\ \Omega$ microstrip line. The width of the quarter-wave transformer was optimized for each characteristic impedance. The $100\text{-}\Omega$ line is 20.7 mm, the $70.7\text{-}\Omega$ line is 4 mm, and the $50\text{-}\Omega$ line is 12.3 mm. The impedance of the $100\text{-}\Omega$ line was

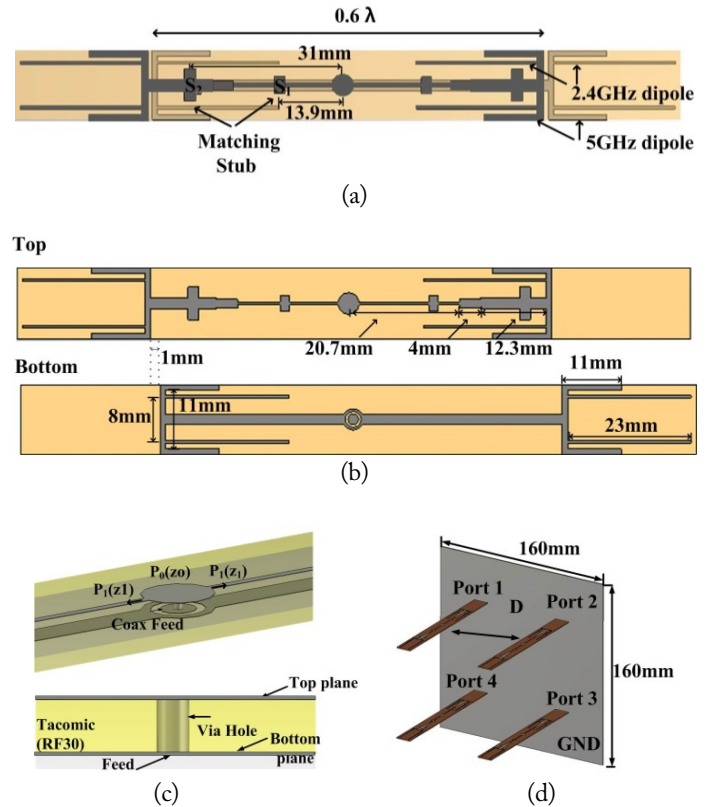


Fig. 1. Dipole antenna: (a) dipole antenna, (b) top and bottom, (c) side, and (d) MIMO antenna.

divided into the 50-Ω line. The ground width of the bottom plane is 2 mm. To improve the impedance of the proposed antenna, we used the stub elements, S_1 and S_2 , at the bottom plane. Both S_1 and S_2 are configured with $\lambda_g/4$ open stub. S_1 is 3 mm × 1.8 mm, and it was placed 13.9 mm away from the feed. S_2 is 6 mm × 2 mm, and was placed 31 mm from the feed. The detailed feeding structure is shown in Fig. 1(c); the feed of the bottom plane is connected to that of the top plane. The antenna array is composed of two dipole antenna elements. The two microstrip lines used for the array configuration were printed on the top layer. As shown in Fig. 1(c), if the input port impedance of P_0 is Z_0 (50 Ω), and the two output ports have the same impedance of $Z_1 = 2 \times Z_0$ (100 Ω), then the input power can be equally divided into the output ports. The MIMO antenna is composed of four dipole antennas with a 2 × 2 structure. The overall size of the MIMO antenna is 160 mm × 160 mm, as shown in Fig 1(d).

The distance between the two radiators is $0.67\lambda_g$ (80 mm) at the 2.4 GHz band and $1.3\lambda_g$ (80 mm) at the 5.4 GHz band. The fabricated dipole antenna is shown in Fig. 2. The electric energy density of the antenna is shown in Fig. 3. The electric energy shows that each high and low-band radiating element plays a role in determining the operating frequency.

2. Patch Antenna with a Directional Radiation Pattern

The configuration of the proposed patch antenna is shown in Fig. 4 and that of the slot antenna is shown in Fig. 4(a) [21]. The size of the reflector is 80 mm × 80 mm. The substrate that the first radiator was printed on was an RF 30 by Taconic Inc. with a 0.8 mm thickness and relative permittivity (ϵ_r) of 2.9. The size of the substrate is 56 mm × 56 mm. It is configured as a bow-tie shape to enhance the bandwidth at the 2 GHz band.

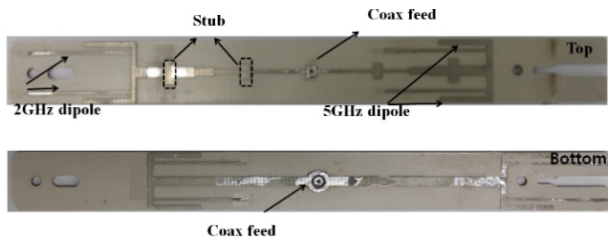


Fig. 2. Dipole antenna fabricated for an indoor access point.

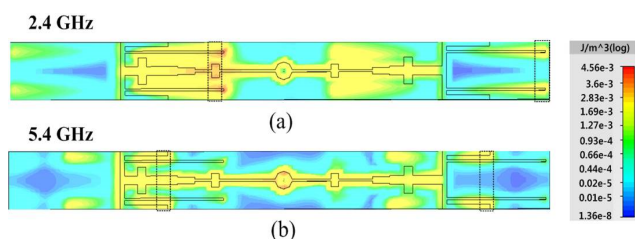


Fig. 3. Electric energy density (J/m^3) of the dipole antenna at the 2.4 GHz (a) and 5.4 GHz (b) bands.

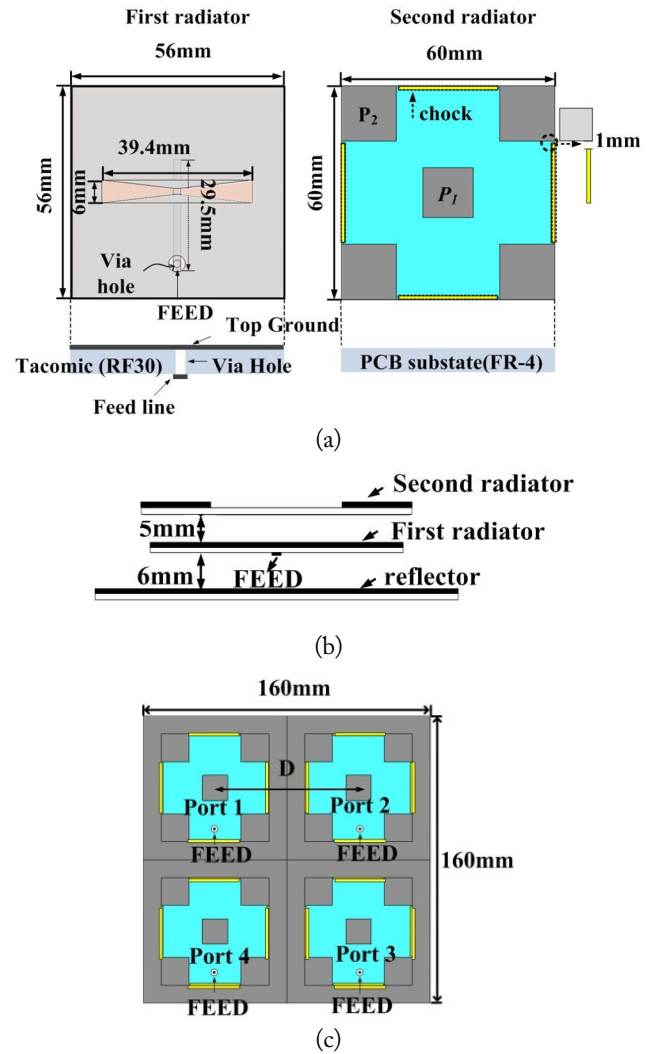


Fig. 4. Patch antenna: (a) top, (b) side, and (c) MIMO antenna.

The dimension of the slot with the bow-tie shape is 39.4 mm × 6 mm so it can operate at 2.4 GHz. The length of the feed line on the slot antenna is 29.5 mm and the width of the feed line is 2 mm, for a characteristic impedance of 50 Ω. The radiator size of the patch antenna of the second radiator operating at the 5 GHz band is 60 mm × 60 mm, and the rectangular patch (P_1) on the center of the second radiator is 14 mm × 14 mm. This antenna was printed on a 1 mm thick substrate (FR-4: $\epsilon_r = 4.4$, $\tan \delta = 0.02$) [22]. All metal was etched with copper, and the depth of etching copper is 17.5 μm (0.5 oz). The patch is usually $0.3333\lambda < \text{Length} < 0.5\lambda$, where λ is the free-space wavelength. The patch is designed to be very thin such that $t \ll \lambda$ (where t is the patch thickness). The height h of the dielectric is usually $0.003\lambda \leq h \leq 0.05\lambda$ [23]. The optimized dimensions of the four parasitic patches (P_2) are 15.5 mm × 15.5 mm and they are separated from the rectangular patch (P_1) by $0.5\lambda_g$ at the 5 GHz band (7.5 mm). The chocks (28 mm × 1 mm) were etched on the patch antenna with a gap of 1 mm from the parasitic patch (P_2). The azimuth beam width is wider than the

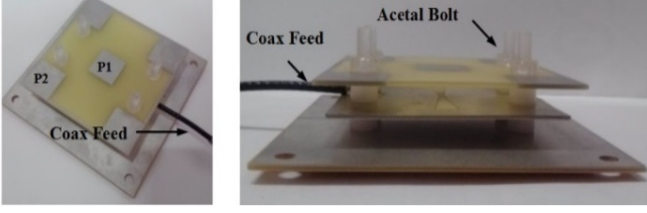


Fig. 5. Patch antenna fabricated for an indoor access point.

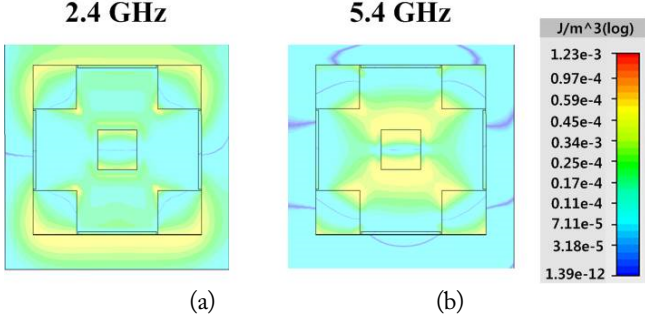


Fig. 6. Electric energy density (J/m^3) of the patch antenna at the 2.4 GHz (a) and 5.4 GHz (b) bands.

elevation beam width. The chock of the second radiator decreases the beam width of the azimuth. Controlling the beam width can improve isolation among the radiators in MIMO structures. A side view of the proposed antenna is shown in Fig. 4(b). The distance between the slot antenna and the reflector is 6 mm, and the distance between the first and second radiator is 5 mm ($1/8\lambda_g$ at the 5 GHz band). The MIMO antenna is composed of four patch elements, as shown in Fig 4(c). The MIMO antenna overall is $160 \text{ mm} \times 160 \text{ mm}$. The distance among the patch radiators is $0.67\lambda_g$ (80 mm) at the 2.4 GHz band and $1.3\lambda_g$ (80 mm) at the 5.4 GHz band. The fabricated patch antenna is shown in Fig. 5, and the electric energy density is shown in Fig. 6. As pictured, the electric energy density of the rectangular patch (P_1) is transferred to the parasitic patch (P_2) by coupling. The simulation showed that parasitic patches play a role in determining the bandwidth at the 5 GHz band.

III. MIMO PERFORMANCE OF THE PROPOSED ANTENNA

The MEG was defined in [24] as the ratio between the mean received power of the antenna and the total mean incident power. It can be calculated by (1):

$$MEG = \frac{P_{rec}}{(P_V + P_H)} \quad (1)$$

The expression for the MEG can be rearranged as the following equation:

$$MEG = \int_0^{2\pi} \int_0^\pi \left(\frac{XPR}{1+XPR} G_\theta(\theta, \phi) P(\theta, \phi) + \frac{XPR}{1+XPR} \right) \quad (2)$$

$$G_\phi(\theta, \phi) P_\phi(\theta, \phi) \sin \theta d\theta d\phi$$

where $G_\theta(\theta, \phi)$ and $G_\phi(\theta, \phi)$ are the θ and ϕ components of the antenna power gain pattern, respectively, and $P_\theta(\theta, \phi)$ and $P_\phi(\theta, \phi)$ are the θ and ϕ components of the angular density functions of the incoming plane waves, respectively.

We analyzed MEG according to the propagation models. The wireless channel is modelled to specify the incident field in the form of an angular density function. In this paper, we used the typical model of an incident field using both the uniform spread in the azimuth angle and Gaussian spread in elevation angle according to the general method of MIMO measurement. The statistical distribution of Gaussian in the elevation angle (θ) is determined by the following equation:

$$P_\theta(\theta) = e^{-\left[\frac{\left(\theta - \left(\frac{\pi}{2} - m_v \right) \right)^2}{2\sigma_v^2} \right]}, \quad P_\phi(\phi) = e^{-\left[\frac{\left(\phi - \left(\frac{\pi}{2} - m_h \right) \right)^2}{2\sigma_h^2} \right]} \quad (3)$$

Also, the statistical distribution of uniform in azimuth angle (ϕ) is determined by the following equation:

$$P_\theta(\phi) = 1, \quad P_\phi(\phi) = 1 \quad (4)$$

where m_v and m_h are, respectively, the mean elevation angle of each vertically polarized and horizontally polarized wave distribution observed from the horizontal direction. In addition, σ refers to the standard deviation of the vertical (σ_v) and horizontal (σ_h) wave distributions, respectively. The angles of the scenario parameters of the indoor environment are $m_v = 20^\circ$, $m_h = 20^\circ$ and $\sigma_v = 30^\circ$, $\sigma_h = 30^\circ$, respectively. The antenna branch power ratio is MEG1/MEG2. In a good diversity system, the power levels of the signals received by the two antennas are similar. The ECC (ρ_c) between the two antennas can be calculated from the following complex correlation coefficient.

$$\rho_c = \frac{\int_0^{2\pi} \int_0^\pi A_{12}(\theta, \phi) \sin \theta d\theta d\phi}{\sqrt{\int_0^{2\pi} \int_0^\pi A_{11}(\theta, \phi) \sin \theta d\theta d\phi \int_0^{2\pi} \int_0^\pi A_{22}(\theta, \phi) \sin \theta d\theta d\phi}} \quad (5)$$

$$A_{mn} = XPR \cdot E_{\theta,m}(\theta, \phi) E_{\theta,n}^*(\theta, \phi) P_\theta(\theta, \phi) + E_{\phi,m}(\theta, \phi) E_{\phi,n}^*(\theta, \phi) P_\phi(\theta, \phi) \quad (6)$$

where E_θ and E_ϕ denote the θ and ϕ polarized electric fields of the antennas. The correlation coefficient of the signals is related to the propagation environment and the radiated far-field characteristics. The relationship between the complex cross-correlation coefficient ρ and the ECC (ρ_c) is obtained with $|\rho|^2 \cong \rho_c$.

1. Measured Result of the MIMO Antenna with the Dipole Antenna with an Omni-directional Pattern

Fig. 7 shows the measured isolation (S_{12} , S_{13} , and S_{14}) and the reflection coefficient (S_{11} , S_{22} , S_{33} , and S_{44}) of the MIMO an-

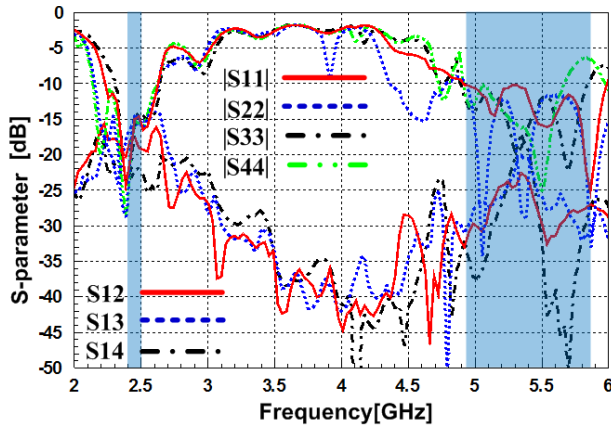


Fig. 7. S -parameter of the dipole antenna.

tenna. The return losses are less than -10 dB over the operating frequency band (2.4–2.48 GHz and 4.905–5.845 GHz). The proposed dipole antenna has a sufficiently broad bandwidth to satisfy the full band set by IEEE 802.11 standards. The feed point distance from the primary antenna is $0.67\lambda_g$ (80 mm) at the 2.4 GHz band for best isolation. The isolation is below -15 dB over the operating frequency band. However, in the case of S_{13} (isolation), it has good isolation compared to other ports, as the distance between port 1 and port 3 is longer than that between ports 1 and 2 or ports 1 and 4. Fig. 8 shows the measured radiation patterns of the proposed antenna according to the ports. In addition, Fig. 8 shows the radiation patterns in the Y-X plane ($0^\circ \leq \Phi \leq 360^\circ$) and X-Z ($0^\circ \leq \theta \leq 360^\circ$) plane at 2.44 GHz and 5.4 GHz. The radiation pattern of the proposed dipole antenna shows omni-directional characteristics and the measured peak gains of the ports are similar. Fig. 9 shows the measured peak gains and radiation efficiencies of the dipole antennas in the operating frequency bands. The peak gain of each port is 4.6–5.07 dBi at the center frequency (2.44 GHz) of the 2.4 GHz band and 6.24–6.5 dBi at the center frequency (5.4 GHz) of the 5 GHz band. The radiation efficiencies of each port are higher than 69% at 2.44 GHz and 66% at 5.4 GHz. The results show that the dual-band omni-directional antenna achieves a high antenna gain and provides a wide bandwidth while maintaining a compact size. Table 1 shows ECC characteristics of the dipole antennas according to the frequency. The ECC can be calculated from the S -parameter with (5). The isolation (S_{12}) improves as the distance between the proposed antennas increases. The ECC value for the high band (i.e., the 5.4 GHz band) is lower than that for the low band (i.e., the 2.42 GHz band), as the spatial separation of the two antennas is large at high frequencies ($>1\lambda$). The measurement results of diversity parameters for the dipole antenna using a Gaussian spread are shown in Table 2. The MEG ratio is close to 1 dB. The MEG values of each antenna are less than 0.1 dB [18]. As expected, the value of the MEG ratio between

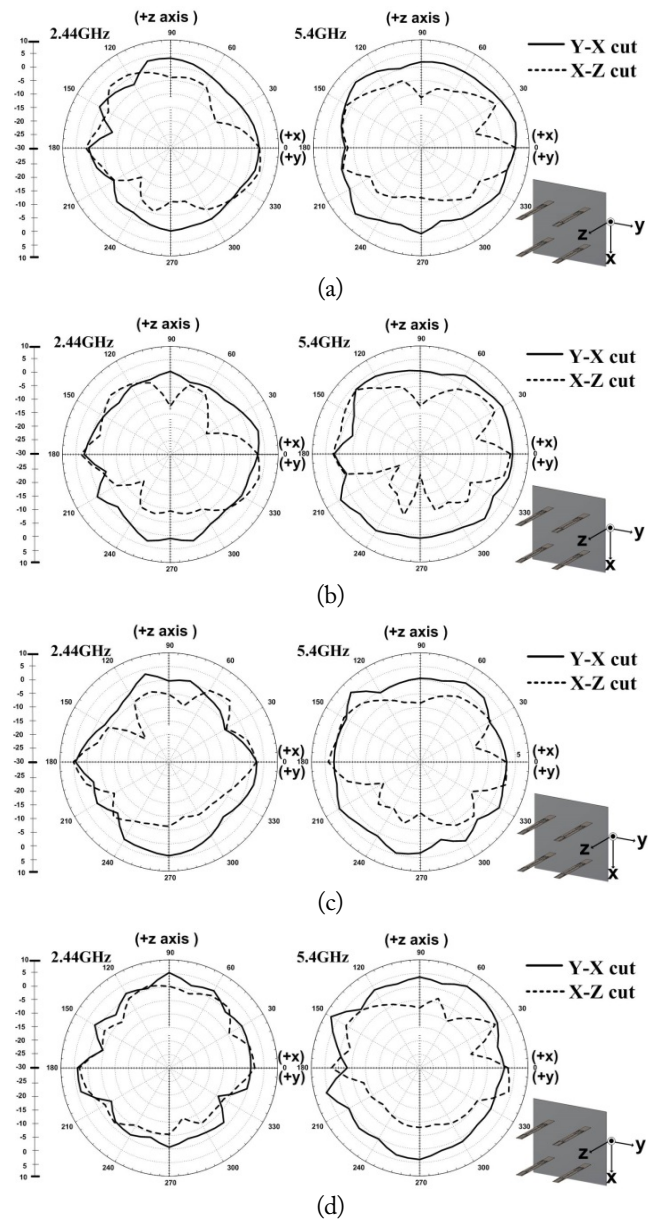


Fig. 8. Radiation pattern of the dipole antenna: (a) port 1, (b) port 2, (c) port 3, and (d) port 4.

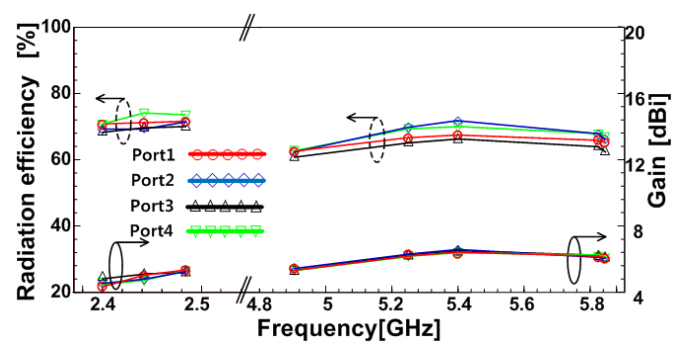


Fig. 9. Measured gain and radiation efficiency characteristics of the dipole antennas.

port 1 and port 3 performs better compared to the MEG ratio with other ports. The other two MEG ratios for ports 1 and 2

Table 1. Measured ECC characteristics of the dipole antenna according to the frequency

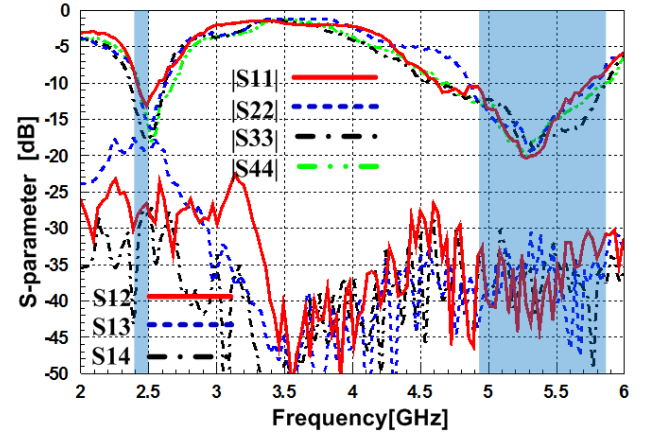
Freq. (GHz)	Feed		
	Port1/Port2	Port1/Port3	Port1/Port4
2.4	0.03	0.02	0.043
2.42	0.038	0.025	0.055
2.48	0.041	0.03	0.054
4.095	0.032	0.031	0.067
5.25	0.024	0.023	0.031
5.45	0.027	0.014	0.023
5.75	0.015	0.009	0.019
5.845	0.013	0.007	0.021

and ports 1 and 4 show almost equally good characteristics. Each port has similar MEG values favorable for an independent channel in a multipath environment [25].

2. Measured Result of the MIMO Antenna with a Patch Antenna of in Directional Pattern

The measured reflection coefficient (S_{11}) of the proposed MIMO antenna is shown in Fig. 10. The distances between the antennas are $0.67\lambda_g$ (80 mm) at 2.4 GHz and $1.3\lambda_g$ (80 mm) at 5 GHz. The measured return-loss result is almost equal to that of the reference antenna. The S_{11} of the antennas is less than -10 dB (VSWR 2:1) at 2.4 GHz and 5 GHz. Patch antennas typically have a narrow bandwidth. However, the proposed antenna improved the bandwidth with the use of a coupled feed and a parasitic element structure at the operating frequency. The isolation between each feed is also less than -15 dB over the operating band. The isolation (S_{13}) is better than the isolation between other ports like a dipole. In addition, the isolation performance (S_{12}) in the parallel condition is better than that in the series (S_{14}) condition due to the distribution of the E/H-field. When the proposed antennas are located in a series, the E-field is created by a positive charge and a negative charge like a dipole at the center. As a result, the main beams are directed toward each other face-to-face due to the electric field. When the proposed antennas are parallel to one another, the main beam is relatively directed in the opposite direction plane because the H-field is canceled at the center [26].

Fig. 11 shows the radiation patterns in the azimuth (Y-Z


 Fig. 10. S -parameter of the patch antenna.

plane) and the elevation (X-Z plane) planes at 2.44 GHz and 5.4 GHz. In the elevation plane pattern, the angle starts from the +x direction. The major lobe directed the signal at the +z direction (90°) and in the azimuth plane, the angle starts from the +y direction.

Fig. 12 shows the measured peak gains and radiation efficiencies of the patch antennas in the operating frequency bands. The peak gain of each port is 6.7–7.24 dBi at 2.44 GHz and 10.26–10.9 dBi at 5.4 GHz. The radiation efficiencies of each port are higher than 80% at both 2.44 GHz and 5.4 GHz frequency. The correlation characteristics show a low ECC (<0.5) at 2.42 GHz and 5.4 GHz, respectively. The measurement results of diversity parameters for the patch antenna using a Gaussian spread are shown in Tables 4. It shows an equally good MEG value with a low ECC as the result of the dipole antenna. As a result, the best correlation and MEG are obtained for the MIMO system.

3. Measured Result of the Throughput Performance of the Wireless Networks

In data communication systems, throughput is traditionally defined as the ratio of the amount of data over the time needed to transfer it. Thus, we use the general formula:

$$\text{Throughput} = \frac{\text{Received data}}{\text{Transmission time}} \quad (7)$$

Table 2. Measured results of diversity parameters for the dipole antenna using Gaussian spread

Freq. (GHz)	Value	MEG (dB)				MEG ratio (dB)				
		MEG1 Port1&2	MEG2 Port1&2	MEG1 Port1&3	MEG3 Port1&3	MEG1 Port1&4	MEG4 Port1&4	Port1/Port2	Port1/Port3	Port1/Port4
2.44	Uniform/Gaussian	-3.685	-3.925	-3.685	-3.497	-3.685	-4.067	0.939	1.054	0.904
5.4	Uniform/Gaussian	-4.237	-4.04	-4.237	-4.046	-4.237	-4.459	1.048	1.047	0.950

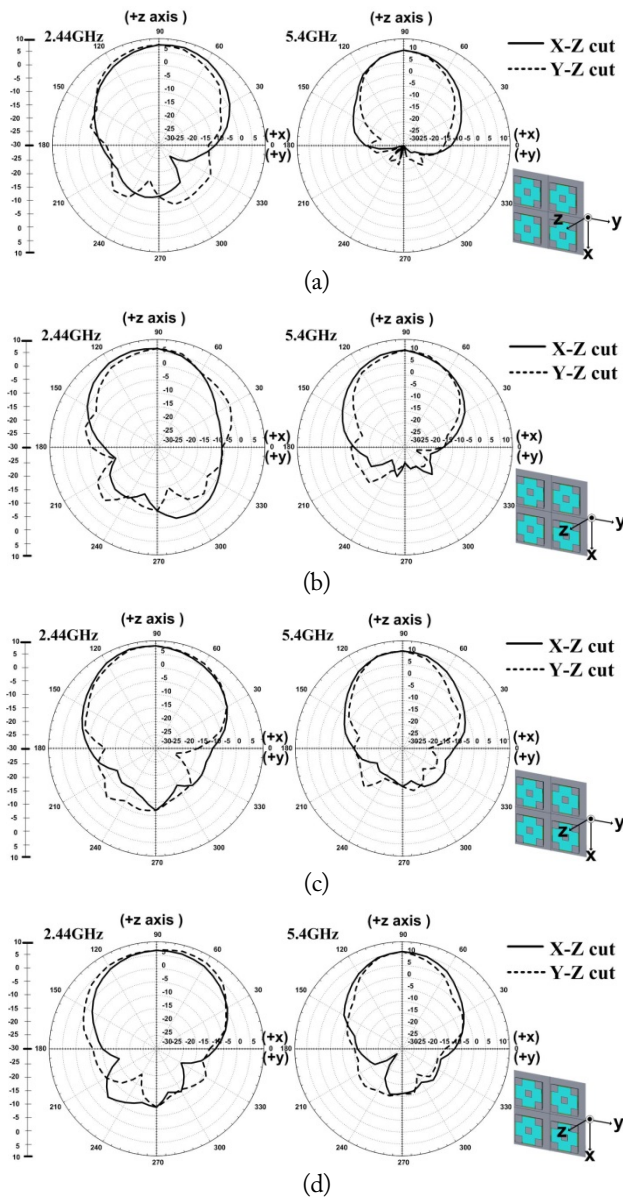


Fig. 11. Radiation pattern of the patch antenna: (a) port 1, (b) port 2, (c) port 3, and (d) port 4.

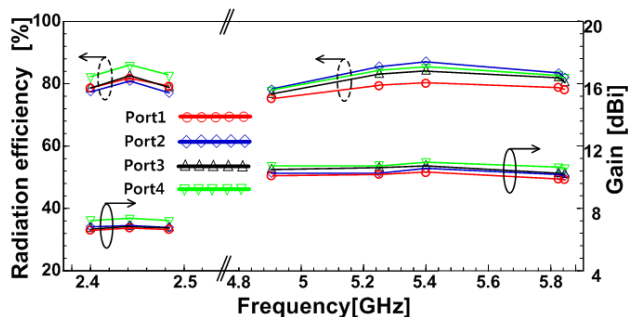


Fig. 12. Measured gain and radiation efficiency characteristics of the patch antennas.

We define “received data” as the amount of 802.11 payload data successfully received by the destination node expressed in number of bits. The test was set up in a small room in a general

Table 3. Measured ECC characteristics of the patch antenna according to the frequency

Freq. (GHz)	Feed		
	Port1/Port2	Port1/Port3	Port1/Port4
2.4	0.037	0.027	0.092
2.42	0.027	0.018	0.068
2.48	0.015	0.018	0.021
4.095	0.037	0.003	0.029
5.25	0.012	0.003	0.021
5.45	0.002	0.001	0.006
5.75	0.002	0.001	0.003
5.845	0.001	0.001	0.006

office. The office’s dimensions are 6.3 m × 9 m, as shown in Fig. 13(a). The RX is composed of a MIMO antenna with 802.11n support. The dipole and patch antennas of the TX are configured based on a ceiling mount as a general structure. The throughput depends heavily on its environment, including the distance between the client and the IAP, the presence of radio channel interference, obstacles such as furniture, walls etc., and signal reflections like scattering. Therefore, it was necessary to limit the impact of external factors that interfere with the IAP. Any radio devices that might interfere with the throughput were removed, and the internal and external conditions, including all physical obstacles, the RF environment, and temperature conditions, were fixed.

We focused on comparing the performance of the throughput according to three main factors: the beam pattern, the antenna gain, and the isolation between the ports. A block diagram of the throughput measurements is shown in Fig. 13(b). All tests were measured using the Chariot program of Ixia Inc. The PC 1 at TX is composed of Endpoint 1 and the IAP with 2 × 2 MIMO, and the PC 2 at RX is composed of Endpoint 2 and the IAP with the proposed antenna. In addition, the IP addresses differed for the test runs. For example, when 192.168.0.1 was assigned to Endpoint 1 in the test run, Endpoint 2 was assigned to 168.168.0.2. The IAP of PC 1 sends a test signal to Endpoint 1. When all the endpoint pairs were ready, the two endpoint computers executed the test. The Endpoint 1 computer collects the test results and timing records and sends them to IxChariot [27, 28]. The IAP chipset at the TX was the RTL8197D (Realtek Inc.) and the chipset of the wireless LAN card at the RX was RTL8812AU (Realtek Inc.).

In order to equalize the conditions, we used the same PC and IAPs with wireless cards for all the tests, and the same packets with loads of 9.53 Mbytes. Fig. 14(a) shows the graph of a typical Transmission Control Protocol (TCP) throughput test with the dipole antenna, which is an omni-directional radiation pattern. It is necessary to compare data throughput according to

Table 4. Measured results of diversity parameters for the patch antenna using Gaussian spread

Freq. (GHz)	Value	MEG (dB)				MEG ratio (dB)				
		MEG1 Port1&2	MEG2 Port1&2	MEG1 Port1&3	MEG3 Port1&3	MEG1 Port1&4	MEG4 Port1&4	Port1/Port 2	Port1/Port 3	Port1/Port 4
2.44	Uniform/ Gaussian	-5.143	-4.879	-5.143	-5.06	-5.143	-4.623	1.054	1.016	1.112
5.4	Uniform/ Gaussian	-5.425	-5.895	-5.425	-5.554	-5.425	-6.045	0.920	0.976	0.897

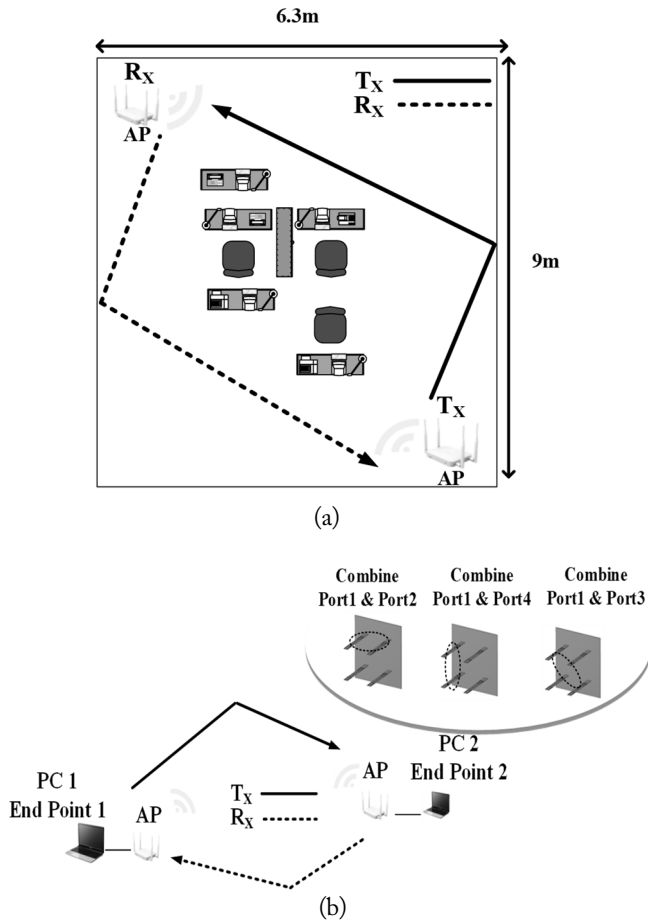


Fig. 13. The throughput measurement of wireless networks: (a) experimental and (b) block diagram.

the directional and omni-directional patterns, which are typical radiation patterns for the general APs. The test was conducted consistently according to the different types of radiation patterns showing good isolations in the indoor condition. The experiments were run three per port, and the average value was recorded. The data packet cycle was run 180 times. Using a large time unit, we measured the average capacity of the IAP [29]. When the antennas at port 1 and port 2 were combined, the average throughput was found to be 139.13 Mbps. The measured throughput data of ports 1 and 3 combined was 149.8 Mbps, and the throughput data measured by combining ports 1 and 4 was 141.6 Mbps. The results of the TCP performance

was similar to that of the port when isolation was high (less than -15 dB) over the operating frequency band; however, ports 1 and 3 had slightly better TCP performance compared to the other ports, as the isolation between ports 1 and 3 was better than that for the other ports.

Fig. 14(b) shows the typical TCP performance of the IAP with a patch antenna, which has a typical directional pattern. When the antennas at ports 1 and 2 were combined, the average throughput was 122.4 Mbps. The measured throughput data of ports 1 and 3 combined was 126.5 Mbps, and the throughput data measured by combining ports 1 and 4 was 123.5 Mbps. In wireless telecommunications, multipath is the result of radio

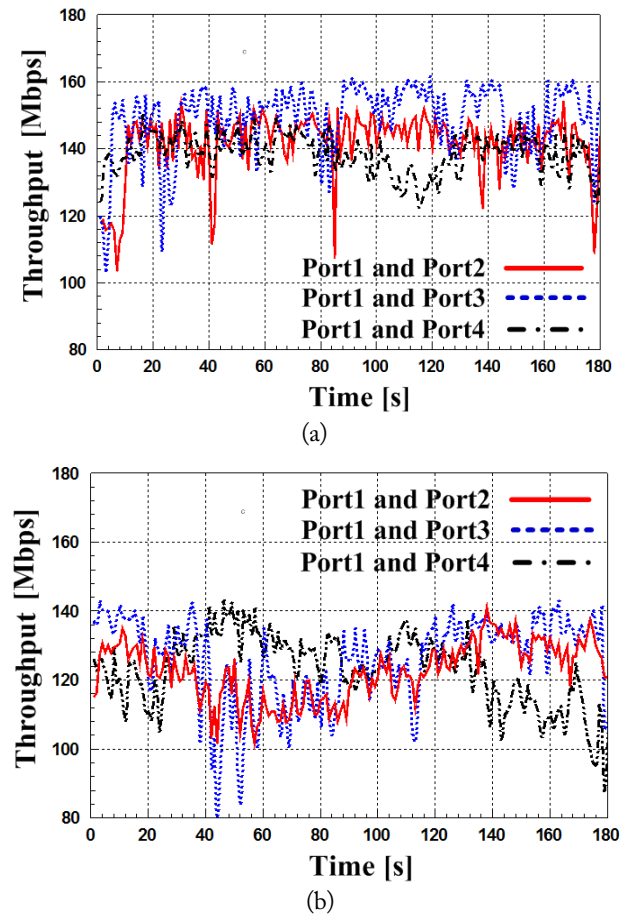


Fig. 14. Typical TCP performance of the IAP: (a) dipole antenna and (b) patch antenna.

signals reaching the receiving antenna by two or more paths. In multipath environments, the diversity of the antennas involved affects the throughput data. The patch antenna with a relatively high gain has poor throughput data compared to the dipole antenna in an office environment. As the total power received by the antenna is the sum over the arriving plane waves from the distribution of the angles, it is shown that the directive antenna as a patch enhances a relatively small number of incident waves. Therefore, the overall power is dependent on the angle of arrival and that received by the directive antenna is lower [15]. In an office environment, the dipole antenna with omnidirectional characteristics covers a wide area and has a higher maximum throughput compared to patch antennas.

IV. CONCLUSION

In this paper, we designed a wide and dual-band MIMO antenna with an omnidirectional and directional radiation pattern for premium IAPs. We analyzed the MIMO performance using two types of antennas in the 2×2 MIMO system. The optimized frequencies were 2.4–2.4835 GHz and 4.905–5.845 GHz. In order to analyze the proposed MIMO antenna for the IAPs, we simulated and measured the isolation. The isolation was below -15 dB. The proposed MIMO antenna has a low ECC (<0.5) with low correlations in a comparative analysis. The values of the MEG between the two antenna elements are less than 0.5 dB. The proposed MIMO antenna supports 802.11n and is capable of providing a high-quality IAP. Finally, we analyzed the throughput performance according to the radiation pattern, the antenna gain, and the isolation using the proposed antenna in an office area. We have shown that the MIMO antenna with an omnidirectional pattern can improve throughput data in office environments with multipath. The results of this study should apply to 4×4 MIMO systems and provide guidance on the selection of suitable types of antennas for certain environments and particular purposes.

This work was supported by a grant from the National Research Foundation of Korea, which is funded by the Korean government (No. 2016R1D1A1B02012957).

REFERENCES

- [1] J. Mietzner, R. Schober, L. Lampe, W. H. Gerstacker, and P. A. Hoeher, "Multiple-antenna techniques for wireless communications: a comprehensive literature survey," *IEEE Communications Surveys and Tutorials*, vol. 11, no. 2, pp. 87–105, 2009.
- [2] R. Tian, B. K. Lau, and Z. Ying, "Multiplexing efficiency of MIMO antennas," *IEEE Antennas and Wireless Propagation Letters*, vol. 10, pp. 183–186, 2011.
- [3] S. Lim, W. C. Choi, and J. Y. Yoon, "Miniaturized radio frequency choke using modified stubs for high isolation in MIMO systems," *Journal of Electromagnetic Engineering and Science*, vol. 15, no. 4, pp. 219–223, 2015.
- [4] I. S. Yeom, and C. W. Jung, "Compact dual-band multiple input multiple output antenna with high isolation performance," *Microwave and Optical Technology Letters*, vol. 52, no. 12, pp. 2808–2811, 2010.
- [5] D. Halperin, W. K. Hu, A. Sheth, and D. Wetherall, "802.11 with multiple antennas for dummies," *ACM SIGCOMM Computer Communication Review*, vol. 40, no. 1, pp. 19–25, 2010.
- [6] O. Tze-Meng, T. K. Geok, and A. W. Reza, "A dual-band omnidirectional microstrip antenna," *Progress in Electromagnetics Research*, vol. 106, pp. 363–376, 2010.
- [7] Z. Zhang, M. F. Iskander, and J. C. Langer, and J. Mathews, "Dual-band WLAN dipole antenna using an internal matching circuit," *IEEE Transactions on Antennas and Propagation*, vol. 53, no. 5, pp. 1813–1818, 2005.
- [8] Y. J. Wu, B. H. Sun, J. F. Li, and Q. Z. Liu, "Triple-band omnidirectional antenna for WLAN application," *Progress in Electromagnetics Research*, vol. 76, pp. 477–484, 2007.
- [9] S. He and J. Xie, "Analysis and design of a novel dual-band array antenna with a low profile for 2400/5800-MHz WLAN systems," *IEEE Transactions on Antennas and Propagation*, vol. 58, no. 2, pp. 391–396, 2010.
- [10] D. C. Chang, B. H. Zeng, and J. C. Liu, "High performance antenna array with patch antenna elements," in *PIERS Proceedings*, Xian, China, 2010, pp. 710–713.
- [11] G. Bianchi, "Performance analysis of the IEEE 802.11 distributed coordination function," *IEEE Journal on Selected Areas in Communication*, vol. 18, no. 3, pp. 535–547, 2000.
- [12] M. Ekpenyong and J. Isabona, "Modeling throughput performance in 802.11 WLAN," *International Journal of Computer Science Issues*, vol. 7, no. 3, pp. 16–22, 2000.
- [13] C. Na, J. K. Chen, and T. S. Rappaport, "Measured traffic statistics and throughput of IEEE 802.11 b public WLAN hotspots with three different applications," *IEEE Transactions on Wireless Communications*, vol. 5, no. 11, pp. 3296–3305, 2006.
- [14] G. Rajagopalan, "802.11n client throughput performance," Aruba Networks, Sunnyvale, CA, 2008.
- [15] D. Wittwer, S. Azulay, M. Ellioot, M. Martiskainen, and S. Krupa, "The influence of antenna directivity on physical layer simulations of 802.11n devices," in *Proceedings of*

- IEEE International Conference on Microwaves, Communications, Antennas and Electronic Systems*, Tel Aviv, Israel, 2009, pp. 1–4.
- [16] S. Maci and G. B. Gentili, "Dual-frequency patch antennas," *IEEE Antennas and Propagation Magazine*, vol. 39, no. 6, pp. 13–20, 1997.
- [17] P. S. Kildal, K. Rosengren, J. Byun, and J. Lee, "Definition of effective diversity gain and how to measure it in a reverberation chamber," *Microwave and Optical Technology Letters*, vol. 34, no. 1, pp. 56–59, 2002.
- [18] Q. Wang, H. Zhang, D. Plettemeier, E. Ohlmer, and G. Fettweis, "Design and performance evaluation of handset MIMO antenna prototypes," in *Proceedings of International ITG Workshop on Smart Antennas*, Bremen, Germany, 2010, pp. 375–382.
- [19] B. Guo, O. Sotoudeh, G. Zhou, and Y. Cheng, "Antenna diversity for a mobile terminal: theory, simulation and measurement," in *Proceedings of IEEE Global Telecommunications Conference*, Honolulu, HI, 2009, pp. 1–6.
- [20] P. S. Kildal and K. Rosengren, "Correlation and capacity of MIMO systems and mutual coupling, radiation efficiency, and diversity gain of their antennas: simulations and measurements in a reverberation chamber," *IEEE Communication Magazine*, vol. 42, no. 12, pp. 104–112, 2004.
- [21] I. Yeom, J. M. Kim, and C. W. Jung, "Dual-band slot-coupled patch antenna with broad bandwidth and high directivity for WLAN access point," *Electronics Letters*, vol. 50, no. 10, pp. 726–728, 2014.
- [22] A. Majumder, "Rectangular microstrip patch antenna using coaxial probe feeding technique to operate in S-band," *International Journal of Engineering Trends and Technology (IJETT)*, vol. 4, no. 4, pp. 1206–1210, 2013.
- [23] C. A. Balanis, *Antenna Theory: Analysis and Design*, 3rd ed. Hoboken, NJ: John Wiley & Sons, 2005.
- [24] T. Taga, "Analysis for mean effective gain of mobile antennas in land mobile radio environments," *IEEE Transactions on Vehicular Technology*, vol. 39, no. 2, pp. 117–131, 1990.
- [25] Qualcomm, "Diversity Antenna Design Guidelines," Release 7.10 913-0949-04 Rev. A, 2006.
- [26] I. Yeom, H. Kim, J. Jung, and C. W. Jung, "Analysis of spatial/polarization diversity using a broadband slot-coupled patch antenna for the WLAN 802.11 A/B/G/N access point," *Microwave and Optical Technology Letters*, vol. 57, no. 5, pp. 1042–1048, 2015.
- [27] Ixia, "IxChariot user guide," 80-V8782-5 Rev. B, 2006.
- [28] E. Pelletta, "Maximum throughput of IEEE 802.11 access points: test procedure and measurements," Master's thesis, Royal Institute of Technology, Stockholm, Sweden, 2004.
- [29] A. L. Wijesinha, Y. T. Song, M. Krishnan, V. Mathur, J. Ahn, and V. Shyamasundar, "Throughput measurement for UDP traffic in an IEEE 802.11g WLAN," in *Proceedings of the 6th International Conference on Software Engineering, Artificial Intelligence, Networking and Parallel/Distributed Computing*, Towson, MD, 2005, pp. 220–225.

Insu Yeom



received his B.S. and M.S. degrees in electrical engineering from Seoul National University of Science and Technology (SeoulTech), Seoul, Korea, in 2002 and 2011. He also obtained a Ph.D. in electrical engineering from SeoulTech, Korea, in 2017. His current research interest focuses on MIMO antennas, reconfigurable antennas, and RF energy for heating systems.

Young-Bae Jung



received a B.S. in radio science and engineering from Kwangwoon University, Seoul, Korea, in 1998, and M.S. and Ph.D. degrees in information and communications engineering from Korea Advanced Institute of Science and Technology (KAIST), Daejeon, Korea, in 2001 and 2009, respectively. From 2001 to 2011, he was with the Electronics and Telecommunications Research Institute (ETRI), Daejeon, Korea, as a senior researcher. From March 2011, he has been an associate professor in the Department of Electronics and Control Engineering, Hanbat National University, Daejeon, Korea. His work is focused on active phased array antenna systems and next generation mobile base-station antennas. His research interests include active phased array antenna systems and active/passive components in the field of RF and microwave.

Chang Won Jung



received his B.S. degree in radio science and engineering from Kwangwoon University, Korea, in 1997 and his M.S. degree in Electrical Engineering from the University of Southern California, Los Angeles, USA, in 2001. He also obtained a Ph.D. in electrical engineering and computer science from the University of California, Irvine, USA, in 2005. Since 2008, he has been a professor with the Graduate

School of Nano·IT·Design Fusion, Seoul National University of Science and Technology. From 1997 to 1999, he was a research engineer in the wireless communication department of LG Information and Telecommunication in Korea. From 2005 to 2008, he was a senior research engineer in the communication laboratory of Samsung Advanced Institute of Technology, Korea. His research interests include antennas for MIMB communication systems, multifunctional reconfigurable antennas, EMI/EMC, millimeter-wave applications, wireless power transfer for energy harvesting, transparent RF passive components etc.

Metaheuristic Optimization Techniques for an Electromagnetic Multilayer Radome Design

Trung Kien Nguyen¹ · In-Gon Lee¹ · Obum Kwon² · Yoon-Jae Kim² · Ic-Pyo Hong^{1,*}

Abstract

In this study, an effective method for designing an electromagnetic multilayer radome is introduced. This method is achieved by using ant colony optimization for a continuous domain in the transmission coefficient maximization with stability for a wide angle of incidence in both perpendicular and parallel polarizations in specific X- and Ku-bands. To obtain the optimized parameter for a C-sandwich radome, particle swarm optimization algorithm is operated to give a clear comparison on the effectiveness of ant colony optimization for a continuous domain. The qualification of an optimized multilayer radome is also compared with an effective solid radome type in transmitted power stability and presented in this research.

Key Words: Ant Colony Optimization, Electromagnetic Multilayer Radome Design, Metaheuristic Optimization Algorithm, Particle Swarm Optimization, Transmission Coefficient Maximization.

I. INTRODUCTION

The problem of an electromagnetic multilayer dielectric design optimization for a frequency band and a desired range of incident angles has been introduced in recent years using such metaheuristic optimization algorithms as the genetic algorithm [1, 2], particle swarm optimization (PSO) [3, 4], or a hybrid algorithm that combines ant colony optimization (ACO) with the microgenetic algorithm [5]. In this study, an effective algorithm presented by Socha and Dorigo [6] in 2008 called ant colony optimization for a continuous domain (ACO_R) is applied to design a C-sandwich radome [7] with an applicable range of incident angle (0°–70°) in both the transverse electric (TE) and transverse magnetic (TM) modes for the X- and Ku-bands. To validate the ACO_R algorithm in a multilayer radome

design optimization, the performance of the transmission coefficient characteristics of the C-sandwich radome design optimized by ACO_R has been compared with a conventional analysis method (i.e., a simpler and lower-cost analysis) that approximates multilayer radomes by a solid radome with an effective medium approximation (EMA) [8, 9]. Then, the performance of ACO_R is compared with a general optimization algorithm used in electromagnetic characteristic design (i.e., PSO). This study is organized as follows: Section II is an overview of the ACO_R algorithm, which uses a boundary value method to evaluate the transmission coefficient of a multilayer radome. Section III examines the fitness function and compares the optimization results obtained by ACO_R and PSO. The simulation results and the transmitted power stability are compared with an effective solid radome, and the results are discussed. The conclusion is

Manuscript received July 26, 2018 ; Revised October 3, 2018 ; Accepted October 17, 2018. (ID No. 20180726-055J)

¹Department of Information & Communication Engineering, Kongju National University, Cheonan, Korea.

²Agency for Defense Development, Daejeon, Korea.

*Corresponding Author: Ic-Pyo Hong (e-mail: iphong@kongju.ac.kr)

This is an Open-Access article distributed under the terms of the Creative Commons Attribution Non-Commercial License (<http://creativecommons.org/licenses/by-nc/4.0>) which permits unrestricted non-commercial use, distribution, and reproduction in any medium, provided the original work is properly cited.

© Copyright The Korean Institute of Electromagnetic Engineering and Science. All Rights Reserved.

provided in Section IV.

II. METHODS

1. Ant Colony Optimization for a Continuous Domain

Originally, ACO was introduced in 1992 by Dorigo [10], and it has been used to solve many combinational optimization problems consisting of a set of discrete decision variables. The idea of applying ACO in solving the continuous optimization problem was presented in 2008 by Socha and Dorigo [6]. The flowchart of the ACO_R algorithm is illustrated in Fig. 1.

In ACO_R, the solutions are kept and sorted in a solution archive (Fig. 2), in which the associated weight of solution l defined in Eq. (1) represents the strength of the solution in producing new solutions.

$$\omega(l) = \frac{1}{qk\sqrt{2\pi}} e^{-\frac{(l-1)^2}{2q^2k^2}}. \quad (1)$$

To generate new solutions, a kernel is selected by probability that is computed for each group as in Eq. (2).

$$p(l) = \frac{\omega(l)}{\sum_{j=1}^k \omega(j)}. \quad (2)$$

Roulette wheel selection [11] is applied to select a solution kernel. Each probability $p(l)$ is presented as a proportion of the wheel (Fig. 3), and a random selection process is made similarly to rotate the roulette wheel. An m new random number

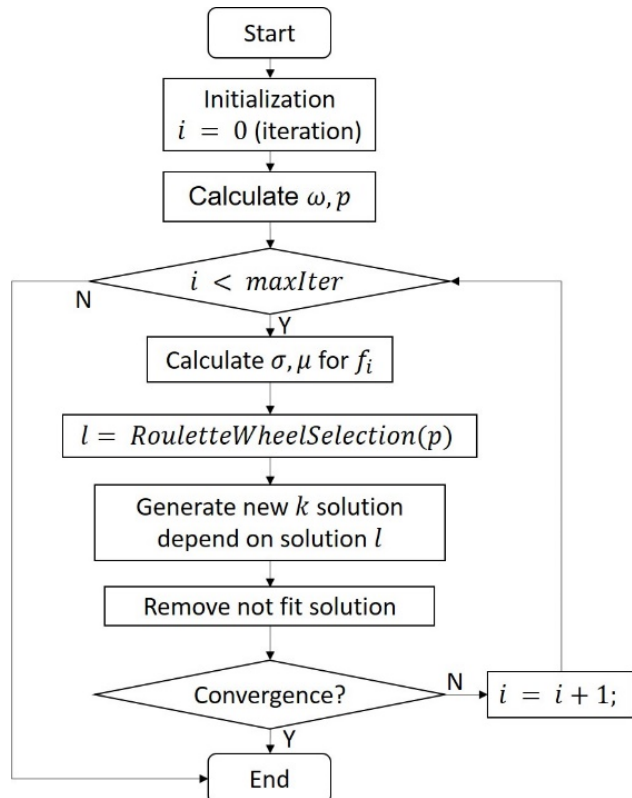


Fig. 1. Flowchart of ACO_R algorithm.

s_1^1	s_1^2	...	s_1^i	...	s_1^n	$\omega(1)$	$f(1)$
s_2^1	s_2^2	...	s_2^i	...	s_2^n	$\omega(2)$	$f(2)$
\vdots	\vdots	\ddots	\vdots	\ddots	\vdots	\vdots	\vdots
s_l^1	s_l^2	...	s_l^i	...	s_l^n	$\omega(l)$	$f(l)$
\vdots	\vdots	\ddots	\vdots	\ddots	\vdots	\vdots	\vdots
s_k^1	s_k^2	...	s_k^i	...	s_k^n	$\omega(k)$	$f(k)$

Fig. 2. Solution archive of the ACO_R algorithm with s_i^l as the value of parameter i in group l and the objective value $f(l)$ with associated weight $\omega(l)$.

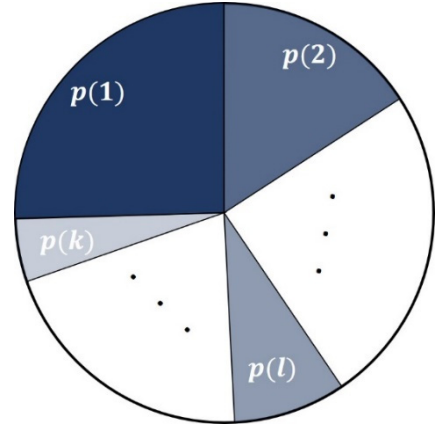


Fig. 3. Roulette wheel with a probability of solution $p(l)$ as the proportion of the wheel.

group according to the parameterized normal distribution is used with mean (μ_i^l) and standard deviation (σ_i^l) for ant i in group l .

$$\mu_i^l = s_i^l. \quad (3)$$

$$\sigma_i^l = \xi \sum_{j=1}^k \frac{|s_j^l - s_i^l|}{k-1}. \quad (4)$$

$\xi > 0$ is a constant parameter that is similar to the pheromone evaporation rate in ACO [10]. Then, m new solutions are added to the solution archive and re-ordered. Non-fit solutions are removed, and only the k best ones are kept after each iteration.

2. Transmission Coefficient Characteristic of the C-Sandwich Radome

A C-sandwich radome, which is a multilayer radome (style d) [7], is considered in this work. The sandwich wall has five layers that were developed to cover an antenna array operating in a wide-band frequency range. The C-sandwich construction consists of three skins that are interleaved by two cores. Typically, the relative permittivity of skin is greater than that of the core. To guarantee that the input and output of the propagation wave

are equal, a C-sandwich wall is designed with the first and last skins having the same thickness, and the widths of the two cores are the same as well. To fabricate a radome, the thickness of each layer is designed as the multiple of plies. The propagation wave on the radome with layer i has thickness d_i , relative permittivity ε_i , loss tangent $\tan\delta_i$, and refractive index n_i . The F_j ($j \in [1,7]$)/ B_k ($k \in [1,6]$) are the forward and backward propagation waves, respectively. The forward and backward fields at the first left interface are related to Eq. (5).

$$\begin{bmatrix} F_1 \\ B_1 \end{bmatrix} = \prod_{i=1}^5 \frac{1}{\tau_i \tau_6} \begin{bmatrix} e^{jk_i d_i} & r_i * e^{-jk_i d_i} \\ r_i * e^{jk_i d_i} & e^{-jk_i d_i} \end{bmatrix} \times \begin{bmatrix} 1 & r_6 \\ r_6 & 1 \end{bmatrix} \begin{bmatrix} F_7 \\ 0 \end{bmatrix} \quad (5)$$

$\tau_i = 1 + r_i$ and r_i is the intrinsic reflection coefficient of each interface and is calculated by the Fresnel equation. If one uses the formula in Eq. (5) and simplifies it to Eq. (6), the transmission coefficient can be obtained by Eq. (7).

$$\begin{bmatrix} F_1 \\ B_1 \end{bmatrix} = \begin{bmatrix} A_{11} & A_{12} \\ A_{21} & A_{22} \end{bmatrix} \begin{bmatrix} F_7 \\ 0 \end{bmatrix}. \quad (6)$$

$$T = \frac{F_7}{F_1} = \frac{1}{A_{11}}. \quad (7)$$

III. RESULTS AND DISCUSSION

1. Fitness Function

The main objective of this research is to maximize the transmission coefficient of a multilayer structure radome, which is calculated by Eq. (7) in a specific frequency band with various angles of incidence in both the TE and TM modes. To ensure the stability of the transmission coefficient, the following objective function is considered for optimization:

$$\text{maximize } F = \{\min[T(f, \theta)]\}^2 * 100, \quad (8)$$

where $T(f, \theta)$ is the transmission coefficient at frequency f and incident angle θ .

2. Optimization Design Result

The optimized thickness design is compared with an effective solid radome type with a half-wavelength thickness. The transmitted power is 80% greater in both polarizations, and the wide angle of incidence is the target of optimization. The design of the multilayer radome structure for optimization is shown in Table 1.

According to the EMA method, a multilayer radome can be approximated by its effective material property. The effective relative permittivity (ε_{eff}) of the radome after optimization is calculated by Eq. (9), where n is the total number of layers, and d_i , ε_i are the thickness and permittivity of layer i , respectively. By using a half-wavelength equation to assume the thickness of the effective medium, Eq. (10) can be used to compute

Table 1. C-sandwich radome layer properties

Layer	Permittivity	Loss tangent	Thickness (mm)	Step/ply (mm)
Skin 1	4.4	0.016	0.48–2.4	0.24
Core 1	1.1	0.001	2–9	0.1
Skin 2	4.4	0.016	2.4–9.6	0.24
Core 2	1.1	0.001	2–9	0.1
Skin 3	4.4	0.016	0.48–2.4	0.24

the thickness of the effective half-wavelength solid-type radome at a resonant frequency of 10 GHz for the X-band and 15 GHz for the Ku-band with an angle of incidence $\theta = 70^\circ$.

$$\varepsilon_{eff} * \sum_{i=1}^n d_i = \sum_{i=1}^n \varepsilon_i * d_i. \quad (9)$$

$$d_{eff} = \frac{\lambda}{2 * \sqrt{\varepsilon_{eff} - \sin(\theta)^2}}. \quad (10)$$

The first optimized radome of this study is the design for the X-band (8–12 GHz) frequency. According to a comparative analysis with 30 execution times (Table 2), ACO_R requires less time (56.69 seconds) to reach the convergence than PSO (70.18 seconds). Fig. 4 presents the comparison of transmitted power stability between the optimized multilayer radome and the effective solid radome with the stability of a multilayer radome in various angles, with both TE and TM modes being under 10% change. The transmission coefficient characteristic of the C-sandwich radome after optimization is presented in Fig. 5 in the X-band.

To give a more effective decision, the same design properties of the multilayer radome are applied in the Ku-band (12–18 GHz). Table 3 shows the same result to demonstrate that ACO_R has better performance than PSO. Fig. 6 illustrates that the stability in the transmitted power of the optimized multilayer structure is less than 10%, which is outstanding compared with that of the effective solid radome. Fig. 7 shows the transmission coefficient of the optimized radome for the TE and TM modes in the Ku-band.

Table 2. Comparison of the 30 execution times between ACO_R and PSO for the X-band frequency

Detail	ACO _R	PSO
Skin 1 (mm)	0.72	0.72
Core 1 (mm)	5.0	5.0
Skin 2 (mm)	7.68	7.68
Core 2 (mm)	5.0	5.0
Skin 3 (mm)	0.72	0.72
Average time (s)	56.69	70.18
Convergent iteration	11	24

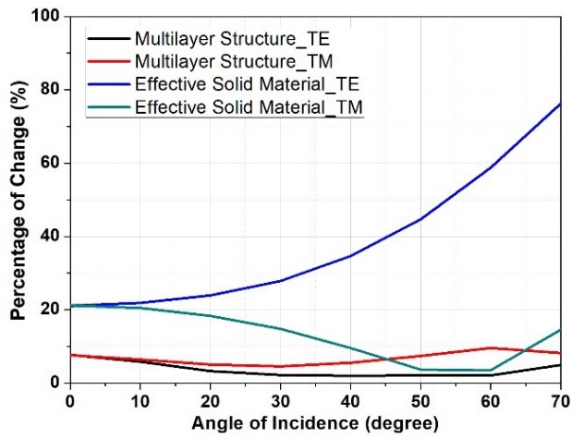


Fig. 4. Stability of the transmitted power of an optimized multilayer structure with an effective solid-type radome in the X-band.

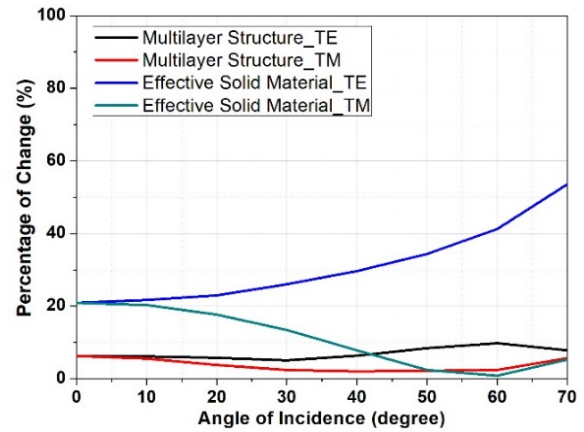


Fig. 6. Stability of the transmitted power of the optimized multilayer structure with an effective solid-type radome in the Ku-band.

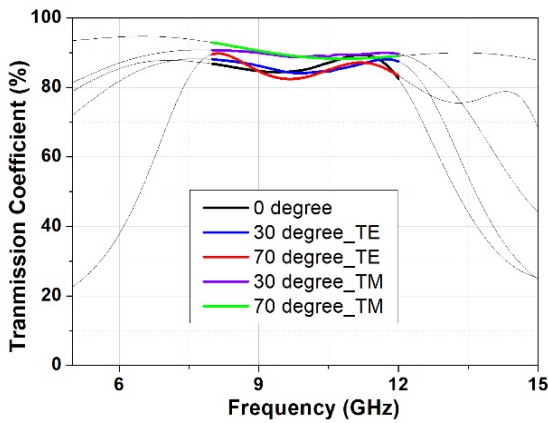


Fig. 5. Optimized transmission coefficient of the multilayer structure for the X-band.

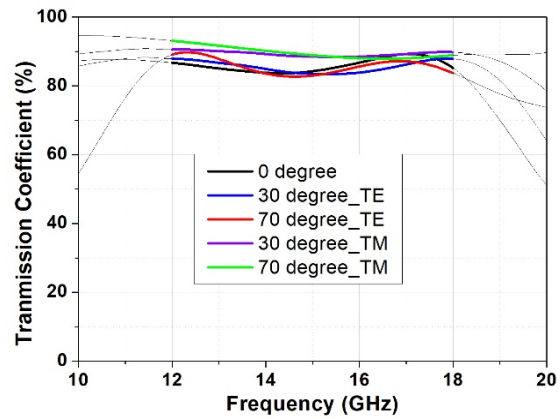


Fig. 7. Optimized transmission coefficient of the multilayer structure for the Ku-band.

According to the computed result, ACO_R gives a promising value in optimizing multi-objective problems applied in the electromagnetic multilayer radome design.

IV. CONCLUSION

A comparative study of two metaheuristic optimization algorithms, PSO and ACO_R for an electromagnetic multilayer ra-

Table 3. Comparison of the 30 execution times between ACO_R and PSO for the Ku-band frequency

Detail	ACO_R	PSO
Skin 1 (mm)	0.48	0.48
Core 1 (mm)	3.3	3.3
Skin 2 (mm)	5.04	5.04
Core 2 (mm)	3.3	3.3
Skin 3 (mm)	0.48	0.48
Average time (s)	64.13	71.86
Convergent iteration	12	24

dome design with various angles of incidence (0° – 70°) in the perpendicular and parallel polarizations for the X- and Ku-bands was presented. The simulation results obtained by ACO_R were compared with those of a trusted optimization, PSO. The results strongly confirm that ACO_R can be useful in the electromagnetic multilayer radome characteristic optimization. The stability for the transmission coefficient of the optimized structure is also guaranteed by ACO_R . In future works, the ACO_R algorithm will be improved to solve more complex frequency-selective surface design optimization problems such as the 3D frequency-selective surface screen design.

This work was supported by the Agency for Defense Development under contract (No. UD170044JD).

REFERENCES

[1] H. A. El-Hakim, K. R. Mahmoud, and A. Abdelaziz,

- "Design of compact double-layer microwave absorber for X-Ku bands using genetic algorithm," *Progress In Electromagnetics Research*, vol. 65, 157–168, 2016.
- [2] N. Lassouaoui, H. Ouslimani, and A. Priou, "Genetic algorithms for automated design of the multilayer absorbers in the X-band and incident angle range," in *Proceedings of 2008 Progress in Electromagnetics Research Symposium (PIERS), Hangzhou, China, 2008*, pp. 509–513.
- [3] K. W. Lee, I. P. Hong, B. J. Park, Y. C. Chung, and J. G. Yook, "Design of multilayer radome with particle swarm optimization," *The Journal of Korean Institute of Electromagnetic Engineering and Science*, vol. 21, no. 7, pp. 744–751, 2010.
- [4] S. Roy, A. Mahanti, S. D. Roy, and G. K. Mahanti, "Comparison of evolutionary algorithms for optimal design of broadband multilayer microwave absorber for normal and oblique incidence," *Applied Computational Electromagnetics Society Journal*, vol. 31, no. 1, pp. 79–84, 2016.
- [5] K. Chao, Y. Liu, and R. Yang, "Application of the hybrid algorithm combining ant colony optimization algorithm with microgenetic algorithm to the optimization of multilayered radar absorbing coating," in *Proceedings of International Conference on Microwave and Millimeter Wave Technology*, Nanjing, China, 2008, pp. 597–600.
- [6] K. Socha and M. Dorigo, "Ant colony optimization for continuous domains," *European Journal of Operational Research*, vol. 185, no. 3, pp. 1155–1173, 2008.
- [7] D. J. Kozakoff, *Analysis of Radome Enclosed Antennas*. Boston, MA: Artech House, 1997.
- [8] R. Lavin, "IEEE Phoenix Waves and Devices chapter," 2014; http://sites.ieee.org/phoenix-wad/files/2016/10/IEEE_Lavin_Radomes_Final.pdf.
- [9] X. Lei, L. Mao, Y. Lu, and P. Wang, "Revisiting the effective medium approximation in all-dielectric subwavelength multilayers: breakdown and rebuilding," *Physical Review B*, vol. 96, no. 3, article no. 035439, 2017.
- [10] M. Dorigo, "Optimization, learning and natural algorithms," Ph.D. dissertation, Politecnico di Milano, Italy, 1992.
- [11] D. E. Goldberg, *Genetic Algorithms in Search, Optimization, and Machine Learning*. Reading, MA: Addison-Wesley Publishing, 1989.

Trung Kien Nguyen



received his B.S. degree in information technology, University of Engineering and Technology from Vietnam National University, Hanoi, Vietnam, in 2013. He is currently working toward obtaining his M.S. degree in information and communication engineering from Kongju National University, Cheonan, Korea. His research interest is optimization algorithm in electromagnetics.

Obum Kwon



received his B.S. and M.S. degrees in mechanical engineering from Ulsan National Institute of Science and Technology, Ulsan, Korea, in 2015 and 2017, respectively. Since 2017, he has been a researcher for the Agency for Defense Development, Daejeon, Korea. His research interests include composite material structures and periodic electromagnetic structures.

In-Gon Lee



received his B.S. and M.S. degrees in information and communication engineering from Kongju National University, Cheonan, Korea, in 2013 and 2015, respectively. He is currently working toward obtaining his Ph.D. degree in information and communication engineering from the same university. His research interest is periodic electromagnetic structures.

Yoon-Jae Kim



received his M.S. and Ph.D. degrees in mechanical and aerospace engineering from Seoul National University, Seoul, Korea, in 2005 and 2011, respectively. From 2011 to 2012, he worked as a senior researcher at the Institute of Advanced Machines and Design, Seoul National University. Since 2012, he has been working at the Agency for Defense Development, Daejeon, Korea, as a senior researcher.

His research interests include aircraft structures and acoustic, vibration, and periodic electromagnetic structures.

Ic-Pyo Hong



received his B.S., M.S., and Ph.D. degrees in electronics engineering from Yonsei University, Seoul, Korea, in 1994, 1996, and 2000, respectively. From 2000 to 2003, he was a senior engineer in CDMA Mobile Research at the Information and Communication Division of Samsung Electronics Company, Suwon, Korea. In 2006 and 2012, he was a visiting scholar at Texas A&M University, College Station,

TX, USA, and Syracuse University, Syracuse, NY, USA, respectively. Since 2003, he has worked as a professor at the Department of Information and Communication Engineering, Kongju National University, Cheonan, Korea. His research interests include numerical techniques in electromagnetics, electromagnetic compatibility, and periodic electromagnetic structures.

Dual-Band Circularly Polarized Stack-Ring Antenna

Youngje Sung*

Abstract

A stack-ring configuration is proposed for designing a dual-band circularly polarized (CP) antenna. Each ring generates different resonant frequencies. A good CP performance at both resonant frequencies is achieved by adjusting the relative distance between the two rings. The two operating bands are separated with a small frequency ratio of 1.07. Measured results show that radiation patterns with good CP characteristics are obtained at the two resonant frequencies.

Key Words: CP Antenna, Dual-Band Antenna.

I. INTRODUCTION

The ring antenna is very attractive because a ring has a smaller size and larger bandwidth, compared to a microstrip patch antenna. Ring antennas are mainly designed for linear polarization [1]. However, since circularly polarized (CP) antennas can provide a stable signal quality between the transmitting and receiving devices, they are widely used in wireless communication systems [2]. Until now, much research in the open literature has focused on the design of the dual-band CP antenna [3–5]. Dual-band CP stacked patch antennas with truncated corners on both lower and upper patches were presented for global positioning system (GPS) applications in [3]. In [4], a CP dielectric resonator antenna loaded with a modified circular patch was proposed for dual-band applications. Both antennas in [3, 4] show the frequency ratio of 1.28. A single-feed dual-band CP antenna was achieved by using an asymmetrical U-shaped slot [5].

Many dual-band CP antennas have been studied [6–10]. Recently, the needs for wireless communication systems that require a small frequency ratio have emerged. The design of the dual-band CP antenna with a small frequency ratio is rather

challenging [6, 7], and is still being studied. In [6] and [7], the single-layer dual-band CP antennas with a small frequency ratio were implemented using the annular patches, cross slot, and asymmetric feed point. The frequency ratios are 1.10 and 1.21, respectively. In [8], the reported antenna achieved dual-band CP performance using an asymmetric S-slotted patch, where a frequency ratio of S_{11} (=1.28) was reported. In [9], the proposed antenna consists of an inner circular patch and an outer annular ring to generate dual-band operation. CP performance was achieved by the cross-slot, and a frequency ratio of 1.28 was reported. In [10], the dual-band CP antenna is composed of two elliptical-ring radiating patches and an asymmetric feed. The frequency ratio was 1.10.

In this article, we propose a new design for a single-feed dual-band CP antenna. This is achieved by designing two square rings that are stacked together. The asymmetry in the structure refers to the relative distance between the two rings. If the relative distance between the two rings is properly selected, the two orthogonal modes of the antenna would be excited with the same amplitude and a 90° phase difference at both the lower and upper bands. To confirm the characteristics of the dual-band CP antenna, the antenna designed at 2.5 and 2.67 GHz is

Manuscript received April 27, 2018 ; Revised August 20, 2018 ; Accepted October 26, 2018. (ID No. 20180427-035J)

Department of Electronic Engineering, Kyonggi University, Suwon, Korea.

*Corresponding Author: Youngje Sung (e-mail: yjsung@kgu.ac.kr)

This is an Open-Access article distributed under the terms of the Creative Commons Attribution Non-Commercial License (<http://creativecommons.org/licenses/by-nc/4.0>) which permits unrestricted non-commercial use, distribution, and reproduction in any medium, provided the original work is properly cited.

© Copyright The Korean Institute of Electromagnetic Engineering and Science. All Rights Reserved.

fabricated and measured.

II. ANTENNA GEOMETRY

Fig. 1 shows the proposed dual-band CP antenna on a double-layer. The dielectric constant $\epsilon_r = 2.2$ and thickness $h = 1.574$ mm of the two substrates are used for the proposed design. The size of substrate_2 is same with that of substrate_1. The ground plane size is $70 \text{ mm} \times 70 \text{ mm}$.

The proposed antenna consists of two square rings and a T-shaped feed line. The two (lower and upper) square rings have the outer side length of L_1 and L_2 and widths of w_1 and w_2 . A lower ring is located on the middle layer and an upper ring is located on the top layer. These rings serve as radiating elements. Here, the center position of the lower ring is established as a reference point. It is denoted by $C(0, 0)$. The center position of the upper square ring moves from $(0, 0)$ to 7 mm on the x -axis and 10 mm on the y -axis. It is denoted by $C'(7, 10)$. The width w_f of the feed line is chosen to be 4.2 mm, which corresponds to the characteristic impedance of 50Ω . Simulation is carried out using IE3D (Mentor Graphics, Wilsonville, OR, USA).

III. PARAMETER STUDY

Fig. 2(a) and (b) show the simulated results of the proposed

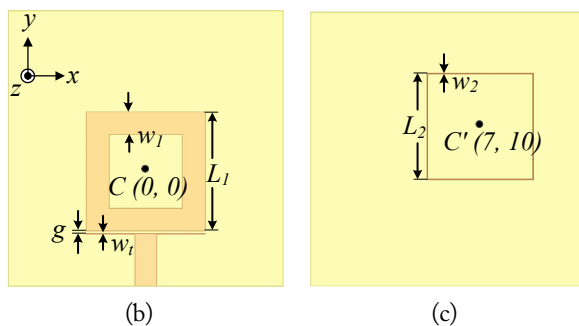
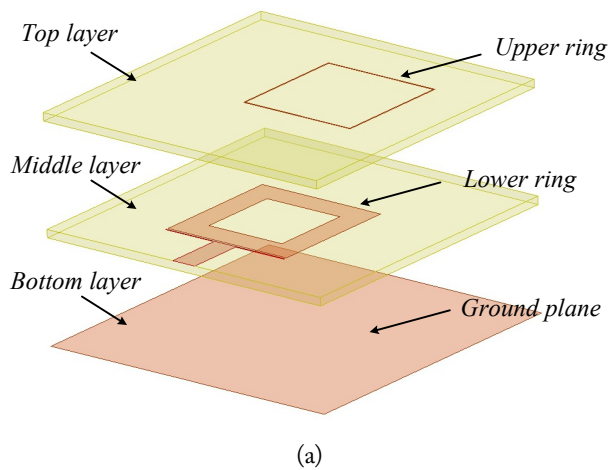


Fig. 1. Configuration of the proposed structure: (a) 3D view, (b) middle layer, and (c) top layer.

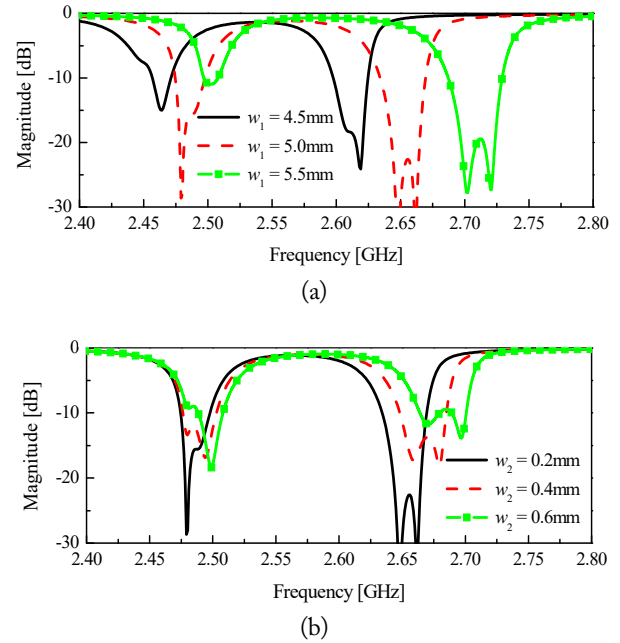


Fig. 2. Simulated results of the proposed antenna with different widths: (a) w_1 and (b) w_2 .

antenna for widths w_1 and w_2 , respectively. The side lengths (L_1 and L_2) of the two square rings are 26 mm and 23.4 mm, respectively. The other parameters are: $g = 0.2$ mm and $w_f = 0.2$ mm. It is well known that the resonant frequency of the ring resonator is mainly adjusted by changing the width of the ring. In this work, also, the lower ring works as a radiating element and works as a feed structure for the upper ring. Therefore, both resonant frequencies are increased as w_1 increases. The proposed antenna shows good impedance matching at the upper band when w_1 are all three values (4.5 mm, 5 mm, 5.5 mm) used above. It is observed that impedance matching has the optimum value as the width $w_1 = 5$ mm. On the other hand, it can be observed from Fig. 2(b) that an increase in w_2 increases the upper band. In this case, the lower band remains almost unchanged. Considering the impedance matching characteristic at both bands, the width w_2 is fixed to 0.2 mm.

Fig. 3 shows the simulated results of the proposed antenna with different positions of the upper ring. In this case, the lower ring is fixed. The other dimensions are the same as before. When the upper ring shifts leftward ($-x$ axis) or downward ($-y$ axis), there is a greater split between the two degenerated modes at the lower band. On the other hand, the two degenerated modes at the upper band are more split when the upper ring shifts in the opposite direction ($+x$ axis or $+y$ axis). In the cases of $C(6, 10)$ and $C(7, 9)$, there is a single resonance at the upper band. Therefore, the proposed antenna exhibits a linear polarization (LP) property at the upper band. In cases of $C(8, 10)$ and $C(7, 11)$, the proposed antenna shows a single resonance at the lower band. Therefore, the proposed antenna has LP operation

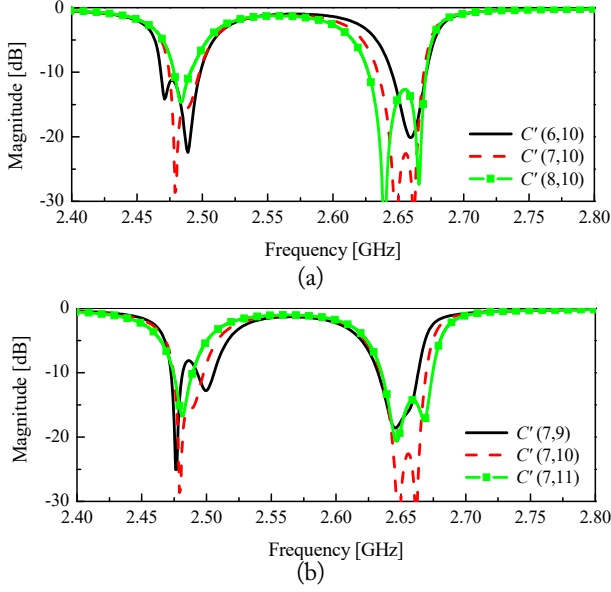


Fig. 3. Simulated results of the proposed antenna with different positions of the upper ring: (a) x direction shift and (b) y direction shift.

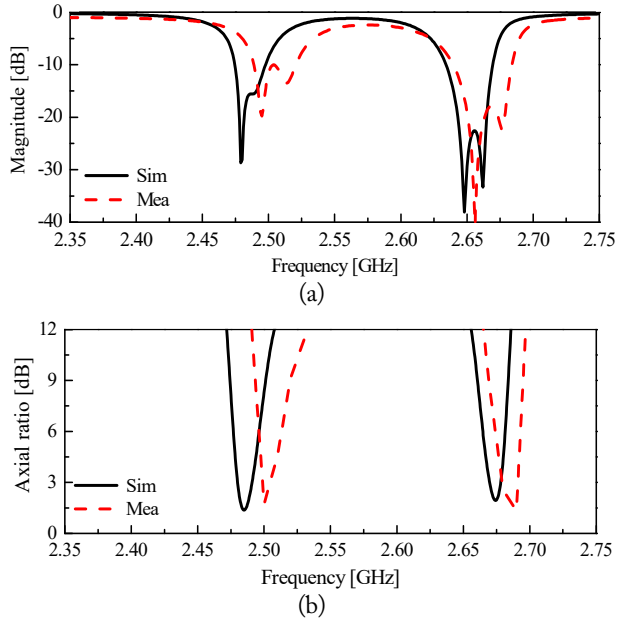


Fig. 4. Simulated and measured result: (a) reflection coefficient and (b) axial ratio.

at the lower band. With position C' chosen to be (7, 10), CP performance has the optimum value in this study.

IV. SIMULATED AND MEASURED RESULTS

The proposed antenna is designed and fabricated with optimal parameters and measured to confirm the simulation performance. Detailed geometrical parameters of the optimal antenna are as follows: $L_1 = 26$ mm, $L_2 = 23.4$ mm, $w_1 = 5$ mm, $w_2 = 0.2$ mm, $g = 0.2$ mm, $w_t = 0.2$ mm, and $C'(7, 10)$. Fig. 4

exhibits both the simulated and measured reflection coefficient and axial-ratio (AR) for the proposed antenna. The proposed antenna features 10-dB impedance bandwidths of 1.3% and 1.7 % and 3-dB AR bandwidths of 0.7% and 0.8% in the lower and upper bands, respectively. The reason for the difference between measurement and simulation is due to the tiny air gap between the two substrates or the alignment between ring resonators in different layers.

Figs. 5 and 6 show simulated current distributions at 2.482 GHz and 2.673 GHz, respectively. The blue and red areas indicate the minimum and maximum current distributions, respect-

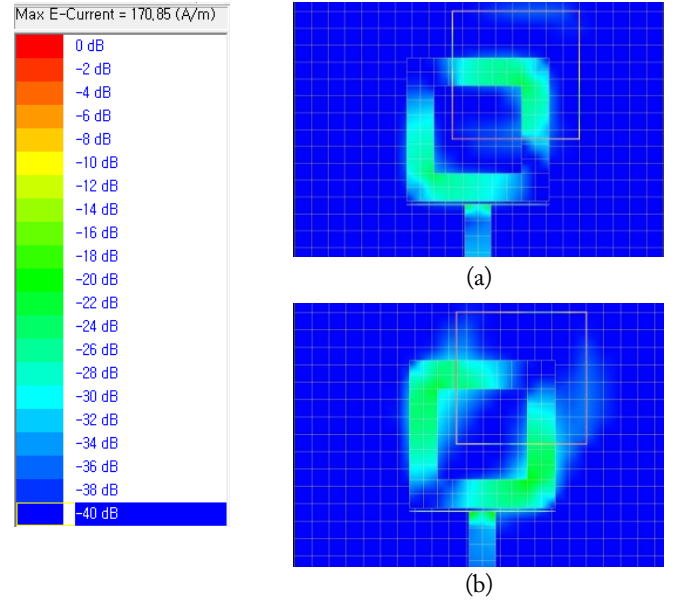


Fig. 5. Simulated current distribution at 2.482 GHz: (a) 0° and (b) 90° .

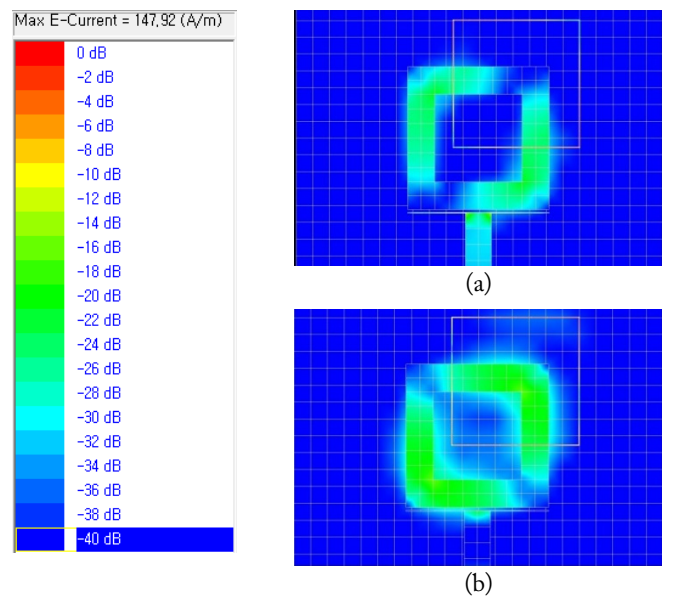


Fig. 6. Simulated current distribution at 2.673 GHz: (a) 0° and (b) 90° .

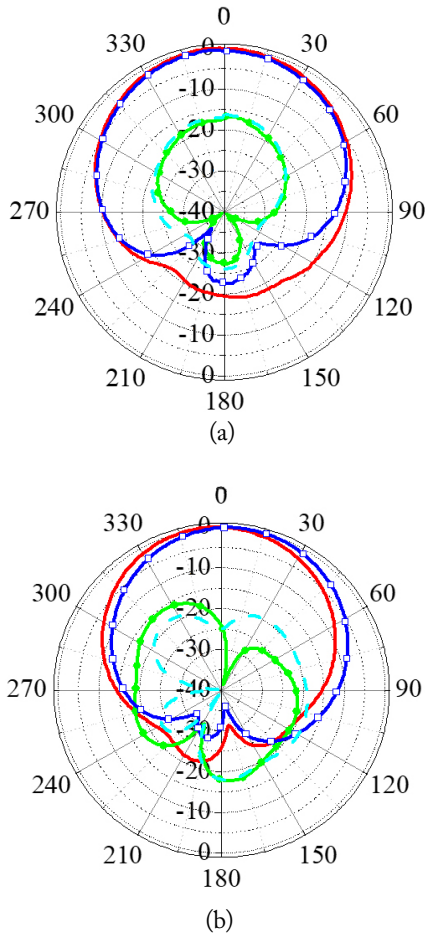


Fig. 7. Measured radiation pattern: (a) 2.5 GHz and (b) 2.67 GHz.

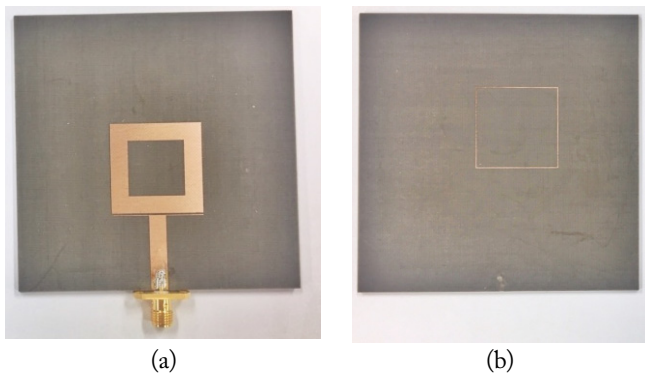


Fig. 8. Configuration of the proposed structure: (a) middle layer and (b) top layer.

tively. It can be seen from the current distribution that the proposed antenna operates as CP at two resonant frequencies.

The radiation patterns measured at 2.5 GHz and 2.67 GHz are shown in Fig. 7. It can be found that the proposed antenna radiates a left-hand circularly polarized (LHCP) wave with cross polarization better than 15 dB for the lower and upper bands. The measured peak gains are about 4.2 dBi for the lower band and 4.6 dBi for the upper band.

Fig. 8 shows the fabricated antenna.

V. CONCLUSION

The antenna structure consists of two square rings and a T-shaped feed line, and the proposed antenna exhibits CP operation because the relative distance between the two rings' centers is used as a perturbation. A prototype of the proposed design has been successfully implemented. If a wireless communication system requires a dual-band CP property with a unidirectional radiation pattern, the proposed antenna is an option that can be considered because it has a simple configuration and is easy to manufacture.

This work was supported by the National Research Foundation of Korea under Grant no. 2017R1A2B4010393 funded by the Korea government.

REFERENCES

- [1] Y. J. Sung, "Frequency and polarisation reconfigurability from an open-loop square ring antenna," *IET Microwaves, Antennas & Propagation*, vol. 6, no. 5, pp. 505–509, 2012.
- [2] H. M. Chen, Y. K. Wang, Y. F. Lin, C. Y. Lin, and S. C. Pan, "Microstrip-fed circularly polarized square-ring patch antenna for GPS applications," *IEEE Transactions on Antennas and Propagation*, vol. 57, no. 4, pp. 1264–1267, 2009.
- [3] S. Chen, G. Liu, X. Chen, T. Lin, X. Liu, and Z. Duan, "Compact dual-band GPS microstrip antenna using multi-layer LTCC substrate," *IEEE Antennas and Wireless Propagation Letters*, vol. 9, pp. 421–423, 2010.
- [4] Y. M. Pan, S. Y. Zheng, and W. Li, "Dual-band and dual-sense omnidirectional circularly polarized antenna," *IEEE Antennas and Wireless Propagation Letters*, vol. 13, pp. 706–709, 2014.
- [5] P. Nayeri, K. F. Lee, A. Z. Elsherbeni, and F. Yang, "Dual-band circularly polarized antennas using stacked patches with asymmetric U-slots," *IEEE Antennas and Wireless Propagation Letters*, vol. 10, pp. 492–495, 2011.
- [6] W. Liao and Q. X. Chu, "Dual-band circularly polarized microstrip antenna with small frequency ratio," *Progress In Electromagnetics Research*, vol. 15, pp. 145–152, 2010.
- [7] X. L. Bao and M. J. Ammann, "Dual-frequency circularly-polarized patch antenna with compact size and small frequency ratio," *IEEE Transactions on Antennas and Propagation*, vol. 55, no. 7, pp. 2104–2107, 2007.
- [8] Z. N. Chen and X. Qing, "Dual-band circularly polarized S-shaped slotted patch antenna with a small frequency-ratio," *IEEE Transactions on Antennas and Propagation*, vol. 58, no. 6, pp. 2112–2115, 2010.
- [9] N. Pham, J. Y. Chung, and B. Lee, "A proximity-fed antenna for dual-band GPS receiver," *Progress In Electromag-*

netics Research, vol. 61, pp. 1–8, 2016.

[10] Z. Wang, R. She, J. Han, S. Fang, and Y. Liu, "Dual-band dual-sense circularly polarized stacked patch antenna with

a small frequency ratio for UHF RFID reader applications," *IEEE Access*, vol. 5, pp. 15260–15270, 2017.

Youngje Sung



He received his B.S., M.S., and Ph.D. degrees from Korea University, Seoul, Korea, in 2001, 2002, and 2005, respectively. From 2005 to 2008, he was a senior engineer at the Antenna R&D Laboratory, Mobile Phone Division, Samsung Electronics, Korea. In 2008, he joined the Department of Electronic Engineering, Kyonggi University, Suwon, Korea, where he is currently a professor. His research inter-

ests include reconfigurable antennas, cellphone antennas, wideband slot antennas, multifunction devices, compact circular polarized antennas, and compact dual-mode filters. Prof. Sung serves as a reviewer for *IEEE Transactions on Microwave Theory and Techniques*, *IEEE Transactions on Antennas and Propagation*, *IEEE Microwave and Wireless Components Letters*, *IEEE Antennas and Wireless Propagation Letters*, *Progress in Electromagnetic Research*, *IET Electronics Letters*, and *IET Microwaves, Antennas, and Propagation*.

Modified Wilkinson Power Divider Using Transmission Lines for Various Terminated Impedances and an Arbitrary Power Ratio

Young-Chul Yoon¹ · Young Kim^{2,*}

Abstract

This paper introduces a modified Wilkinson power divider that uses uniform transmission lines for various terminated impedances and an arbitrary power ratio. For the designed power ratio, the proposed divider changes only the electrical lengths of the transmission lines between the input and output ports, and those between the output ports and the isolation resistor. In this case, even when various termination impedances of the ports exist, the divider characteristics are satisfied. To verify the feasibility of the proposed divider, two circuits were designed to operate at a frequency of 2 GHz with 2:1 and 4:1 power splitting ratios and various terminated impedances of 40, 70, and 60 Ω for one circuit, and 50, 70, and 60 Ω for the other. The measurement and simulation results were in good agreement.

Key Words: Arbitrary Power Ratio, Unequal Divider, Uniform Transmission Line, Various Terminated Impedance, Wilkinson Divider.

I. INTRODUCTION

The divider is the most widely used passive component in the wireless industry. In many cases, the same splitting divider is used [1, 2]. However, in special applications, cases that require unequal distribution [3, 4] or various termination impedances [5, 6] exist. To achieve a divider with unequal or various terminated impedances, a high-impedance transmission line must be implemented. Such a high-impedance transmission line is difficult to implement because of its very narrow line width that must be implemented through microstrip technology. Moreover, to satisfy the characteristics of the high-impedance line, a bulky capacitor or coupled lines with narrow gaps are used.

Recently, a new design method has been proposed to adjust only the electrical length of the transmission lines between the

input and output ports, or between the output ports and the isolation resistor, to achieve the operation of an unequal divider. Many dividers using a uniform transmission line have been introduced, such as a divider with uniform transmission lines of various electrical lengths [7–9], a structure using an isolated resistor with open-stub connection to obtain enhanced bandwidth [10], an isolated resistor configuration connected to the same impedance lines between the output ports with long stub length [11], a structure connected to various impedance lines at both sides of an isolation resistor [12], a Gysel divider with a phase shifter instead of a 180° transmission line [13], a ring hybrid coupler with a 50- Ω transmission line [14], and a half mode substrate integrated waveguide (HMSIW) divider with composite right and left-handed transmission line (CRLH-TL) [15]. This type of splitter uses a transmission line with uniform impedance, and

Manuscript received July 10, 2018 ; Revised October 3, 2018 ; Accepted October 30, 2018. (ID No. 20180710-053J)

¹Department of Electronics Engineering, Catholic Kwandong University, Gangneung, Korea.

²School of Electronics Engineering, Kumoh National Institute of Technology, Gumi, Korea.

*Corresponding Author: Young Kim (e-mail: youngk@kumoh.ac.kr)

This is an Open-Access article distributed under the terms of the Creative Commons Attribution Non-Commercial License (<http://creativecommons.org/licenses/by-nc/4.0>) which permits unrestricted non-commercial use, distribution, and reproduction in any medium, provided the original work is properly cited.

© Copyright The Korean Institute of Electromagnetic Engineering and Science. All Rights Reserved.

it does not use an impedance transformer to match each port, even though it operates as an unequal divider. Such a divider consists of circuits with an arbitrary power split ratio and a termination impedance of 50Ω .

In this paper, we propose a modified Wilkinson divider using a uniform transmission line with various termination impedances and an arbitrary dividing ratio as well as the previously used 50Ω termination impedance. This type of device eliminates the requirement for a matching circuit between the divider and the peripheral device with various termination impedances, and allows a small circuit size to be achieved.

II. THEORY AND DESIGN

Fig. 1 shows the schematic of the proposed power divider with power splitting ratio $k^2 (= P_2/P_3)$. This proposed divider consists of three transmission lines with uniform impedance Z_{uL} and various electrical lengths of θ_{1L} , θ_{2L} , and θ_{3L} , an isolation resistor R_{iso} , and various terminated impedances of R_{aT} , R_{bT} , and R_{cT} .

In addition, this divider must satisfy the S -parameter characteristics of the unequal Wilkinson power divider:

$$(S)_{unequal} = \frac{1}{\sqrt{1+k^2}} \begin{pmatrix} 0 & k \cdot e^{-j\beta} & e^{-j\beta} \\ k \cdot e^{-j\beta} & 0 & 0 \\ e^{-j\beta} & 0 & 0 \end{pmatrix} \quad (1)$$

where β is the phase shift of the transmission coefficient.

Because the proposed power divider with various terminated impedances is asymmetrical, we analyzed it using scattering parameters rather than the conventional even-odd method. When port 1 is excited, all power is transmitted to the output ports, P_2 and P_3 , and the voltage from the branch of $P_1 - P_2$ to ground is the same as that from the branch of $P_1 - P_3$ to ground at any distance from P_1 , and no current flows in the isolation resistor. Because the isolation resistor operates as an open circuit, we can design an equivalent circuit between ports 2 and 3, as shown in Fig. 2(a). The ABCD parameters between port 1 and ports 2 and 3 can be expressed as

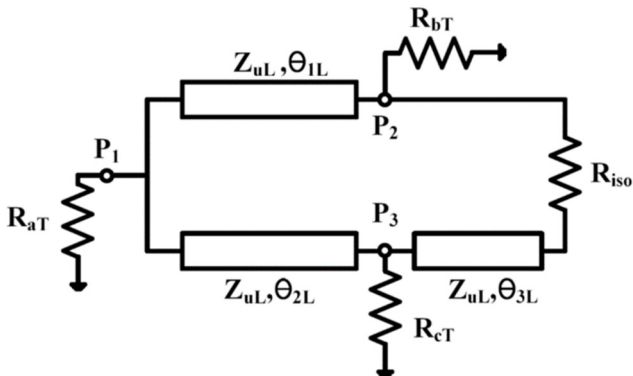


Fig. 1. Schematic of the proposed Wilkinson power divider.

$$\begin{pmatrix} A_{21} & B_{21} \\ C_{21} & D_{21} \end{pmatrix} = \begin{pmatrix} \cos \theta_{1L} & jZ_{uL} \cdot \sin \theta_{1L} \\ \frac{j \sin \theta_{1L}}{Z_{uL}} & \cos \theta_{1L} \end{pmatrix} \quad (2)$$

$$\begin{pmatrix} A_{31} & B_{31} \\ C_{31} & D_{31} \end{pmatrix} = \begin{pmatrix} \cos \theta_{2L} & jZ_{uL} \cdot \sin \theta_{2L} \\ \frac{j \sin \theta_{2L}}{Z_{uL}} & \cos \theta_{2L} \end{pmatrix} \begin{pmatrix} 1 & 0 \\ \frac{j \tan \theta_{3L}}{Z_{uL}} & 1 \end{pmatrix} \quad (3)$$

The ABCD parameters of Eqs. (2) and (3) can be converted into the S -parameters of S_{21} and S_{31} . Using the relation of $S_{21} = k \cdot S_{31}$, the following related equations are then obtained.

$$k^2 \sqrt{\frac{R_{cT}}{R_{bT}}} \cdot \left(R_{bT} + \frac{1+k^2}{k^2} R_{aT} \right) \cos \theta_{1L} \\ = \left\{ R_{cT} + (1+k^2) R_{aT} \right\} \cos \theta_{2L} - R_{cT} \sin \theta_{2L} \tan \theta_{3L} \quad (4)$$

$$k^2 \sqrt{\frac{R_{cT}}{R_{bT}}} \cdot \left(Z_{uL}^2 + \frac{1+k^2}{k^2} R_{aT} R_{bT} \right) \sin \theta_{1L} \\ = \left\{ Z_{uL}^2 + (1+k^2) R_{aT} R_{cT} \right\} \sin \theta_{2L} + (1+k^2) R_{aT} R_{cT} \cos \theta_{2L} \tan \theta_{3L} \quad (5)$$

In Fig. 2(a), under the input matching condition ($S_{11} = 0$), we have

$$\frac{1}{Z_{2e}} + \frac{1}{Z_{3e}} = \frac{1}{R_{aT}} \quad (6)$$

$$Z_{2e} = Z_{uL} \frac{R_{bT} + jZ_{uL} \tan \theta_{1L}}{Z_{uL} + jR_{bT} \tan \theta_{1L}} \quad (7)$$

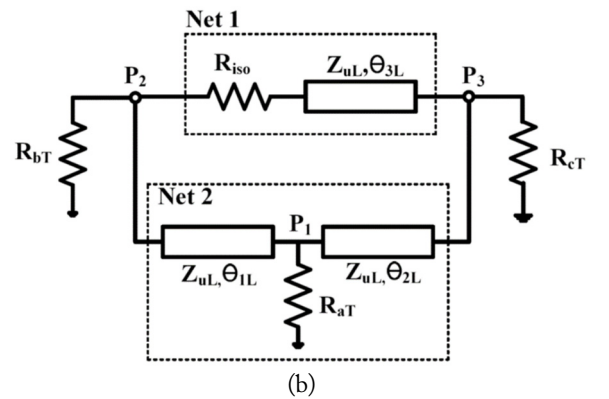
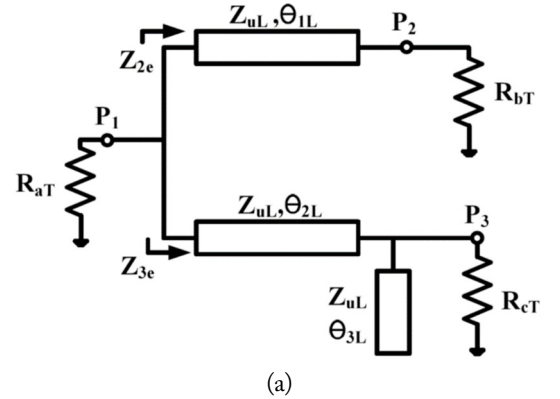


Fig. 2. (a) Equivalent circuit of proposed divider when port 1 is excited and (b) equivalent circuit of the proposed divider when port 2 is excited.

$$Z_{3e} = Z_{uL} \frac{R_{eT}(1 - \tan \theta_{2L} \tan \theta_{3L}) + jZ_{uL} \tan \theta_{2L}}{Z_{uL} + jR_{eT}(\tan \theta_{2L} + \tan \theta_{3L})} \quad (8)$$

where Z_{2e} and Z_{3e} are the input impedances of the upper and lower branches, respectively.

Based on the principle of conservation of energy and ideal transmission lines, the real parts of Z_{2e} and Z_{3e} are expressed as follows:

$$\text{Re}[Z_{2e}] = \frac{1+k^2}{k^2} R_{aT} \quad (9)$$

$$\text{Re}[Z_{3e}] = (1+k^2) R_{aT} \quad (10)$$

In Fig. 2(b), when port 2 is excited, the networks of Net1 and Net2 are connected in parallel, in which Net1 consists of the isolation resistor R_{iso} and the transmission line of electrical length θ_{3L} ; and Net2 consists of a termination resistor R_{aT} and transmission lines of electrical lengths θ_{1L} , θ_{2L} . The ABCD parameters of Net1 and Net2 can be expressed as:

$$\begin{pmatrix} A_{Net1} & B_{Net1} \\ C_{Net1} & D_{Net1} \end{pmatrix} = \begin{pmatrix} 1 & R_{iso} \\ 0 & 1 \end{pmatrix} \begin{pmatrix} \cos \theta_{3L} & jZ_{uL} \sin \theta_{3L} \\ \frac{j \sin \theta_{3L}}{Z_{uL}} & \cos \theta_{3L} \end{pmatrix} \quad (11)$$

$$\begin{pmatrix} A_{Net2} & B_{Net2} \\ C_{Net2} & D_{Net2} \end{pmatrix} = \begin{pmatrix} \cos \theta_{1L} & jZ_{uL} \sin \theta_{1L} \\ \frac{j \sin \theta_{1L}}{Z_{uL}} & \cos \theta_{1L} \end{pmatrix} \begin{pmatrix} 1 & 0 \\ \frac{1}{R_{aT}} & 1 \end{pmatrix} \begin{pmatrix} \cos \theta_{2L} & jZ_{uL} \sin \theta_{2L} \\ \frac{j \sin \theta_{2L}}{Z_{uL}} & \cos \theta_{2L} \end{pmatrix} \quad (12)$$

The ABCD parameters of Eqs. (11) and (12) are converted into the Y-parameters of Net1 and Net2, respectively, and the admittance parameters of the entire network can be obtained as follows:

$$\begin{pmatrix} Y_{11_tot} & Y_{12_tot} \\ Y_{21_tot} & Y_{22_tot} \end{pmatrix} = \begin{pmatrix} Y_{11_Net1} & Y_{12_Net1} \\ Y_{21_Net1} & Y_{22_Net1} \end{pmatrix} + \begin{pmatrix} Y_{11_Net2} & Y_{12_Net2} \\ Y_{21_Net2} & Y_{22_Net2} \end{pmatrix} \quad (13)$$

where

$$Y_{11_tot} = \frac{\cos \theta_{3L}}{R_{iso} \cos \theta_{3L} + jZ_{uL} \sin \theta_{3L}} + \frac{\cos \theta_{1L} \cos \theta_{2L} - \sin \theta_{1L} \sin \theta_{2L} + j \frac{Z_{uL}}{R_{aT}} \sin \theta_{2L} \cos \theta_{1L}}{\frac{Z_{uL}^2}{R_{aT}} \sin \theta_{1L} \sin \theta_{2L} + jZ_{uL} (\sin \theta_{2L} \cos \theta_{1L} + \sin \theta_{1L} \cos \theta_{2L})}$$

$$Y_{12_tot} = Y_{21_tot} = \frac{-1}{R_{iso} \cos \theta_{3L} + jZ_{uL} \sin \theta_{3L}} + \frac{-1}{\frac{Z_{uL}^2}{R_{aT}} \sin \theta_{1L} \sin \theta_{2L} + jZ_{uL} (\sin \theta_{2L} \cos \theta_{1L} + \sin \theta_{1L} \cos \theta_{2L})}$$

$$Y_{22_tot} = \frac{\cos \theta_{3L} + j \frac{R_{iso}}{Z_{uL}} \sin \theta_{3L}}{R_{iso} \cos \theta_{3L} + jZ_{uL} \sin \theta_{3L}} + \frac{\cos \theta_{1L} \cos \theta_{2L} - \sin \theta_{1L} \sin \theta_{2L} + j \frac{Z_{uL}}{R_{aT}} \sin \theta_{2L} \cos \theta_{1L}}{\frac{Z_{uL}^2}{R_{aT}} \sin \theta_{1L} \sin \theta_{2L} + jZ_{uL} (\sin \theta_{2L} \cos \theta_{1L} + \sin \theta_{1L} \cos \theta_{2L})}$$

The admittance parameters of Eq. (13) can be converted to the S-parameters of S_{22} , S_{32} , and S_{33} with terminated impedances of R_{bT} and R_{cT} . The S-parameters of the entire network between ports 2 and 3 can be expressed as

$$S_{22} = -\frac{(Y_{11_tot} - \frac{1}{R_{bT}})(Y_{22_tot} + \frac{1}{R_{cT}}) - Y_{12_tot} Y_{21_tot}}{(Y_{11_tot} + \frac{1}{R_{bT}})(Y_{22_tot} + \frac{1}{R_{cT}}) - Y_{12_tot} Y_{21_tot}} \quad (14)$$

$$S_{32} = -\frac{2\sqrt{\frac{1}{R_{bT}R_{cT}}Y_{21_tot}}}{(Y_{11_tot} + \frac{1}{R_{bT}})(Y_{22_tot} + \frac{1}{R_{cT}}) - Y_{12_tot} Y_{21_tot}} \quad (15)$$

$$S_{33} = -\frac{(Y_{11_tot} + \frac{1}{R_{bT}})(Y_{22_tot} - \frac{1}{R_{cT}}) - Y_{12_tot} Y_{21_tot}}{(Y_{11_tot} + \frac{1}{R_{bT}})(Y_{22_tot} + \frac{1}{R_{cT}}) - Y_{12_tot} Y_{21_tot}} \quad (16)$$

Based on Eqs. (4) to (5), (9) to (10), and (14) to (16), the electrical lengths θ_{1L} , θ_{2L} , θ_{3L} , and isolation resistance R_{iso} that satisfy the power divider characteristic conditions with $|S_{22}| < -20$ dB, $|S_{33}| < -20$ dB, and $|S_{32}| < -20$ dB at center frequency can be obtained by using MATLAB.

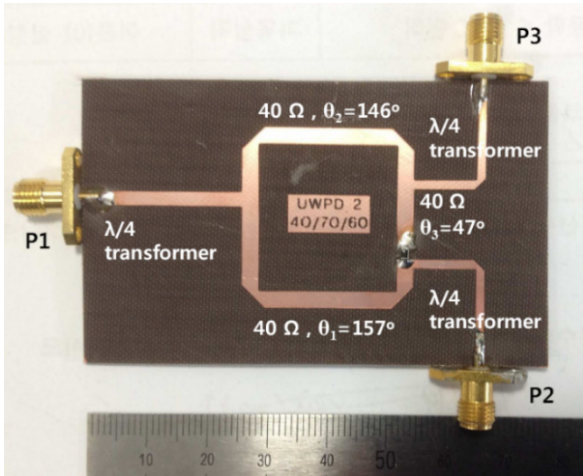
III. SIMULATION AND EXPERIMENTAL RESULTS

To validate the proposed power divider, we designed two types of circuits at a center frequency of 2 GHz. One has a power dividing ratio of $k^2 = 2$ and port impedances of $R_{aT} = 40 \Omega$, $R_{bT} = 70 \Omega$, and $R_{cT} = 60 \Omega$. The second circuit has a power dividing ratio of $k^2 = 4$ and port impedances of $R_{aT} = 50 \Omega$, $R_{bT} = 70 \Omega$, and $R_{cT} = 60 \Omega$. For the first circuit, when the transmission line characteristic impedance of $Z_{uL} = 40 \Omega$ was chosen, we calculated the electrical lengths and isolation resistance using the equations above and after optimization as follows: $\theta_{1L} = 157^\circ$, $\theta_{2L} = 146^\circ$, $\theta_{3L} = 47^\circ$, and $R_{iso} = 12 \Omega$. For the second circuit, when a transmission line characteristic impedance of $Z_{uL} = 40 \Omega$ was chosen, we calculated the electrical lengths and isolation resistance using the equations above and after optimization as follows: $\theta_{1L} = 153^\circ$, $\theta_{2L} = 130^\circ$, $\theta_{3L} = 66^\circ$, and $R_{iso} = 20 \Omega$. The Teflon substrate of the proposed power divider had a dielectric constant of 2.5, a thickness of 0.787 mm, and a conductor thickness of 0.035 mm.

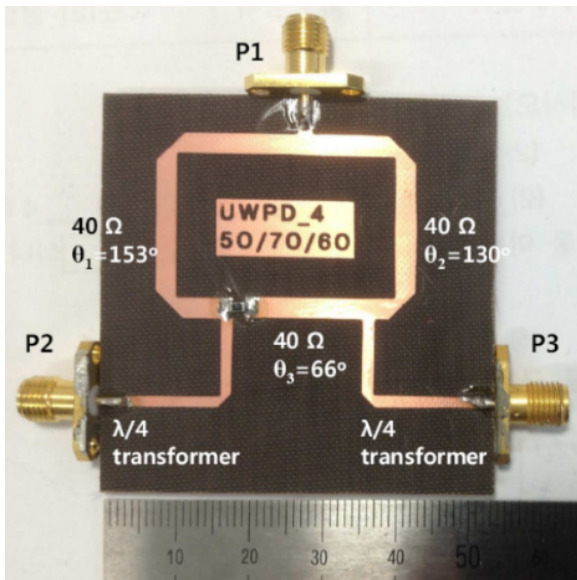
The simulation was performed using Microwave Office software with version 13 developed by National Instruments.

Fig. 3(a) and (b) show the photographs of the circuits in which $k^2 = 2$ and $k^2 = 4$, respectively, where power dividers of various port impedances and uniform transmission lines are implemented. For the measurement, the impedance transformers shown in Fig. 3 were used to match the input and output ports to 50 Ω .

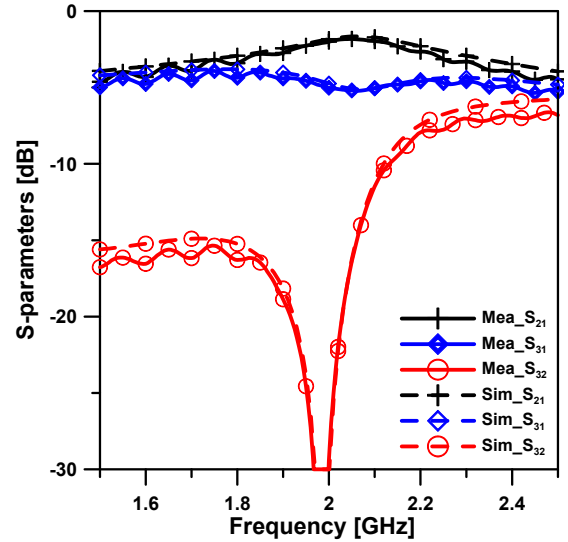
Fig. 4(a) and (b) show the measured and simulated S-parameters of the circuit with a power dividing ratio of $k^2 = 2$ and port impedances of 40, 70, and 60 Ω ; the figures show insertion losses of $|S_{21}| = 2.0$ dB and $|S_{31}| = 5.0$ dB, an isolation of $|S_{32}| > 25$ dB, an input return loss of $|S_{11}|$ that is better than -20 dB, and output return losses of $|S_{22}|$, $|S_{33}|$ that are better than -18 dB at the center frequency of 2 GHz. In addition, Fig. 5(a) and (b) show the measured and simulated S-parameters of the circuit with a power dividing ratio of $k^2 = 4$ and port impedances of 50, 70, and 60 Ω ; the figures show insertion losses of $|S_{21}| = 1.2$ dB and $|S_{31}| = 6.8$ dB, an isolation of $|S_{32}| > 25$ dB, an input return loss of $|S_{11}|$ that is better than -25 dB, and out-



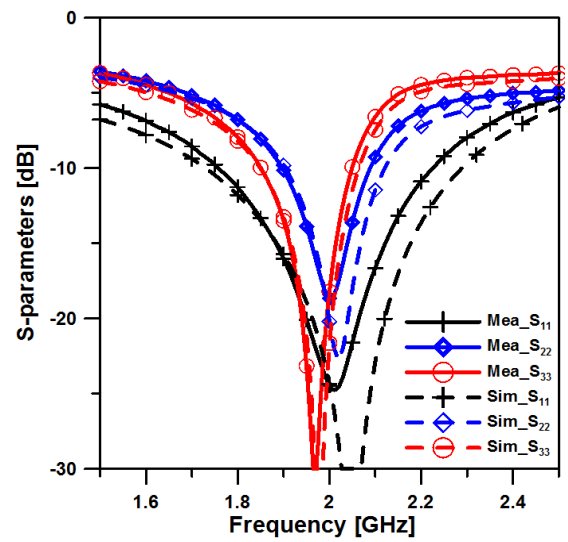
(a)



(b)



(a)



(b)

Fig. 3. Photographs of the implemented power divider: (a) $k^2 = 2$ and (b) $k^2 = 4$.

Fig. 4. Measured and simulated S -parameters of the $k^2 = 2$ circuit: (a) $|S_{21}|$, $|S_{31}|$, $|S_{32}|$ and (b) $|S_{11}|$, $|S_{22}|$, $|S_{33}|$.

put return losses of $|S_{22}|$, $|S_{33}|$ that are better than -25 dB, -13 dB, respectively, at the center frequency of 2 GHz. In Figs. 4

and 5, the $|S_{33}|$ data can be observed with slight frequency deviation, which is caused by the parallel admittance of electrical

Table 1. Comparison of the proposed divider with conventional power dividers

Ref.	Dividing ratio and type	Frequency (GHz)	Total length ^a (°)	TL impedance (Ω)	Term. (Ω)	IL (dB)	RL (dB)	Isolation (dB)
[7]	2:1 / 4:1 (WPD)	1	270 / 300	70.7	50	0.3	30	30
[10]	4:1 (WPD)	3	388	50	50	0.9	15	20
[11]	1:1 (WPD)	60/90	321.04	50	50	0.3	22	19
[12]	2:1 / 4:1 / 9:1 (WPD)	3	324.82 / 332.21 / 341.66	50	50	-	20	20
[13]	9:1 (Gysel)	1	219	70.7	50	0.2	20	29
[14]	9:1 (Ring)	1	378.6	50	50	0.4	25	40
This work	2:1 / 4:1 (WPD)	2	350 / 349	40	40/50 / 60/70	0.3	18	25

WPD = Wilkinson power divider, IL = insertion loss, RL = return loss.

^aWithout output matching transformer.

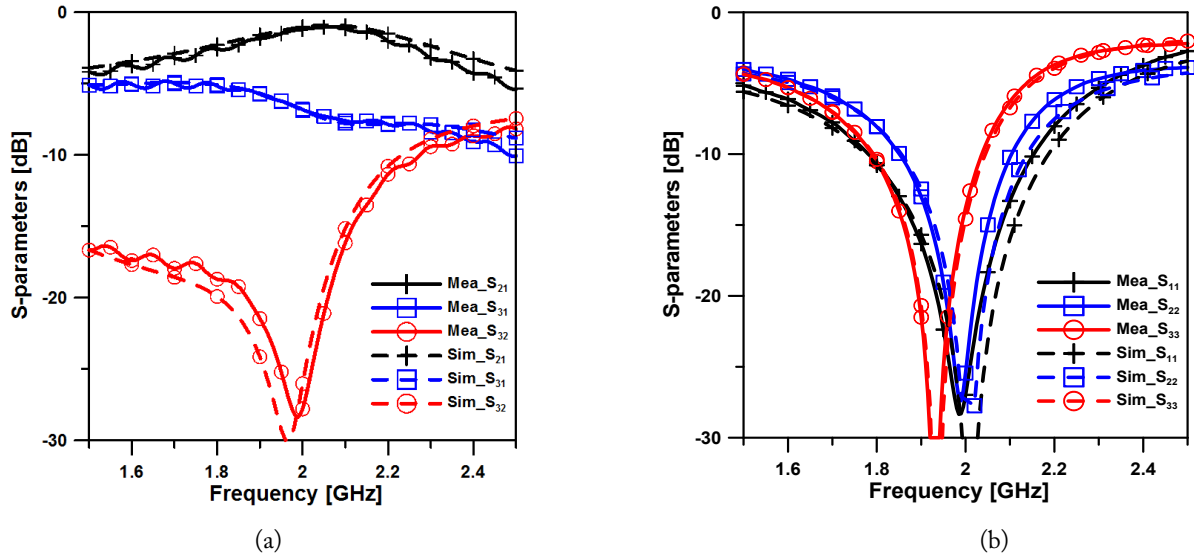


Fig. 5. Measured and simulated S -parameters of the $k^2 = 4$ circuit: (a) $|S_{21}|$, $|S_{31}|$, $|S_{32}|$ and (b) $|S_{11}|$, $|S_{22}|$, $|S_{33}|$.

Table 2. Summary of experimental results and design parameters of the proposed power divider

Dividing ratio	Term. (Ω)	$ S_{21} $ (dB)	$ S_{31} $ (dB)	$ S_{11} $ (dB)	$ S_{22} $ (dB)	$ S_{33} $ (dB)	$ S_{32} $ (dB)	θ_1 ($^\circ$)	θ_2 ($^\circ$)	θ_3 ($^\circ$)	R_{iso} (Ω)
2	40/70/60	2.0	5.0	-20	-18	-18	-25	157	146	47	12
4	50/70/60	1.2	6.8	-25	-25	-13	-25	153	130	66	20

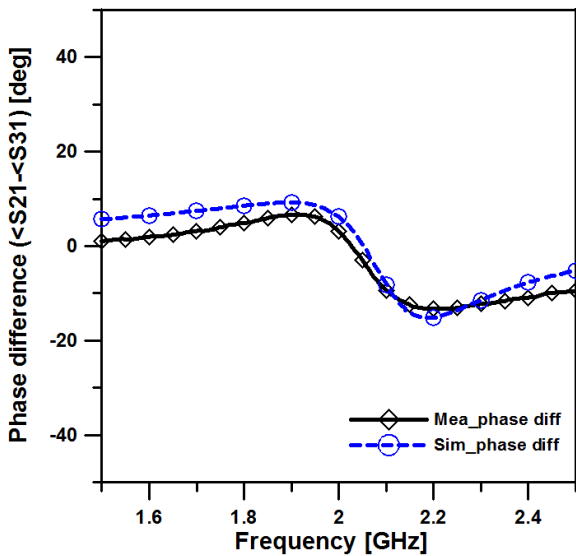


Fig. 6. Measured and simulated phase difference between the output ports of the $k^2 = 2$ circuit.

length θ_{3L} . Fig. 6 shows that the phase difference between the output ports of the $k^2 = 2$ circuit is $+3^\circ$ at the center frequency of 2 GHz. Table 1 shows a comparison of dividers using the conventional uniform transmission line and the results obtained for the proposed divider. In addition, Table 2 summarizes the experimental results and design parameters of the proposed power divider.

IV. CONCLUSION

This paper presented a modified Wilkinson divider using uniform transmission lines for various terminated impedances and an arbitrary dividing ratio. With this configuration, the desired splitting ratio can be obtained by adjusting only the electrical length of the transmission lines between the ports. Moreover, it has the advantage that the impedance of the ports is set to various terminated impedances, and is connected to a circuit without a matching circuit. The feasibility of the proposed power divider design concept was demonstrated, and the simulated and measured results were confirmed to be in good agreement.

REFERENCES

- [1] E. J. Wilkinson, "An N-way hybrid power divider," *IRE Transaction on Microwave Theory and Techniques*, vol. 8, no. 1, pp. 116–118, 1960.
- [2] U. H. Gysel, "A new N-way power divider/combiner suitable for high-power application," in *Proceedings of IEEE MTT-S International Microwave Symposium*, Palo Alto, CA, 1975, pp. 116–118.
- [3] Y. Kim and Y. C. Yoon, "A modified unequal power divider with a complex isolation component for enhanced isolation," *Microwave and Optical Technology Letters*, vol. 57, no. 2, pp. 322–324, 2015.

- [4] A. K. Agrawal and G. F. Mikucki, "A printed circuit hybrid ring directional coupler for arbitrary power divisions," *IEEE Transactions on Microwave Theory and Techniques*, vol. 34, no. 12, pp. 1401–1407, 1986.
- [5] H. R. Ahn, I. Wolff, and I. S. Chang, "Arbitrary termination impedances, arbitrary power division and small-sized ring hybrids," *IEEE Transactions on Microwave Theory and Techniques*, vol. 44, no. 12, pp. 2241–2247, 1997.
- [6] H. R. Ahn and I. Wolff, "Three-port 3-dB power divider terminated by different impedances and its application to MMICs," *IEEE Transactions on Microwave Theory and Techniques*, vol. 47, no. 6, pp. 786–794, 1999.
- [7] K. K. M. Cheng and P. W. Li, "A novel power-divider design with unequal power-dividing ratio and simple layout," *IEEE Transactions on Microwave Theory and Techniques*, vol. 57, no. 6, pp. 1589–1594, 2009.
- [8] P. W. Li and K. K. M. Cheng, "A new unequal power-divider design with enhanced insertion loss flatness," *IEEE Microwave and Wireless Components Letters*, vol. 19, no. 12, pp. 786–788, 2009.
- [9] Z. Haiwei and X. Quan, "A novel Gysel power divider with arbitrary power ratio for high-power application," in *Proceedings of IEEE International Wireless Symposium (IWS)*, Beijing, China, 2013, pp. 1–4.
- [10] Y. Z. Zhu, X. F. Zhang, X. F. Wu, C. Li, and G. Y. Fang, "Novel Wilkinson power divider with uniform impedance line," in *Proceedings of Asia-Pacific Microwave Conference (APMC)*, Macau, China, 2008, pp. 1–4.
- [11] S. Horst, R. Bairavasubramanian, M. M. Tentzeris, and J. Papapolymerou, "Modified Wilkinson power dividers for millimeter-wave integrated circuits," *IEEE Transactions on Microwave Theory and Techniques*, vol. 55, no. 11, pp. 2439–2446, 2007.
- [12] T. Qi, S. He, Z. Dai, and W. Shi, "Novel unequal power divider with 50 Ω characteristic impedance lines," *IEEE Microwave and Wireless Components Letters*, vol. 26, no. 3, pp. 180–182, 2016.
- [13] F. Lin, Q. X. Chu, and S. W. Wong, "A novel Gysel power divider design with uniform impedance transmission lines for arbitrary power-dividing ratios," *Journal of Electromagnetic Waves and Applications*, vol. 27, no. 2, pp. 242–249, 2013.
- [14] M. J. Park and B. Lee, "Design of ring couplers for arbitrary power division with 50 Ω lines," *IEEE Microwave and Wireless Components Letters*, vol. 21, no. 4, pp. 185–187, 2011.
- [15] D. S. Eom and H. Y. Lee, "A broadband half-mode substrate integrated waveguide quadrature Wilkinson power divider using composite right/left-handed transmission line," *Journal of Electromagnetic Engineering and Science*, vol. 17, no. 1, pp. 9–13, 2017.

Young-Chul Yoon



received his B.S., M.S., and Ph.D. in electronics engineering from Sogang University, Seoul, Korea, in 1978, 1982, and 1989, respectively. In 1987, he joined the Department of Electronics Engineering, Catholic Kwandong University, Gangneung, Korea, where he is currently a Professor. His areas of interest are the design of high power amplifiers for the ISM band, and RF and microwave circuit analysis and design.

Young Kim



received his B.S., M.S., and Ph.D. in electronics engineering from Sogang University, Seoul, Korea, in 1986, 1988, and 2002, respectively. He developed cellular and PCS linear power amplifiers at Samsung Electronics Co., Ltd. In 2003, he joined the School of Electronics Engineering, Kumoh National Institute of Technology, Gumi, Korea, where he is currently a Professor. His areas of interest are the design of high-power amplifiers and linearization techniques, and RF and microwave circuit analysis and design.

Toroidal-Shaped Coils for a Wireless Power Transfer System for an Unmanned Aerial Vehicle

Jaehyoung Park¹ · Jonghoon Kim² · Yujun Shin¹ · Bumjin Park¹ · Won-Seok Kim³ ·
Seok-Jong Cheong³ · Seungyoung Ahn^{1,*}

Abstract

Unmanned aerial vehicles (UAVs) using communications, sensors, and navigation equipment will play a key role in future warfare. Currently, UAVs are monitored to prevent misfire and accidents, and the conventional method adopted uses wires for data transmission and power supply. The repeated connection and disconnection of cables increases maintenance time and harms the connector. For convenience and stability, a wireless power transfer system to power UAVs is needed. Unlike other wireless power transfer (WPT) applications, the size of the receiving coils must be small, so that the WPT systems can be embedded inside space-limited UAVs. The small size reduces the coupling coefficient and transfer efficiency between the transmitting and the receiving coils. In this study, we propose a toroidal-shaped coil for a WPT system for UAVs with high coupling coefficient with minimum space requirements. For validation, conventional coils and the proposed toroidal-shaped coil were used and their coupling coefficient and power transfer efficiency were compared using simulated and measured results. The simulated and measured results were strongly correlated, confirming that the proposed WPT system significantly improved efficiency with negligible change in the space requirement.

Key Words: Coupling Coefficient, Power Transfer Efficiency, Unmanned Aerial Vehicles, Wireless Charging, Wireless Power Transfer.

I. INTRODUCTION

Modern and future warfare is shifting toward a space environment with manned and unmanned weapons. The need for unmanned aerial vehicles (UAVs) is increasing. The modern military weapons system is based on the use of communication, sensors, and navigation equipment to accomplish a given task, even in hard-to-reach areas [1]. UAVs include all types of equipment, including drones, satellites, and missiles, among others. However, as UAVs become more advanced, their maintenance and repair also require a higher level of scientific

technology. Conventional UAVs depend on fuel cells with high-energy density for operations. The fuel cell will not stop burning once it has been ignited [2]. UAVs with fuel cells have a 10-year life span. They can avoid misfire and accidents by conducting periodic safety maintenance of the charging and power supply systems. The current UAV power supply maintenance method is shown in Fig. 1 [3]. However, this maintenance method has three problems. First, a large number of direct cables must be connected and then disassembled each time to supply the power. This condition increases the possibility that maintenance time is expanded or that maintenance efficiency is

Manuscript received May 2, 2018 ; Revised July 23, 2018 ; Accepted October 30, 2018. (ID No. 20180502-039J)

¹The Cho Chun Shik Graduate School of Green Transportation, Korea Advanced Institute of Science and Technology (KAIST), Daejeon, Korea.

²EMC Doctors Inc., Hwaseong, Korea.

³WISTEK Co. Ltd., Gunpo, Korea.

*Corresponding Author: Seungyoung Ahn (e-mail: sahn@kaist.ac.kr)

This is an Open-Access article distributed under the terms of the Creative Commons Attribution Non-Commercial License (<http://creativecommons.org/licenses/by-nc/4.0>) which permits unrestricted non-commercial use, distribution, and reproduction in any medium, provided the original work is properly cited.

© Copyright The Korean Institute of Electromagnetic Engineering and Science. All Rights Reserved.

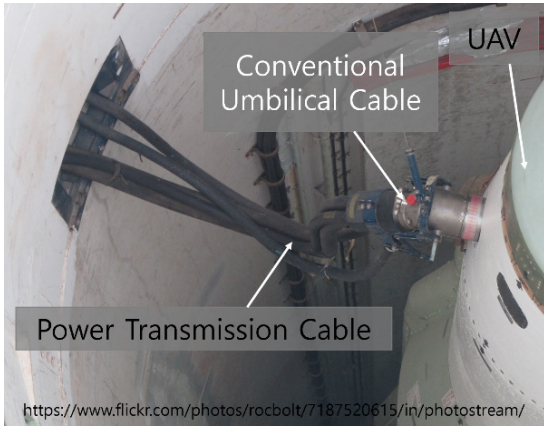


Fig. 1. Conventional method for charging and repairing an unmanned vehicle [3].

low. Second, the repeated connection and disconnection of cables causes wear and tear to the connector. It also has the potential to diminish the performance of UAVs. Third, when the UAVs are deployed, the launcher is destroyed every time because the power supply cables and modules are still connected when the UAVs are launched. The demand for wireless power transfer (WPT) technology is increasing because of these and other umbilical cable shortcomings. Therefore, WPT technologies have recently been developed to overcome the limitations of the wired power transfer system [4, 5].

Although WPT technology can overcome the shortcomings of a wired power system, there is concern that the transmission distance poses a potential inconvenience to users [6]. Various coil systems and methods have been employed to increase the transmission distance [7, 8]. However, these enhancing methods generally require increased space, weight, and cost, which are critical problems in UAVs.

In this study, we propose a toroidal-shaped coil for the WPT systems of UAVs. The toroidal-shaped coil includes a wing-shaped ferrite located at the ends of the coil. The toroidal-shaped coil increases the transmission distance by increasing the coupling coefficient between the source and the load coils. It can be applied in UAVs because it requires minimal space, which is an important feature in UAVs.

II. WPT COIL SYSTEMS AS THE CORDLESS UMBILICAL CONNECTOR OF A UAV

To transfer several hundred Watts or more of power with high efficiency in a WPT environment within a few centimeters, a magnetic induction-type WPT technology should be used. The magnetic induction-type WPT system in a UAV typically includes an inverter, a resonance matching capacitor, two magnetically coupled coils, and an AC-DC convertor, as shown in Fig. 2.

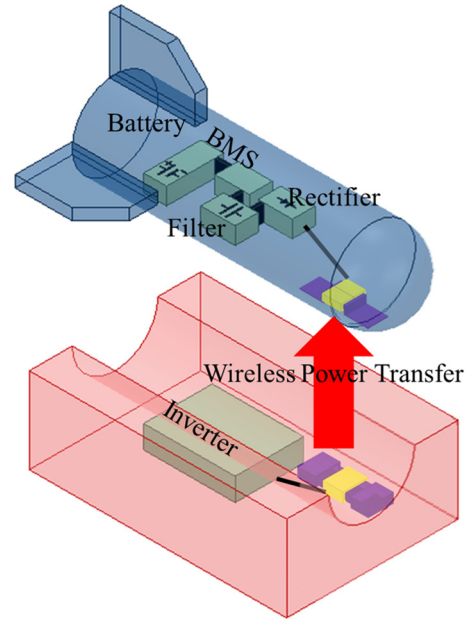


Fig. 2. Concept of the wireless power transfer system for unmanned vehicles.

In the WPT system used in this study for a UAV, the air gap from the launch ramp to the UAV is 50 mm, as shown in Fig. 3. The body and the WPT coil case is made of aluminum, similar to the body of the UAV. The skin depth of the aluminum at 110 kHz is 247.25 μm , and the thickness of the aluminum coil case is 3 mm. Therefore, the magnetic field generated by the WPT coil cannot affect the inside of the UAV where the other systems are located.

For miniaturization, the inverter for supplying AC power is located at the bottom of the source coil. The rectifying circuits are directly mounted on the body of the UAV to optimize space.

Conventionally, the size of the transmitting and receiving coils needs to be small because of the limited space in UAVs. However, the small size and the long distance between the transmitting and the receiving coils mean that the coupling coefficient is also small, which can reduce the power transfer effi-

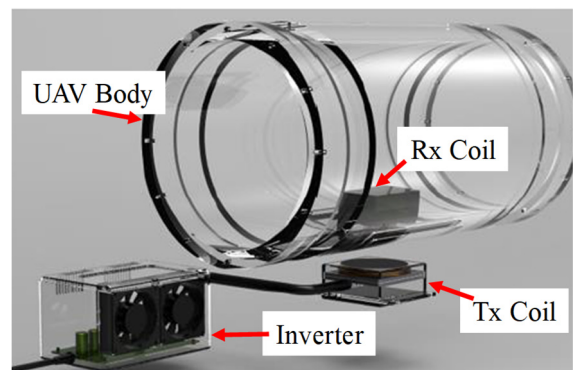


Fig. 3. Configuration of wireless power transfer system for unmanned vehicle.

ciency. At the same transmission distance, a larger-sized WPT Tx coil produces greater power transmission efficiency. Therefore, the coil sizes are chosen according to the given Rx space.

1. Conventional WPT Coil 1 for the Cordless Umbilical Connector of UAVs

A conventional WPT coil 1 [9] is simply a loop coil of the ferromagnetic material with resonance matching capacitance. This WPT coil is simple to design and implement in UAVs, as shown in Fig. 4. Given the small size of the transmitting and receiving coils, the coupling coefficient is small and can cause the diminution of the power transfer efficiency. The geometrical parameters of the conventional WPT coil 1 are shown in Table 1. The material properties of the WPT system for UAVs are presented in Table 2.

When the highly permeable ferrite is designed with a convex shape, its magnetoresistance becomes lower than that of planar ferrite. In the convex configuration, the ferrite acts as a shaped magnetic field in resonance (SMFIR), which forms a magnetic flux generated by the magneto motive force of the coil along the ferrite with a low magnetic reluctance [10]. A schematic illustrating the concept of the magnetic field formed by the SMFIR is shown in Fig. 5. As a result of this design, the magnetic flux generated by the current flowing in the transmitting part is tightly linked to the receiving part.

However, when the size of the coil is much smaller than the distance between the two coils, the coupling coefficient (K) is limited. The size of the conventional coil 1 is shown in Table 1.

The vertical direction of the magnetic flux generated by the source coil (or load coil) is captured by the load coil (or source coil) ferrite. The narrow effective area of the ferrite is shown in Fig. 4. The magnetic flux cannot link the opposite coil, thus

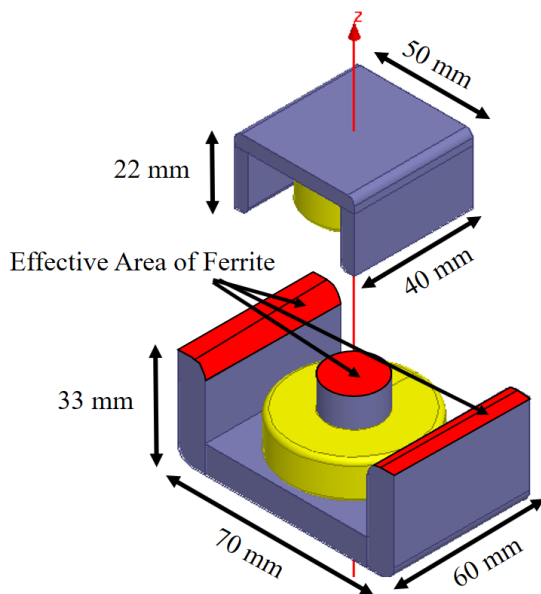


Fig. 4. Over all view of conventional WPT system 1 for UAVs.

Table 1. Geometrical parameters of conventional coil (CC) and proposed toroidal-shaped coil

Parameter	CC 1	CC 2	Proposed coil
Tx coil size (mm)	70 × 60 × 33	140 × 50 × 20	140 × 50 × 20
Rx coil size (mm)	50 × 40 × 22	146 × 40 × 22	50 × 40 × 22
Rx wing size (mm)	-	-	48 × 34 × 3
Tx turns (turns)	19	19	19
Rx turns (turns)	15	8	8
Air gap (mm)	50	50	50

Table 2. Material properties of WPT systems for UAVs

Parameter	Ferrite	Aluminum	Copper
Conductivity (S/m)	1.0 e-2	3.8 e7	5.8 e7
Relative permeability	1000	1	1

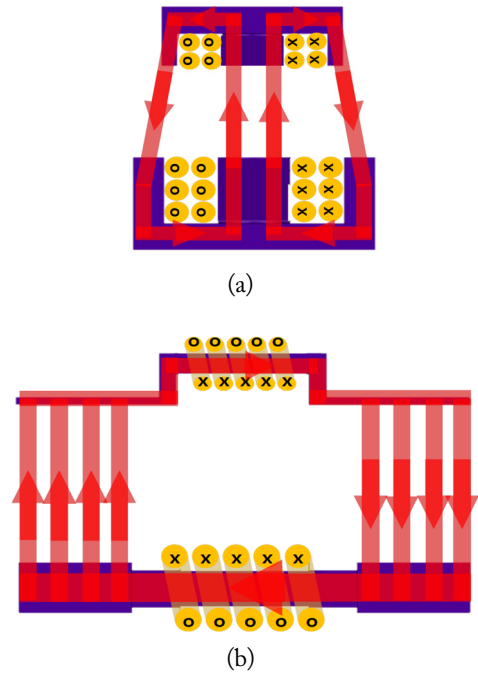


Fig. 5. Schematic of the shaped magnetic field with a conventional coil (b) and the proposed toroidal coil (a) using a ferromagnet.

causing the WPT coil system to have a low coupling coefficient. For higher power transfer efficiency, a broader effective area of ferrite is needed.

2. Conventional WPT Coil 2 for a Cordless Umbilical Connector of UAVs

A conventional WPT coil 2 [9] has a loop coil and a ferromagnetic material with resonance matching capacitance. As shown in Table 1, the conventional WPT system 2 has a larger coil size to increase the coupling coefficient. As the effective area increases, the volume of the coil system also greatly increases (Fig. 6).

The electronic and mechanic devices of UAVs are embedded

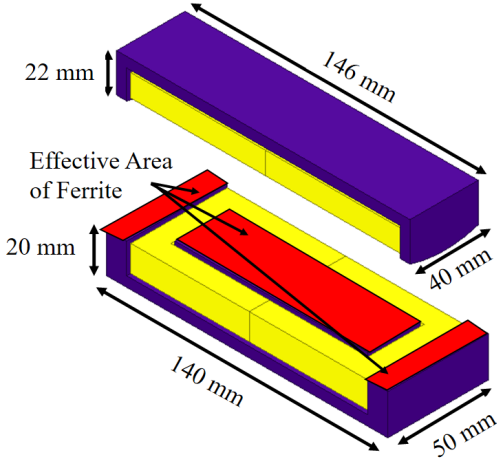


Fig. 6. Overall view of the conventional WPT system 2 for UAVs.

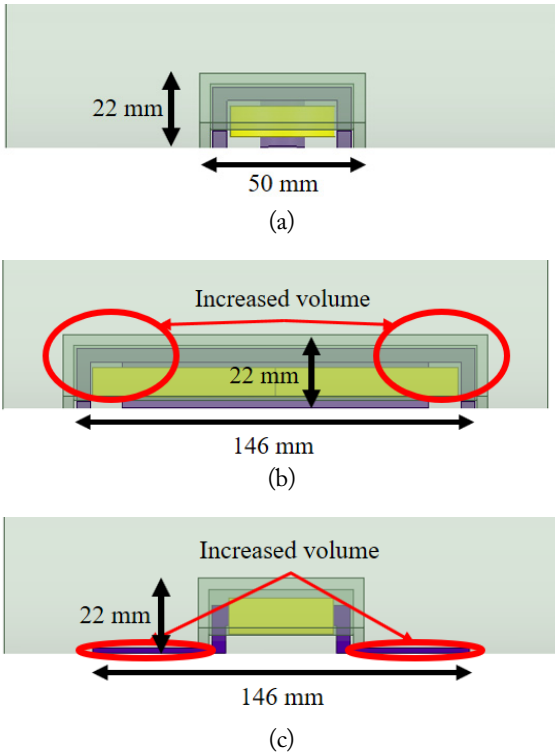


Fig. 7. Application of (a) conventional WPT system 1. (b) conventional WPT system 2. (c) proposed toroidal-shaped WPT system.

inside the craft to protect against external impact. Therefore, the coil system should not require an increased volume. Otherwise, it cannot be applied as a UAV WPT system because any increase in the volume of the WPT system limits the load of other devices in the UAV, as shown in Fig. 7(b).

3. Proposed Toroidal-Shaped Coil for Cordless Umbilical Connector of UAVs

The proposed toroidal-shaped coil has a transversely wound coil and a wing-shaped ferrite. The toroidal-shaped coil is wound the same as a solenoidal coil, as shown in Fig. 5. The

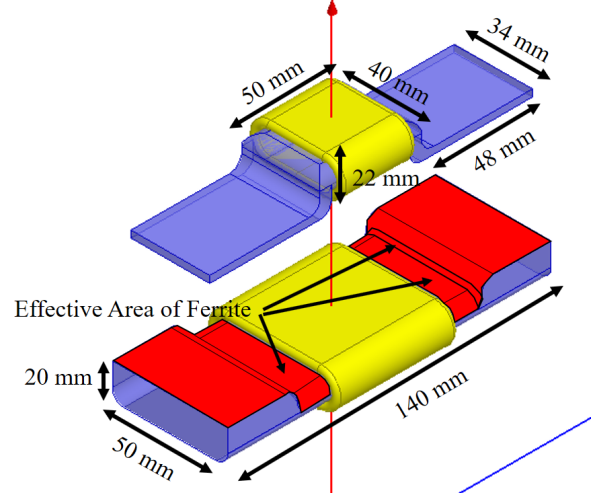


Fig. 8. Overall view of the proposed toroidal-shaped WPT coils for UAVs.

size of the proposed toroidal-shaped coil is listed in Table 1. The volume of the transmitting coil is the same as that of the conventional coil system 1.

Unlike its interior, the exterior surface of the UAV can be easily used without spatial limitation. To take advantage of the unused surface area, the wing-shaped ferrite was designed with a thin flat bar shape, as shown in Fig. 8.

The wing-shaped ferrite can minimize the use of the internal space of UAVs and at the same time widen the effective area of the ferrite. The proposed coil can be embedded into the UAV, as shown in Fig. 7(c). The increased area of the proposed coil system is much smaller than that of the conventional coil 2. The proposed coil can increase the coupling coefficient without affecting the volume inside the UAV.

The increased effective area of ferrite can also reduce reluctance. That is, when the WPT coil system has a broader effective area of ferrite, the reluctance of the WPT coil system is reduced. The proposed toroidal coil maximizes the effective area of ferrite, which can increase the coupling coefficient with a minimal increase in space.

III. SIMULATION OF THE WPT SYSTEM FOR A CORDLESS UMBILICAL CONNECTOR OF UAVS

1. Simulation Setup

In the simulation, the operating frequency was set to 110 kHz, and a sinusoidal current flowed through the transmitting coil for a 300-W power transfer. To design the receiving and transmitting coils of the WPT system, a finite element analysis-based magnetic field simulation was used (ANSYS Maxwell Simulation; ANSYS Inc., Canonsburg, PA, USA).

The simulations were conducted under three conditions: a conventional WPT coil 1, a conventional WPT coil 2, and the proposed toroidal-shaped coil. Fig. 9 shows the overall simula-

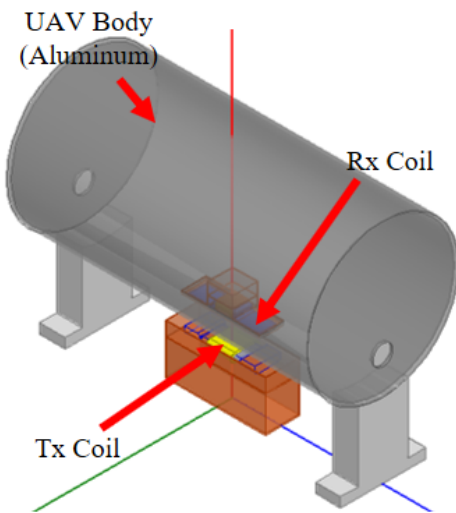


Fig. 9. Overall setup for the simulation.

tion setup for each coil. The geometrical parameters of each coil system are shown in Table 1. The cross-section of the conventional coils and the proposed toroidal-shaped coil are illustrated in Fig. 10.

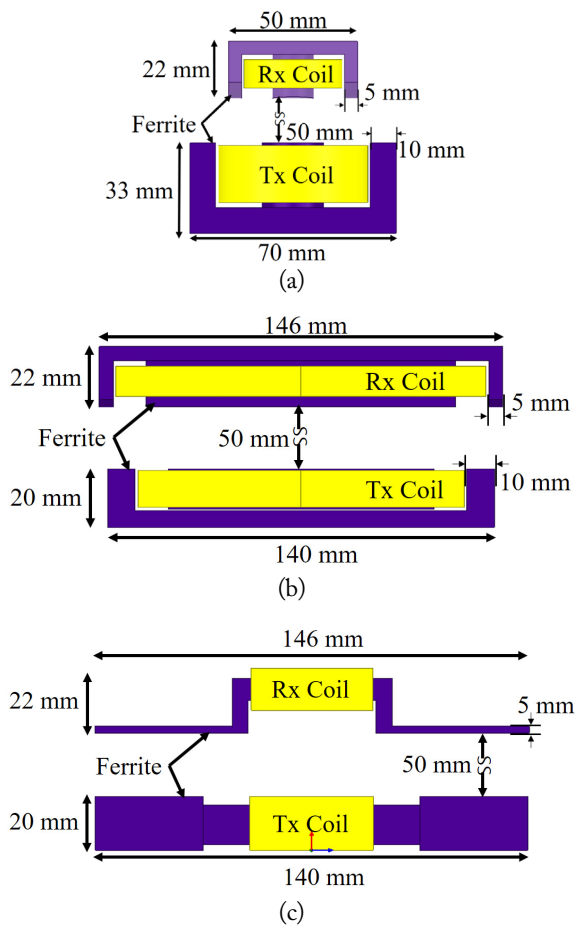


Fig. 10. Side view of the simulation configuration. (a) Conventional WPT coil system 1, (b) conventional WPT coil system 2, and (c) proposed toroidal-shaped coil system.

Although the total size of the proposed coil system is slightly larger than that of the conventional coil system 1, the volume inside the UAV is the same, and the increased volume of the coil is applied to the surface of the UAV that is not being used to mount the device.

Three-dimensional (3D) finite element analysis simulations (ANSYS Maxwell) were conducted to compare the electrical parameters of the two structures listed in Table 3. The resistances of the Tx and Rx coils were calculated using a simulation with an ideal environment, where the skin effect and the proximity effect were neglected. To compare the power transfer efficiency, a circuit simulation was performed. The values of the compensation capacitors of the transmitting and receiving coils were determined on the basis of the operating frequency, and a full bridge rectifier and a smoothing capacitor were constructed.

2. Comparison of Power Transfer Efficiencies

The input power of the system is the power supplied from the DC power supply in front of the transmitting coil. The power delivered to the receiver is measured at the back of the receiving coil. The overall system efficiency is the ratio of the power delivered to the load to the system input power. The simulation results are shown in Table 4. The conventional coil system 1 has low power transfer efficiency because of the different sizes of the transmitting and receiving coils. The aluminum

Table 3. Electrical parameters of the conventional coils (CC) and the proposed toroidal-shaped coil

Parameter	CC 1	CC 2	Proposed coil
Tx resistance (mΩ)	5.58	13.25	24.19
Rx resistance (mΩ)	5.51	7.89	11.23
Tx self-inductance (μH)	64.61	181.0	31.15
Tx matching capacitor (nF)	32.39	11.56	67.20
Rx self-inductance (μH)	6.01	2.76	9.90
Rx matching capacitor (nF)	348.20	758.48	211.33
Mutual inductance (μH)	0.28	0.67	3.71
Coupling coefficient	0.014	0.030	0.21
Resonance frequency (kHz)	110	110	110

Table 4. Simulated input, output power, and power transfer efficiency of conventional coils (CC) and the proposed toroidal-shaped coil

Parameter	CC 1	CC 2	Proposed coil
Input power (W)	633.7	467.6	365.7
Output power (W)	299.9	303.1	309.5
Power transfer efficiency (%)	47.3	64.8	84.6

case around the receiving coil decreases the coupling coefficient by canceling the magnetic flux generated by the eddy currents on the aluminum.

The conventional coil system 2 is found to have increased power transfer efficiency in comparison with the conventional coil system 1 because the transmitting and receiving coils were similar in size. The canceling magnetic field from the aluminum case around the receiving coil has lesser effect on the coupling coefficient between the two coils.

The wing ferrite can capture the magnetic flux generated by the opposite coil, thus increasing the coupling coefficient. By using the wing ferrite, the proposed toroidal-shaped coil increased the power transfer efficiency by 37.3%. The wing ferrite, which is included in the proposed toroidal-shaped coil system, has a dramatic effect on the power transfer efficiency of the WPT system, with minimal additional space requirements.

IV. MEASUREMENT OF THE WPT SYSTEM FOR A CORDLESS UMBILICAL CONNECTOR OF UAVS

The power transfer efficiency of the proposed toroidal-shaped coil was measured for comparison with the simulated results. As shown in Fig. 11, a 300-W WPT coil system was designed and implemented to experimentally verify the effectiveness of the proposed toroidal-shaped coil. A Litz wire was used for the coil

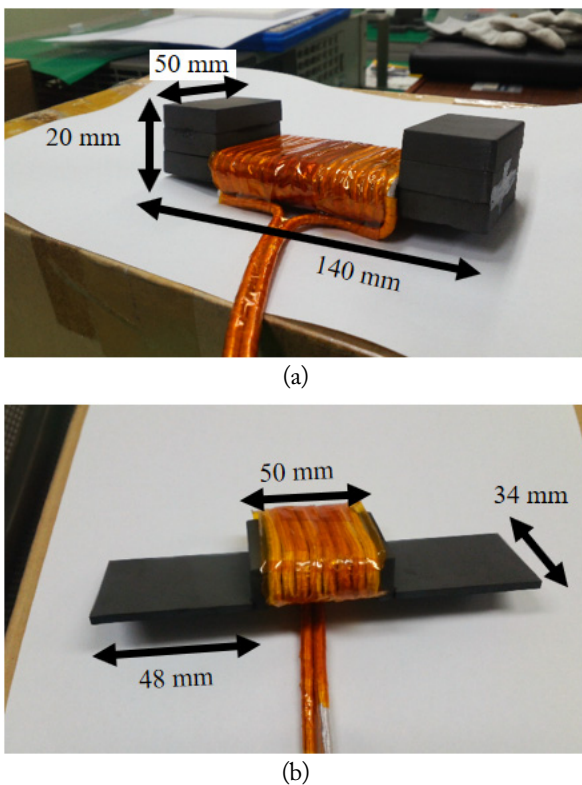


Fig. 11. Manufactured toroidal-shaped coil. (a) Transmitting coil and (b) receiving coil.

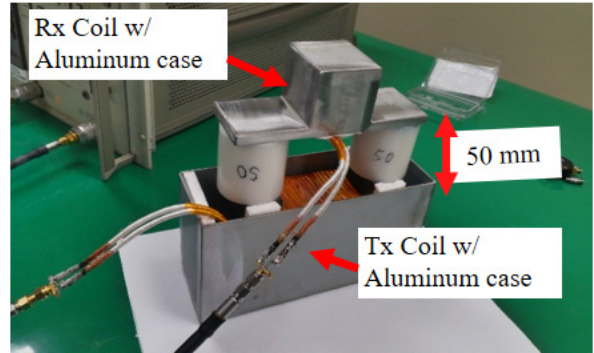


Fig. 12. Configuration of the WPT system for measurement.

Table 5. Comparison of the simulated and measured input, output power, and power transfer efficiency

Parameter	Simulated	Measured
Input power (W)	365.7	360.3
Output power (W)	309.5	302.7
Power transfer efficiency (%)	84.6	84.0

winding to increase the power transfer efficiency by reducing the resistance of the proposed toroidal-shaped coil.

The resonance frequencies of the transmitting and receiving coils were set to 110 kHz as in the simulations. Consistent with the simulations, the power delivered to the load was 300 W, and the voltage targeted was at 28 V. Therefore, the resistance of the electronic load was set to 2.55 Ω .

The size of the coils and the distance between the source and the receiving coils were the same as those in the simulation environment. The overall coil configuration of the experiment is presented in Fig. 12. The case of the source and receiving coils was made with aluminum, which was also used for the case of the UAV. The air gap consisted of acrylic, which did not affect the generation or linkage of the magnetic field. A full-bridge inverter was used to convert DC power to AC power.

Table 5 shows the input power, output power, and efficiency calculated by measuring the current and the voltage at each point. The measurement data correlated well with the simulation data. The proposed toroidal-shaped coil system dramatically increased the power transfer efficiency.

V. CONCLUSION

In this study, we propose a toroidal-shaped coil system using a wing-shaped ferrite to overcome the reduced efficiency resulting from the small coil size of conventional WPT systems, which is their inherent limit, for UAVs. The design and analysis of the proposed toroidal-shaped coil were performed, and comparisons with other coil systems were conducted using simulations and measurements. The simulation results were in good agreement with the results obtained by measurement.

The simulation and measurement results confirm that the proposed toroidal-shaped coil dramatically increases the power transfer efficiency and is significantly better than the other conventional coil systems in UAVs, with a negligible increase in occupied space.

This work was supported by the SPIN-ON application research project sponsored by the Civil Military Technology Cooperation Center in the Agency for Defense Development (No. 16-SN-22-11).

REFERENCES

- [1] K. D. Mullens, E. B. Pacis, S. B. Stancliff, A. B. Burmeister, and T. A. Denewiler, "An automated UAV mission system," *Space and Naval Warfare Systems Command*, San Diego, CA, 2003.
- [2] M. K. Furrutter and J. Meyer, "Small fuel cell powering an unmanned aerial vehicle," in *Proceedings of IEEE AFRICON*, Nairobi, Kenya, 2009, pp. 1–6.
- [3] K. Michals, "UAV power supply maintenance method," 2012; <https://www.flickr.com/photos/rocbolt/7187520615/in/photostream>.
- [4] A. Kurs, A. Karalis, R. Moffatt, J.D. Joannopoulos, P. Fisher, and M. Soljacic, "Wireless power transfer via strongly coupled magnetic resonances," *Science*, vol. 317, no. 5834, pp. 83–86, 2007.
- [5] Collado, J. A, Garcia, et al., "Wireless power transmission: R&D activities within Europe," *IEEE Transactions on Microwave Theory and Technology*, vol. 62, no. 4, pp. 1031–1045, 2014.
- [6] S. Kim and B. Lee, "Analysis of efficiencies for multiple-input multiple-output wireless power transfer systems," *Journal of Electromagnetic Engineering and Science*, vol. 16, no. 2, pp. 126–133, 2016.
- [7] S. Jeong, M. Kim, J. H. Jung, and J. Kim, "An effective experimental optimization method for wireless power transfer system design using frequency domain measurement," *Journal of Electromagnetic Engineering and Science*, vol. 17, no. 4, pp. 208–220, 2017.
- [8] W. Huang and H. Ku, "Analysis and optimization of wireless power transfer efficiency considering the tilt angle of a coil," *Journal of Electromagnetic Engineering and Science*, vol. 18, no. 1, pp. 13–19, 2018.
- [9] J. Kim, J. Kim, S. Kong, H. Kim, I. S. Suh, N. P. Suh, D. H. Cho, J. Kim, and S. Ahn, "Coil design and shielding methods for a magnetic resonant wireless power transfer system," *Proceedings of the IEEE*, vol. 101, no. 6, pp. 1332–1342, 2013.
- [10] J. Shin, S. Shin, Y. Kim, S. Ahn, S. Lee, G. Jung, S. J. Jeon, and D. H. Cho, "Design and implementation of shaped magnetic-resonance-based wireless power transfer system for roadway-powered moving electric vehicles," *IEEE Transactions on Industrial Electronics*, vol. 61, no. 3, pp. 1179–1192, 2014.

Jaehyoung Park



received his M.S. degree from the Korea Advanced Institute of Science and Technology (KAIST), Daejeon, Korea, in 2014. He is currently completing his Ph.D. degree in KAIST. His current research interests include the electromagnetic compatibility issues in wireless power transfer.

Jonghoon Kim



received his Ph.D. degree from the Department of Electrical Engineering of the Korea Advanced Institute of Science and Technology (KAIST), Daejeon, Korea, in 2003. His master and doctoral theses were focused on the reduction of electromagnetic interference (EMI) from a high-speed digital system. After receiving his Ph.D. degree, he joined the Memory Division of Samsung Electronics, Korea, in 2003.

Since then, he gained experience in the standardization for DDR3/DDR4 memory and in the design of semiconductor test hardware for high-speed memory. He moved to KAIST in 2010 to become a research professor of the Division of Future Vehicle. Since joining KAIST, he gained experience in module/component design for automobile and in electromagnetic compatibility design of a wireless power transfer system for electric vehicles. He became the president of EMC Doctors Inc. in 2017. His current research interests include signal integrity, power integrity, and EMI/EMC of high-speed digital systems and the analysis and design of WPT systems.

Yujun Shin



received his B.S. degree in electrical engineering from Inha University, Incheon, Korea, in 2016. He is currently completing his Ph.D. degree at the Korea Advanced Institute of Science and Technology. His main research interests are in wireless power transfer systems for electric vehicle systems.

Seok-Jong Cheong



received his B.S. degree in electronic engineering from Yonsei University, Seoul, Korea, in 1980 and his M.S. degree in computer science at the Korea Advanced Institute of Science and Technology in 1996. He worked for Guidance and Control Part of the missile system in ADD, Daejeon, Korea, from 1980 to 1998. Since 1999, he gained various experiences in commercial fields, such as geolocation systems, cellular mobiles, ETCS, and wearable devices, among others. Now, he belongs to WISTEK Co. Ltd. His current research interests are wireless power transmissions, radar systems, and other RF systems.

Bumjin Park



received his B.S. degree in electrical engineering from Chungnam National University, Daejeon, Korea, in 2015 and his M.S. degree from the Korea Advanced Institute of Science and Technology (KAIST), Daejeon, Korea, in 2017. He is currently completing his Ph.D. degree at KAIST. His current research interests include magnetic material and magnetic energy harvesting.

Seungyoung Ahn



received his B.S., M.S., and Ph.D. degrees at the Korea Advanced Institute of Science and Technology (KAIST), Korea, in 1998, 2000, and 2005, respectively. He is currently an associate professor at KAIST. His research interests are WPT system design and electromagnetic compatibility design for electric vehicles and digital systems.

Won-Seok Kim



received his B.S. degree in Information and Communication engineering from Daegu University, Daegu, Korea, in 2001. Now, he belongs to WISTEK Co. Ltd. His current research interests are wireless power transmission, radar system, and many other RF systems.

Design Method for Negative Group Delay Circuits Based on Relations among Signal Attenuation, Group Delay, and Bandwidth

Sehun Na¹ · Youn-Kwon Jung² · Bomson Lee^{1,*}

Abstract

Typical negative group delay circuits (NGDC) are analyzed in terms of signal attenuation, group delay, and bandwidth using S -parameters. By inverting these formulations, we derive and present the design equations (for NGD circuit elements) for a desired specification of the two among the three parameters. The proposed design method is validated through simulation examples for narrow- and wide-band pulse inputs in the time and frequency domains. Moreover, an NGDC composed of lumped elements is fabricated at 1 GHz for measurement. As a function of frequency, the circuit-/EM-simulated and measured group delays are in good agreement. The provided simple NGDC design equations may be useful for many applications that require compensations of some signal delays.

Key Words: Bandwidth, Negative Group Delay, Passive Element, Signal Attenuation, Synthesis.

I. INTRODUCTION

Negative group delay (NGD) was initially presented by Brillouin [1] in the 1960s, and it has been studied actively since the research on superluminal effects was published in [2]. The NGD characteristics have been demonstrated in various systems. In the microwave area, NGD circuits are used to compensate for group delays usually caused by the use of filters or amplifiers [3, 4]. Many studies have been conducted to utilize the NGD phenomenon by employing various structures, such as a defected microstrip structure and a defected ground structure [5]. In [6], the familiarity between a non-Foster reactive property and NGD networks with loss compensation was discussed theoretically and experimentally. A loss-compensated NGD network composed of cascading two unit cells and amplifiers was also presented for

larger NGD effects. Some design equations were proposed through an S -parameter analysis [6–9], a lossy coupling matrix synthesis [10], and a filter analysis [11]. The design equations for negative group delay circuit (NGDC) using lumped RLC resonators are also available based on the specification of the signal attenuation and NGD [12, 13]. In this study, we derive the mathematical relations among signal attenuation, NGD, and bandwidth for a convenient and systematic design of the NGDC composed of RLC resonators. The effects of the NGDC are evaluated in the time and frequency domains using narrow- and wide-band pulse inputs. To verify the proposed design equations, we fabricate an NGDC composed of lumped elements at 1 GHz. The group delays of the fabricated NGDC are measured and compared with those obtained from the presented design equations.

Manuscript received May 21, 2018 ; Revised September 12, 2018 ; Accepted November 11, 2018. (ID No. 20180521-043J)

¹Department of Electronics Engineering, College of Electronics and Information, Kyung Hee University, Yongin, Korea.

²Avionics Radar Team, Hanwha Systems, Yongin, Korea.

*Corresponding Author: Bomson Lee (e-mail: bomson@khu.ac.kr)

This is an Open-Access article distributed under the terms of the Creative Commons Attribution Non-Commercial License (<http://creativecommons.org/licenses/by-nc/4.0>) which permits unrestricted non-commercial use, distribution, and reproduction in any medium, provided the original work is properly cited.

© Copyright The Korean Institute of Electromagnetic Engineering and Science. All Rights Reserved.

II. ANALYSIS AND SYNTHESIS OF A GROUP DELAY CIRCUIT

1. Analysis

Fig. 1(a) shows an equivalent circuit consisting of a parallel resonant circuit connected in a series with a transmission line. Z_0 is the characteristic impedance of the host transmission line. Fig. 1(b) shows an equivalent circuit consisting of a series resonant circuit connected in parallel with a transmission line. Y_0 is the characteristic admittance. Most passive NGD structures can be modeled on the basis of these equivalent circuits in Fig. 1(a) and (b).

In Fig. 1(a), the admittance of Y_{NGD} of the parallel resonant circuit can be expressed as

$$Y_{NGD} = G_0 + j\sqrt{\frac{C_0}{L_0}}\left(\frac{\omega}{\omega_0} - \frac{\omega_0}{\omega}\right) \approx G_0 + j2C_0(\omega - \omega_0), \quad (1)$$

where G_0 is the conductance, ω is the angular frequency, ω_0 is the resonant angular frequency given by $1/\sqrt{C_0L_0}$, and $\sqrt{C_0/L_0}$ (or ω_0C_0) is the susceptance slope parameter. The last expression in (1) is an approximation based on the assumption that ω is near ω_0 .

The impedance Z_{NGD} can be approximated as

$$Z_{NGD} = \frac{1}{Y_{NGD}} \approx \frac{G_0 - j2C_0(\omega - \omega_0)}{G_0^2}. \quad (2)$$

Then, the input impedance Z_{in} is the sum of Z_{NGD} and Z_0 . The reflection coefficient S_{11} is obtained as

$$S_{11} = \frac{V_1^-}{V_1^+} = \frac{Z_{in} - Z_0}{Z_{in} + Z_0} = \frac{Z_{NGD}}{Z_{NGD} + 2Z_0} = \frac{G_0^2(1 + 2Z_0G_0) + 4C_0^2(\omega - \omega_0) - j4Z_0G_0^2C_0(\omega - \omega_0)}{G_0^2(1 + 2Z_0G_0)^2 + 4C_0^2(\omega - \omega_0)^2}. \quad (3)$$

When $\omega = \omega_0$, S_{11} (3) is simplified to

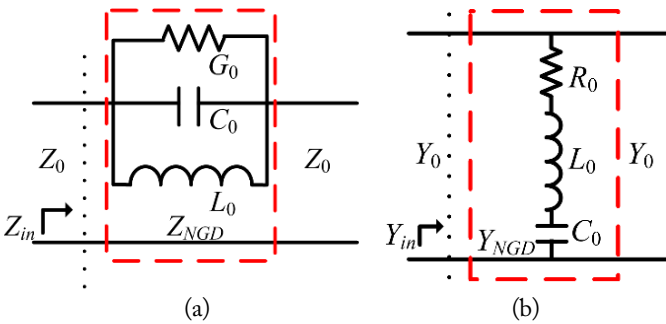


Fig. 1. (a) Equivalent circuit for the NGD structure made of a parallel GCL resonator connected in a series with a transmission line. (b) Equivalent circuit for the NGD structure made of a series RLC resonator connected in parallel with the transmission line.

$$S_{11} = \frac{1}{1 + 2Z_0G_0}. \quad (4)$$

The transmission coefficient (S_{21}) of the NGDC unit cell can be obtained by the ratio of the transmitted voltage (V_2^-) and input voltage (V_1^+) given by

$$S_{21} = \frac{V_2^-}{V_1^+} = \frac{2Z_0}{2Z_0 + Z_{NGD}} \approx \frac{2Z_0G_0(1 + 2Z_0G_0) + j4Z_0C_0(\omega - \omega_0)}{(1 + 2Z_0G_0)^2}. \quad (5)$$

The real and imaginary parts of S_{21} are represented by

$$\text{Re}[S_{21}] = \frac{2Z_0G_0}{1 + 2Z_0G_0} \quad (6)$$

and

$$\text{Im}[S_{21}] = \frac{2Z_0[2C_0(\omega - \omega_0)]}{(1 + 2Z_0G_0)^2}, \quad (7)$$

respectively.

S_{21} (5) at ω_0 is simplified to

$$S_{21}(\omega_0) = \frac{2Z_0G_0}{1 + 2Z_0G_0}, \quad (8)$$

which is purely real and positive. That is, the transmission at ω_0 across the NGDC in Fig. 1(a) occurs without a phase delay. The phase for the NGDC is obtained as

$$\phi(\omega) = \angle S_{21} = \tan^{-1} \frac{\text{Im}[S_{21}]}{\text{Re}[S_{21}]} = \tan^{-1} \frac{2C_0(\omega - \omega_0)}{G_0(1 + 2Z_0G_0)}. \quad (9)$$

Then, the group delay (τ) [8] can be shown to be given by

$$\tau(\omega) = -\frac{d\phi}{d\omega} = -\frac{2C_0G_0[1 + 2Z_0G_0]}{G_0^2[1 + 2Z_0G_0]^2 + [2C_0(\omega - \omega_0)]^2}, \quad (10)$$

which is negative, and its magnitude is observed to become maximum at the resonant angular frequency ω_0 and zero when ω is far away from ω_0 . The group delay is another word for a signal envelope delay [14]. The frequency dependence in (10) prevents a pulse input from being entirely copied in advance of the input at the output terminal. The maximum NGD is expressed as

$$\tau(\omega_0) = -\left.\frac{d\phi}{d\omega}\right|_{\omega=\omega_0} = -\frac{2C_0}{G_0(1 + 2Z_0G_0)}. \quad (11)$$

As G_0 becomes smaller, the signal transmission becomes smaller, as implied by (8), but the effect of the NGD becomes larger, as shown by (11). The magnitude of the NGD is shown to be proportional to C_0 as is the susceptance slope ω_0C_0 .

Fig. 2 shows the magnitudes and phases of S_{21} when $\tau(\omega_0)$ (11) is assumed to be -0.5 , -1 , and -5 ns and $S_{21}(\omega_0) = 0.5$ at

1 GHz. In the case of $\tau(\omega_0) = -1$ ns, $Z_0 = 50 \Omega$, $G_0 = 1/100$ ($1/\Omega$), $C_0 = 10$ pF, and $L_0 = 2.53$ nH. As the magnitude of $\tau(\omega_0)$ becomes larger, the bandwidth of the NGD becomes smaller. This will result in more signal distortion if an input signal bandwidth is wider than the NGDC bandwidth. The positive phase slopes near 1 GHz shown in Fig. 2(b) lead to NGD s, as explained in (10).

So far, we have analyzed the NGD equivalent circuit given in Fig. 1(a) in terms of the signal transmission S_{21} and NGD τ .

2. Synthesis

On the contrary, if specific values of $S_{21}(\omega_0)$ and $\tau(\omega_0)$ are desired for a particular NGD circuit design, (8) and (11) can be simultaneously solved for the design equations given by

$$G_0 = \frac{S_{21}(\omega_0)}{2Z_0[1 - S_{21}(\omega_0)]}, \quad (12)$$

$$C_0 = \frac{|\tau(\omega_0)|G_0(1 + 2Z_0G_0)}{2} = \frac{|\tau(\omega_0)|S_{21}(\omega_0)}{4Z_0[1 - S_{21}(\omega_0)]^2}, \quad (13)$$

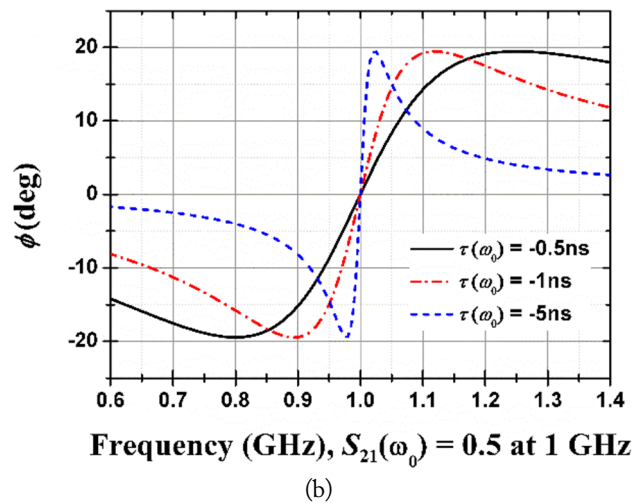
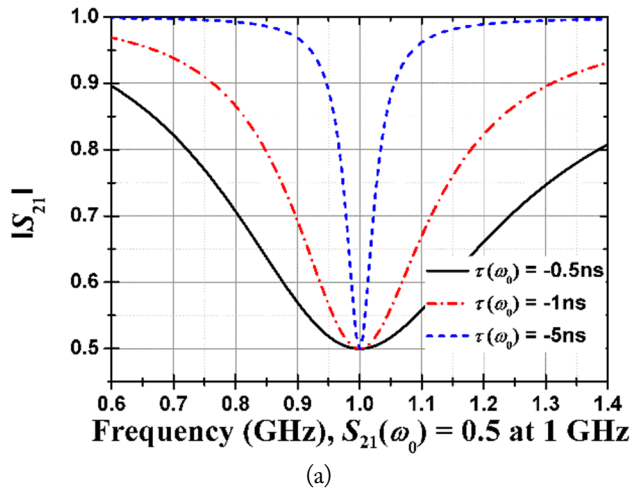


Fig. 2. (a) Magnitudes of S_{21} . (b) Phases of S_{21} for different group delays when $S_{21}(\omega_0)$ is fixed at 0.5 at 1 GHz.

and L_0 is obtained with

$$L_0 = \frac{1}{\omega_0^2 C_0}. \quad (14)$$

Fig. 3 shows the capacitance values of the NGD circuit for different $S_{21}(\omega_0)$ and $\tau(\omega_0)$ at 1 GHz using (13). Whereas G_0 (12) depends only on $S_{21}(\omega_0)$, C_0 and L_0 depend on both $S_{21}(\omega_0)$ and $\tau(\omega_0)$. Expressions (12)–(14) are actually the design equations to realize the specifically required values of $S_{21}(\omega_0)$ and $\tau(\omega_0)$. With (12) and (13), the quality factor of the NGD circuit may be expressed as

$$Q_{NGD} = \frac{\omega_0 C_0}{G_0} = \frac{\omega_0 |\tau(\omega_0)|}{2[1 - S_{21}(\omega_0)]}. \quad (15)$$

Moreover, the 3 dB fractional bandwidth (BW) is roughly given by

$$BW \approx \frac{1}{Q_{NGD}} = \frac{G_0}{\omega_0 C_0} = \frac{2[1 - S_{21}(\omega_0)]}{\omega_0 |\tau(\omega_0)|}. \quad (16)$$

The bandwidth (16) becomes large as $S_{21}(\omega_0)$ (8) or $\tau(\omega_0)$ (11) becomes small. Note that if the two among the three design parameters $S_{21}(\omega_0)$ (8), $\tau(\omega_0)$ (11), and bandwidth (16) are specified, the rest is determined automatically. This relation is summarized in Table 1.

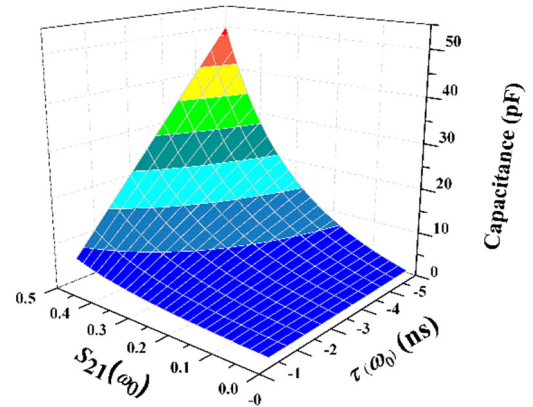


Fig. 3. Capacitance values for different $S_{21}(\omega_0)$ and $\tau(\omega_0)$.

Table 1. Relation among design parameters $S_{21}(\omega_0)$, $\tau(\omega_0)$, and BW

Specified design parameters for NGDC		Determined design parameter
$\tau(\omega_0)$	$S_{21}(\omega_0)$	$BW \approx \frac{2[1 - S_{21}(\omega_0)]}{\omega_0 \tau(\omega_0) }$
$\tau(\omega_0)$	BW	$S_{21}(\omega_0) \approx \frac{2 - \omega_0 \tau(\omega_0) BW}{2}$
$S_{21}(\omega_0)$	BW	$ \tau(\omega_0) \approx \frac{2[1 - S_{21}(\omega_0)]}{\omega_0 BW}$

Fig. 4(a) shows the group delay $\tau(\omega)$ (10) as a function of frequency for different $S_{21}(\omega_0)$'s of -6, -10, and -20 dB when $\tau(\omega_0)$ is -1 ns at 1 GHz. As $S_{21}(\omega_0)$ becomes smaller, the bandwidth of $\tau(\omega)$ becomes larger; this is the important trade-off feature of the presented NGDC. Fig. 4(b) shows $S_{21}(\omega)$ as a function of frequency for the different $S_{21}(\omega_0)$'s of -10, -20, -30, and -40 dB when $\tau(\omega_0)$ is fixed at -1 ns at 1 GHz. The symbols represent the calculated results using (5), and the lines represent the circuit-simulated results based on Fig. 1(a).

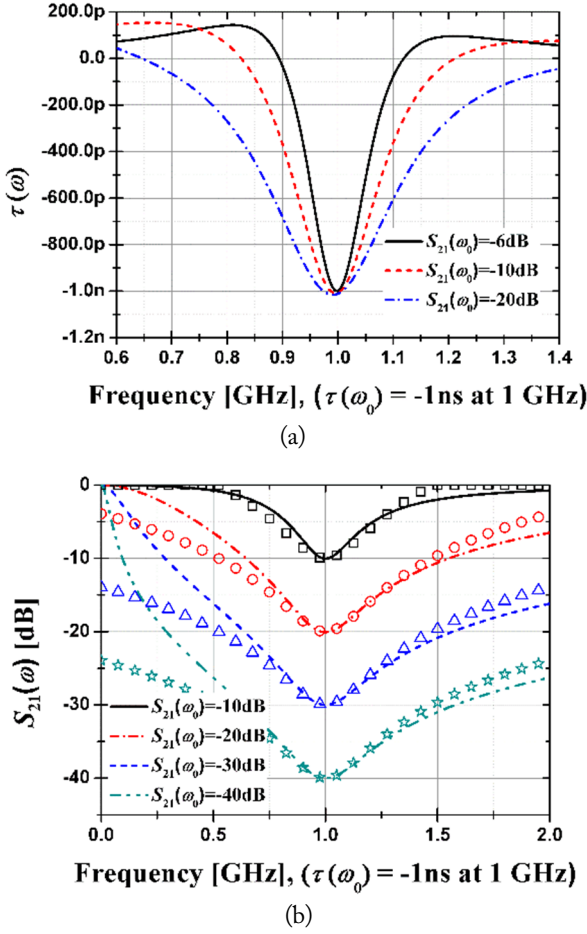


Fig. 4. (a) Group delay $\tau(\omega)$ as a function of frequency for the different $S_{21}(\omega_0)$'s of -6, -10, and -20 dB. (b) $S_{21}(\omega)$ as a function of frequency for the different $S_{21}(\omega_0)$'s of -10, -20, -30, and -40 dB when $\tau(\omega_0) = -1$ ns at 1 GHz (symbols using (5), lines circuit simulations).

Table 2. Q-factors and bandwidth for the different $S_{21}(\omega_0)$'s of -10, -20, -30, and -40 dB when $\tau(\omega_0) = -1$ ns at 1 GHz

	S_{21} (dB)			
	-10	-20	-30	-40
Q-factor	4.595	3.491	3.244	3.173
BW (GHz) (16)	0.218	0.286	0.308	0.315
BW (GHz) (circuit)	0.24	0.29	0.325	0.325

In Table 2, we show the Q factors and compare the bandwidths based on (16) and circuit simulations. The results in Fig. 4(b) and Table 2 prove the theory to be accurate enough when ω is near ω_0 .

In Fig. 5, we show the 3 dB fractional bandwidth (16) of the NGDC as a function of $S_{21}(\omega_0)$ and $\tau(\omega_0)$. The bandwidth increases as $S_{21}(\omega_0)$ decreases and $|\tau(\omega_0)|$ gets smaller.

Table 3 shows the circuit element values of the NGDC obtained using the design Eqs. (12)–(14) assuming that $S_{21}(\omega_0) = 1/2, 1/\sqrt{10},$ and $1/10$ and $\tau(\omega_0) = -0.5, -1,$ and -2 ns at 1 GHz. Based on these circuit values, the NGDC circuits as shown in Fig. 1(a) can be easily realized.

Fig. 6 shows the diagram of the NGDC combined with an amplifier. The attenuated signal through the NGDC is shown to be properly amplified using the amplifier. The output signal may be somewhat distorted because the bandwidth of the NGDC is usually smaller than the bandwidth of the input signal.

Fig. 7 shows the envelopes and spectra of the input and output signals. The rising/falling time and the width of the input pulse are 3 ns and 1 ns, respectively. The 1 GHz carrier signal is shown only in Fig. 7(a) and is hidden in Fig. 7(b). The output with the NGDC is shown to have some NGD features with an attenuation of about 1/10. The effect of NGD is more pronounced after amplification 10 times. The spectrum of the output has more high-frequency components than that of the input, consistent with the time signals in Fig. 7(b).

In Fig. 8(a), we show the envelopes of the input and output

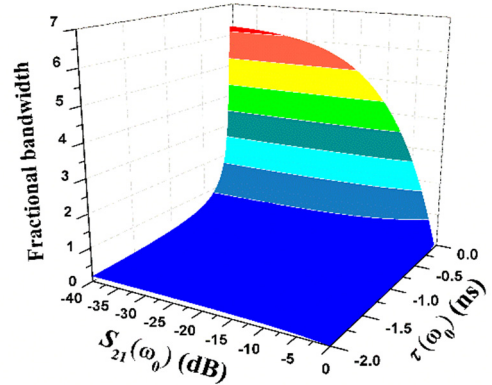


Fig. 5. The 3-dB bandwidth of NGDC as a function of $S_{21}(\omega_0)$ and $\tau(\omega_0)$ at 1 GHz.

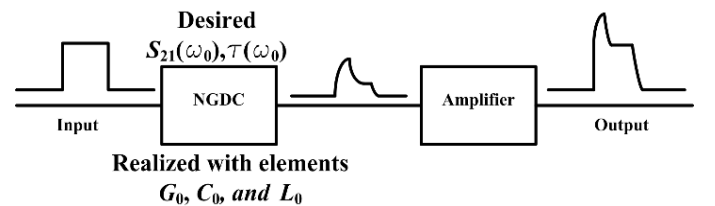


Fig. 6. Diagram of the NGDC combined with an amplifier (brief sketches of the input and output are shown).

Table 3. Calculated circuit values for specific examples

Desired		Solutions for NGD circuit		
$ S_{21}(\omega_0) $	$\tau(\omega_0)$ (ns)	$R_0(\Omega)$ ($= 1/G_0$)	C_0 (pF)	L_0 (nH)
1/2	-0.5	100	5	5.07
	-1		10	2.53
	-2		20	1.27
$1/\sqrt{10}$	-0.5	216.23	1.69	14.98
	-1		3.38	7.49
	-2		6.76	3.75
1/10	-0.5	900	0.31	82.07
	-1		0.62	41.04
	-2		1.23	20.52

signals with $\tau(\omega_0) = -1$ ns and -2 ns, respectively. The rising/falling time and the width of the input pulse are 3 ns and 3 ns, respectively. The carrier frequency is again 1 GHz but not shown. As the magnitude of $\tau(\omega_0)$ increases, the output appears more ahead of the input pulse, but its distortion compared with the input pulse becomes larger. In Fig. 8(b), we show the same when $\tau(\omega_0) = -1, -2,$ and -5 ns. For this case, the rising/falling time and the width of the input pulse are 6 ns and 6 ns, respectively. The input pulse in Fig. 8(b) is slowly varying, and its spectrum should be narrower than that in Fig. 8(a). This leads to less distortion as demonstrated particularly in the case of $\tau(\omega_0) = -2$ ns.

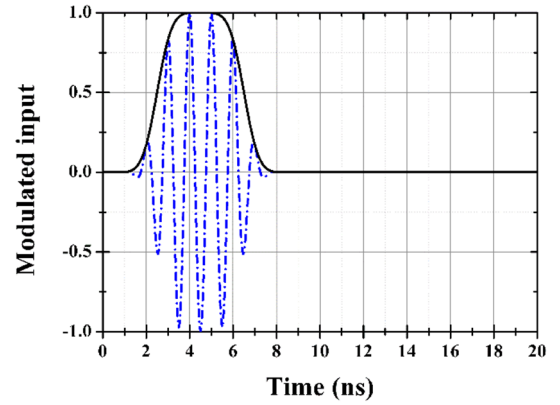
Fig. 9(a) shows the structure of the proposed NGDC composed of lumped RLC elements based on the required $S_{21}(\omega_0) = -20$ dB and $\tau(\omega_0) = -1$ ns at 1 GHz. Fig. 1(b) is the photograph of the measurement setup. The permittivity of the microstrip transmission line with a thickness of 1.6 mm and the lumped element values are $\epsilon_r = 2.2, R_0 = 900 \Omega, C_0 = 0.62$ pF, and $L_0 = 41$ nH using (12)–(14). The S -parameters of the structure are measured using a network analyzer. The influence of the transmission line is de-embedded on the reference plane at the center of the structure.

Table 4 presents the circuit element values calculated using Eqs. (12)–(14), tuned by electromagnetic (EM) simulations, and used for fabrication. The values tuned by the EM simulations are different from the theoretical ones. The actually used element values are the ones closest to the available ones.

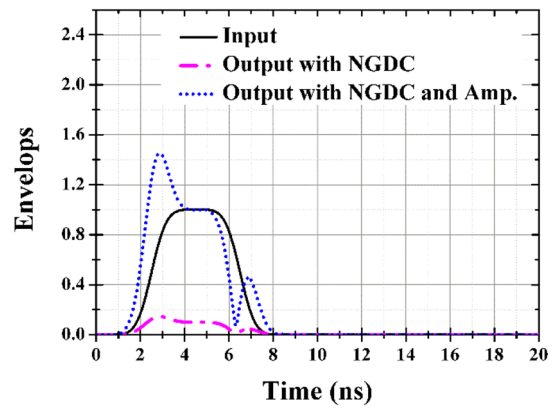
Fig. 10 shows the circuit-/EM-simulated and measured S -parameters and group delays as a function of frequency in the case shown in Fig. 9. They all show to be in good agreement. The output time signals to the input pulses are similar to the dotted ones with $\tau(\omega_0) = -1$ ns in Fig. 8(a).

In the case of using N unit cells in Fig. 1(a), (8) can be shown to be generalized to

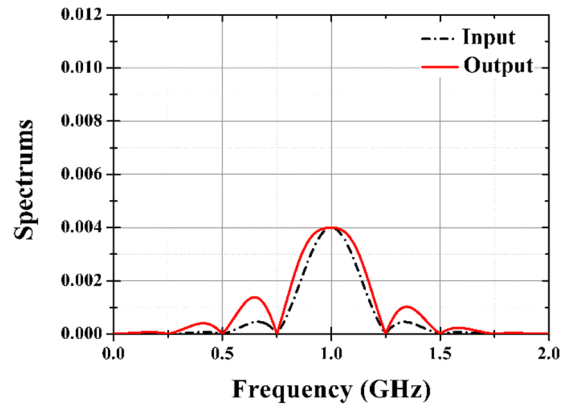
$$S_{21}(\omega_0) = \frac{2Z_0G_0}{N + 2Z_0G_0} \quad (17)$$



(a)



(b)



(c)

Fig. 7. (a) Modulated input signal and carrier as a function of time. The rising/falling time and the width of the input pulse are 3 ns and 1 ns, respectively. The carrier frequency is 1 GHz. (b) Envelopes of the input and output as a function of time with the desired $\tau(\omega_0) = -1$ ns and $S_{21}(\omega_0) = -20$ dB. (c) Spectra of the input and output as a function of frequency.

and (11) to

$$\tau(\omega_0) = -\left. \frac{d\phi}{d\omega} \right|_{\omega=\omega_0} = -\frac{2NC_0}{NG_0 + 2Z_0G_0^2}. \quad (18)$$

As the number N of the identical unit cells increases, the signal transmission (17) decreases but the NGD (18) does not change

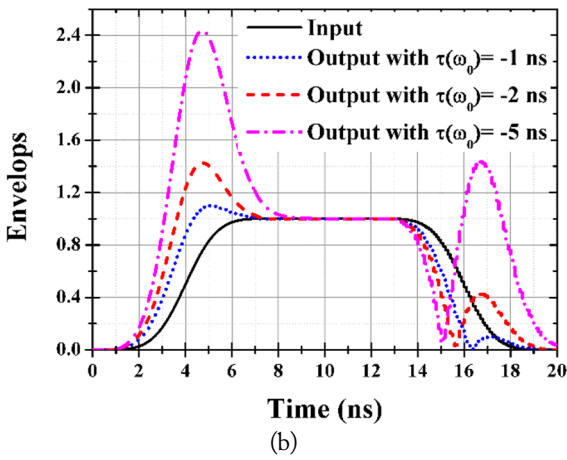
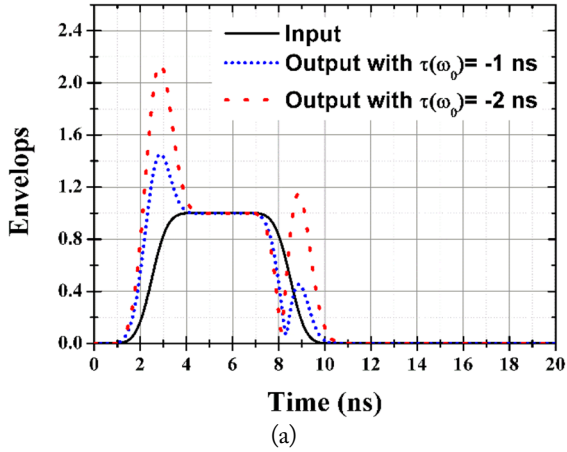


Fig. 8. (a) Circuit-simulated envelopes of the input and output signals as a function of time with the desired $S_{21}(\omega_0) = -20$ dB for different $\tau(\omega_0) = -1$ ns and -2 ns. The rising/falling time and the width of the input pulse are 3 ns and 3 ns, respectively. The hidden carrier frequency is 1 GHz. (b) Envelopes of the input and output as a function of time with the desired $S_{21}(\omega_0) = -20$ dB for different $\tau(\omega_0) = -1, -2,$ and -5 ns. The rising/falling time and the width of the input pulse are 6 ns and 6 ns, respectively. The hidden carrier frequency is 1 GHz.

Table 4. Lumped element values for the case in which $S_{21}(\omega_0) = -20$ dB and $\tau(\omega_0) = -1$ ns at 1 GHz

	R (Ω)	L (nH)	C (pF)
Theory (12)–(14)	900	41	0.62
Tuned by EM	900	37	0.55
Used for fabrication	900	33	0.5

much.

In the case of the NGDC in Fig. 1(b), the analysis and design equations are obtained by simply converting $Z_0, G_0, C_0, L_0,$ and Z_{in} in this study to $Y_0, R_0, L_0, C_0,$ and Y_{in} using the duality principle. The presented design method is applicable to other previous passive NGD circuits, not just the one demonstrated in this study.

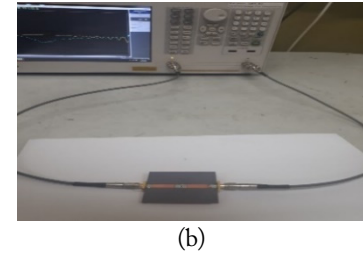
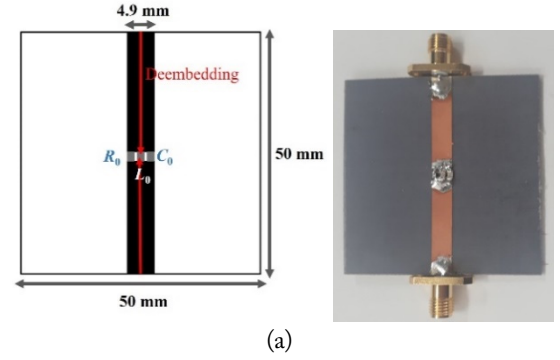


Fig. 9. (a) Fabricated NGDC composed of lumped RLC elements based on the required $S_{21}(\omega_0) = -20$ dB and $\tau(\omega_0) = -1$ ns at 1 GHz ($\epsilon_r = 2.2$, thickness = 1.6 mm, $R_0 = 900 \Omega$, $C_0 = 0.5$ pF, and $L_0 = 33$ nH). (b) Photograph of the measurement setup.

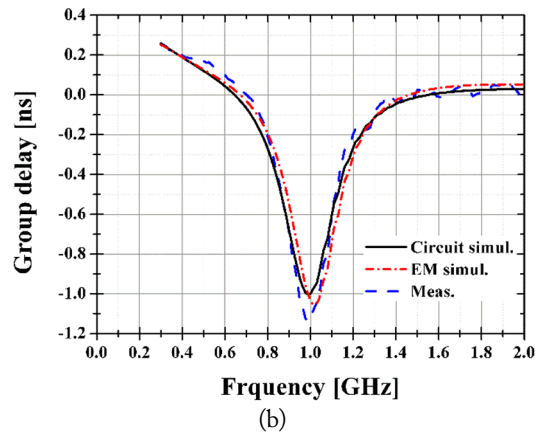
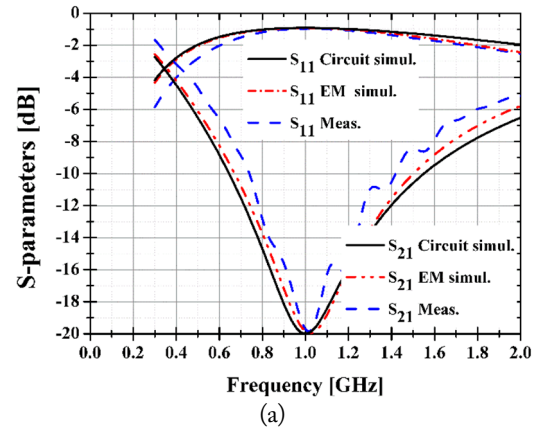


Fig. 10. Circuit-/EM-simulated and measured results of the NGD circuit when $S_{21}(\omega_0) = -20$ dB and $\tau(\omega_0) = -1$ ns at 1 GHz. (a) S -parameters $S(\omega)$. (b) Group delay $\tau(\omega)$.

III. CONCLUSION

Then characteristics of NGD circuits are systematically characterized using $S_{21}(\omega_0)$, $\tau(\omega_0)$, and bandwidth. Some design examples are provided and analyzed in the time and frequency domains. The relations among $S_{21}(\omega_0)$, $\tau(\omega_0)$, and the group delay bandwidth are explained using closed-form expressions. The circuit-/EM-simulated and the measured S -parameters and group delays are all shown to be in good agreement. The presented NGDC design methods may be useful for many applications, such as filters, feed-forward amplifiers, array antennas, and non-Foster reactive elements, among others.

This work was supported by the Institute for Information & Communications Technology Promotion (IITP) grant funded by the Korea government (MSIT) (No. IITP-2019-2016-0-00291, Information Technology Research Center).

REFERENCES

- [1] L. Brillouin, *Wave Propagation and Group Velocity*. New York, NY: Academic Press, 1960.
- [2] L. J. Wang, A. Kuzmich, and A. Dogariu, "Gain-assisted superluminal light propagation," *Nature*, vol. 406, no. 6793, pp. 277–279, 2000.
- [3] M. Kitano, T. Nakanishi, and K. Sugiyama, "Negative group delay and superluminal propagation: an electronic circuit approach," *IEEE Journal of Selected Topics in Quantum Electronics*, vol. 9, no. 1, pp. 43–51, 2003.
- [4] L. F. Qiu, L. S. Wu, W. Y. Yin, and J. F. Mao, "Absorptive bandstop filter with prescribed negative group delay and bandwidth," *IEEE Microwave and Wireless Components Letters*, vol. 27, no. 7, pp. 639–641, 2017.
- [5] G. Chaudhary, Y. Jeong, and J. Lim, "Miniaturized dual-band negative group delay circuit using dual-plane defected structures," *IEEE Microwave and Wireless Components Letters*, vol. 24, no. 8, pp. 521–523, 2014.
- [6] H. Mirzaei and G. V. Eleftheriades, "Realizing non-foster reactive elements using negative-group-delay networks," *IEEE Transactions on Microwave Theory and Techniques*, vol. 61, no. 12, pp. 4322–4332, 2013.
- [7] B. Ravelo, A. Perennec, and M. Le Roy, "Synthesis of broadband negative group delay active circuits," in *Proceedings of 2007 IEEE/MTT-S International Microwave Symposium*, Honolulu, HI, 2007, pp. 2177–2180.
- [8] B. Ravelo, A. Perennec, M. L. Roy, and Y. G. Boucher, "Active microwave circuit with negative group delay," *IEEE Microwave and Wireless Components Letters*, vol. 17, no. 12, pp. 861–863, 2007.
- [9] M. Kandic and G. E. Bridges, "Asymptotic limits of negative group delay in active resonator-based distributed circuits," *IEEE Transactions on Circuits and Systems I: Regular Papers*, vol. 58, no. 8, pp. 1727–1735, 2011.
- [10] R. Das, Q. Zhang, and H. Liu, "Lossy coupling matrix synthesis approach for the realization of negative group delay response," *IEEE Access*, vol. 6, pp. 1916–1926, 2018.
- [11] J. Park, G. Chaudhary, J. Jeong, and Y. Jeong "Microwave negative group delay circuit: filter synthesis approach," *Journal of Electromagnetic Engineering and Science*, vol. 16, no. 1, pp. 7–12, 2016.
- [12] H. Choi, K. Song, C. D. Kim, and Y. Jeong, "Synthesis of negative group delay time circuit," in *Proceedings of 2008 Asia-Pacific Microwave Conference*, Macau, China, 2008, pp. 1–4.
- [13] C. D. Broomfield and J. K. A. Everard, "Broadband negative group delay networks for compensation of microwave oscillators and filters," *Electronics Letters*, vol. 36, no. 23, pp. 1931–1933, 2000.
- [14] R. E. Collin, *Foundations for Microwave Engineering*. New York, NY: McGraw-Hill Inc., 1992.

Sehun Na



received his B.S. degree in electronics engineering from Kyung Hee University, Yongin, Korea, in 2016. He is currently pursuing his master's degree in electronics engineering from Kyung Hee University. His research interests include wireless power transfer systems, passive devices, and small antennas.

Youn-Kwon Jung (M'09)



received his B.S. degree in radio communication engineering from Kyung Hee University, Yongin, Korea, in 2008 and his M.S. and Ph.D. degrees in electronics and radio engineering from the same university in 2011 and 2016, respectively. In 2016, he joined Hanwha Systems, where he is currently a senior researcher at an Active Electronically Steering Array (AESA) radar research center. His research interests include AESA antennas, system antenna, microwave passive devices, small antennas, RFID reader antennas, wireless power transmission, and metamaterials.

Bomson Lee (M'96)



received his B.S. degree in electrical engineering from Seoul National University, Seoul, Korea, in 1982. From 1982 to 1988, he worked at Hyundai Engineering Company Ltd., Seoul, Korea. He received his M.S. and Ph.D. degrees in electrical engineering from the University of Nebraska, Lincoln, NE, USA in 1991 and 1995, respectively. In 1995, he joined the faculty of Kyung Hee University, where he is currently a profes-

sor at the Department of Electronics Engineering. From 2007 to 2008, he was the chair of the technical group for microwave and radio wave propagation in the Korea Institute of Electromagnetic Engineering & Science (KIEES). In 2010, he was Editor-in-Chief of the *Journal of the Korean Institute of Electromagnetic Engineering and Science*. He was vice-chairman in 2015–2016 and executive vice-chairman of KIEES in 2017. Since 2018, he has been the president of KIEES. His research interests include microwave antennas, RF identification tags, microwave passive devices, wireless power transfer, and metamaterials.

SFCFOS Uniform and Chebyshev Amplitude Distribution Linear Array Antenna for K-Band Applications

Venkata Kishore Kothapudi* · Vijay Kumar

Abstract

In this study, a compact series-fed center-fed open-stub (SFCFOS) linear array antenna for K-band applications is presented. The antenna is composed of a single-line 10-element linear array. A symmetrical Chebyshev amplitude distribution (CAD) is used to obtain a low sidelobe characteristic against a uniform amplitude distribution (UAD). The amplitude is controlled by varying the width of the microstrip patch elements, and open-ended stubs are arranged next to the last antenna element to use the energy of the radiating signal more effectively. We insert a series-fed stub between two patches and obtain a low mutual coupling for a 4.28-mm center-to-center spacing (0.7λ at 21 GHz). A prototype of the antenna is fabricated and tested. The overall size of the uniform linear array is $7.04 \times 1.05 \times 0.0563 \lambda_g^3$ and that of the Chebyshev linear array is $9.92 \times 1.48 \times 0.0793 \lambda_g^3$. The UAD array yields a $|S_{11}| < -10$ dB bandwidth of 1.33% (20.912–21.192 GHz) and 1.45% (20.89–21.196 GHz) for the CAD. The uniform array design gives a -23 dB return loss, and the Chebyshev array achieves a -30.68 dB return loss at the center frequency with gains of 15.3 dBi and 17 dBi, respectively. The simulated and measured results are in good agreement.

Key Words: Chebyshev Amplitude Distribution (CAD), Linear Array, Microstrip, Series-Fed Center-Fed Open-Stub (SFCFOS), Uniform Amplitude Distribution (UAD).

I. INTRODUCTION

Series-fed patch array antennas have been known for many years [1] and have also been examined in the context of traveling wave and resonator antennas [2]. For the standard resonator array antenna, each half-wavelength patch is separated by a uniform $\lambda/2$ - transmission line. This important characteristic will lead to a uniform aperture distribution with a broadside radiation pattern if all patches have the same width. In a uniform series antenna circuit model, all radiation resistances of the same value are generally in parallel.

Owing to the half-wavelength patch and line length, these types of antennas provide only a single-frequency operation.

Microstrip patch array antennas are widely applied in radar systems [3–6] and wireless communications systems [7–10], which have a high gain, a light weight, a low cost, and a low profile and can accurately control radiation patterns. Resonant and traveling-wave feeds are commonly used in a series-fed structure. The bandwidth of a traveling-wave feed is wider than that of a resonant feed [8, 9]. However, the main beam angle changes in accordance with the change in operating frequency, which is caused by the change in the relative phase difference between two adjacent elements along the series-fed lines.

Several designs have recently been made to suppress the sidelobe level (SLL) in the printed antenna arrays [10–18]. A new aperture is proposed in [10] microstrip antenna array. The an-

Manuscript received May 6, 2018 ; Revised August 2, 2018 ; Accepted November 22, 2018. (ID No. 20180506-036J)

Department of Communication Engineering, School of Electronics Engineering (SENSE), Vellore Institute of Technology, Vellore, Tamil Nadu, India.

*Corresponding Author: Venkata Kishore Kothapudi (e-mail: v.k.kothapudi@ieee.org)

This is an Open-Access article distributed under the terms of the Creative Commons Attribution Non-Commercial License (<http://creativecommons.org/licenses/by-nc/4.0>) which permits unrestricted non-commercial use, distribution, and reproduction in any medium, provided the original work is properly cited.

© Copyright The Korean Institute of Electromagnetic Engineering and Science. All Rights Reserved.

antenna consists of 100×50 planar array microstrip elements with an inter-element spacing of 0.51λ , and a -20.9 dB SLL is obtained. In [11], the authors presents a SLL suppression method for an X-band antenna array by designing a novel feeding network with a Chebyshev distribution. The array operates at 9.3 GHz and can give a -19.4 dB SLL, and the gain is only 12.3 dBi. A linear series-fed six-element antenna array is presented in [12]. A 6.5% wideband is obtained, but the SLL and the acquired gain remain poor at -20 dB and 14.2 dBi, respectively. Lower SLLs are dealt with and obtained in [13, 14]. The optimized distribution coefficients through the differential evolution algorithm have been used to achieve a wideband and a lower SLL in the slot antenna with a series-fed network in [13]. The antenna has 10 elements arranged in a series feeding system. The SLL and the half-power beamwidth (HPBW) are -25.3 dB and 8.4° , respectively. However, the gain is only 14.5 dBi. In addition, Nikkhah et al. [14] propose a low SLL and wideband series-fed antenna for the dielectric resonator (DRA). The proposed antenna can achieve a very low -30 dB SLL and a high 19 dBi gain. A 22×1 linear array results in a large size and fabrication complexity. Similarly, two other DRA arrays are introduced in [15, 16]. The array in [15] works at 60 GHz and that in [16] operates at 7.4 GHz. The SLLs are -27.7 dB and -23 dB, respectively. In [17, 18], two linear series-fed Yagi-like array samples are presented. The arrays have 22 similar Yagi line elements, which can provide a gain of 15.3 dBi and an SLL of about -27 dB. A literature comparison is presented in [13–16, 19–21] for both uniform and Chebyshev amplitude distributions (CAD).

In this study, a series-fed center-fed open-stub (SFCFOS)

uniform amplitude distribution (UAD) and Chebyshev amplitude distribution (CAD) linear arrays are designed and applied to achieve a SLL of -25 dB and gain enhancement. Two series-fed linear array antennas with UAD and CAD at the same operating frequency are fabricated, and scattering parameters and radiation characteristics are measured. The amplitude can be controlled by varying the patch width that has been implemented. A $\lambda_g/2$ open-ended stub is introduced at both the ends of the array, so that the energy remaining after the last element is reflected from the open stub and radiates into the space.

II. ANTENNA ARRAY STRUCTURE AND DESIGN

This section introduces a design process of two types of antenna arrays with different configurations. In addition, uniform linear array (ULA) and Chebyshev linear array (CLA) antenna arrays using the corresponding linear polarized—antenna elements are also presented. Here, we define the xz -plane as the vertical plane (E-plane or $\phi = 0^\circ$) and yz -plane as the horizontal plane (H-plane or $\phi = 90^\circ$). The whole design is analyzed with the aid of the full-wave electromagnetic solver CST Microwave Studio (CST Computer Simulation Technology GmbH, Darmstadt, Germany).

Fig. 1 shows the top and bottom views of the geometry of the UAD and CAD linear array antennas, respectively. The antenna is composed of a microstrip patch array, a series feed, and coaxial probe center-feed structures (substrate and Brass plate). Both arrays are designed with 31 mil with 1 oz., that is, a 0.035 mm-thick copper RT/Duroid-5880 (Rogers Corp., Chandler, AZ, USA) copper cladding substrate with relative permittivity ϵ_r ,

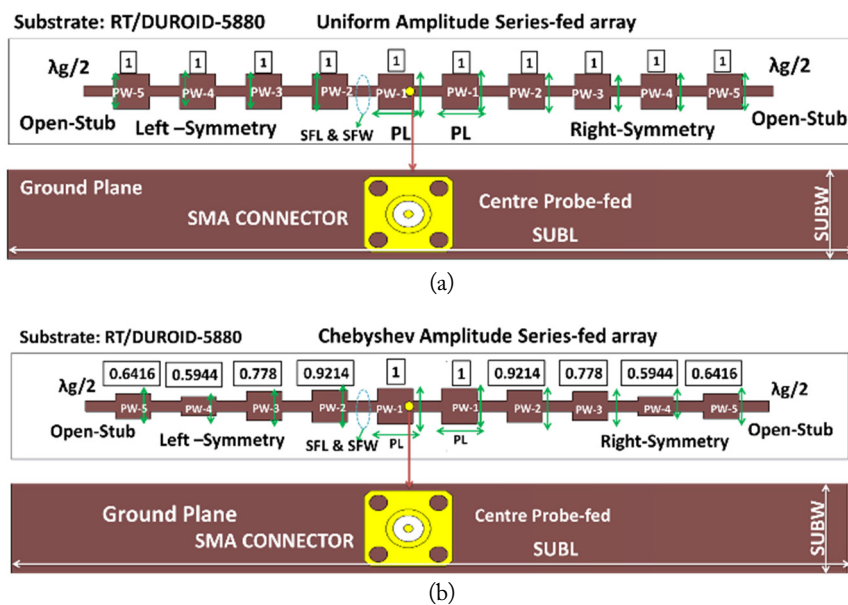


Fig. 1. Geometry of the configuration with optimized dimensions: (a) 10-element series-fed uniform linear array and (b) 10-element series-fed Chebyshev linear array.

= 2.2, and the loss tangent $\tan\delta = 0.0009$ is chosen as the substrate material. After the fabrication of the antenna, we perform gold plating over the patch and the ground copper layer of 1- μ m thickness for the ULA and silver plating for the CLA. Then, an antenna mounting plate with brass material of 0.8 mm thickness is mechanically fabricated and used to mount the antenna PCB using M2 (M-Metric Standard) stainless steel screws. The height of the antenna becomes 1.6 mm (electrical dimensions = $0.158\lambda_g$), which corresponds to the center frequency of 21 GHz. The optimized parameters are given in Table 1.

In the SFCFOS array design, a uniform characteristic with a constant SLL of -13 dB and a Chebyshev characteristic of -25 dB is chosen. To obtain a flat SLL performance, we use amplitude coefficients modified from an ordinary Chebyshev synthesis and introduce a half-wavelength open-ended stub after the last element for an effective utilization of transmitted power. The width of the center patch is 5 mm. The patch width of the other elements is variable, with a ratio of 1, 0.9214, 0.778, 0.5944, and 0.6412 from the array center to the edges. The distance between two adjacent elements is 4.28 mm ($0.7\lambda_0$ at 21 GHz). The whole size of the proposed ULA and CLA antenna arrays are 120 mm (L) \times 15 mm (W) \times 1.587 mm (H) and 100 mm (L) \times 15 mm (W) \times 0.787 mm (H), respectively. The array factor of the series array for an even number of elements can be written as (1):

$$(AF)_{2M} = \sum_{n=1}^M a_n \cos(2n-1)\psi \quad (1)$$

$$\because \psi = kd \cos(\theta)\psi$$

Table 1. Optimized parameters of a 10-element linear array

Parameter	Value (mm)	λ_0	λ_g
10-element ULA			
PL	5	0.352	0.496
PW-1 to PW-5	5	0.352	0.496
SFL	4.28	0.301	0.424
SFW	1.5	0.105	0.148
10-element CLA			
PL	5	0.352	0.496
PW-1	5	0.352	0.496
PW-2	4.6	0.323	0.456
PW-3	4.15	0.292	0.411
PW-4	2.75	0.193	0.272
PW-5	3.5	0.246	0.347
SFL	4.28	0.301	0.424
SFW	1.5	0.105	0.148

λ_0 = free space wavelength with respect to the velocity of propagation in the air center frequency (21 GHz) (0.0142 m), λ_g = guided wavelength with respect to the velocity of propagation in the substrate material (RT/Duroid-5880) (0.01008 m), PL = length of the patch, PW = width of the patch, SFL = length of the series-fed line, SFW = width of the series-fed line.

$$\psi = \frac{2\pi}{\lambda} 0.7\lambda \cos(\theta)$$

Let $M = 5$

$$(AF)_{10} = a_1 \cos(\psi) + a_2 \cos(3\psi) + a_3 \cos(5\psi) + a_4 \cos(7\psi) + a_5 \cos(9\psi).$$

III. FABRICATED AND MEASURED RESULTS

The proposed ULA and CLA antenna arrays are fabricated and measured. Fig. 2 presents a photograph of the fabricated antenna arrays showing the ULA and CLA antenna arrays assembled with a brass plate and stainless steel screws. The measured return loss of the ULA and CLA antenna arrays is performed with the Agilent N9918A FieldFox microwave analyzer. The radiation patterns and gains of the antenna array are measured using a far-field measurement technique in a microwave anechoic chamber with the Agilent PNA Series Network Analyzer N5230C (10 MHz–40 GHz).

1. Impedance Bandwidth

The uniform and Chebyshev 10-element series-fed linear arrays are fabricated and measured to validate the design. Fig. 2 shows the prototype array antenna for K-band applications. The measurement setup for both S -parameters and radiation patterns are shown in Fig. 3. The simulated structure using the CST Microwave Studio Simulator shows the electric field distribution illustrated in Fig. 4. The measured return loss $|S_{11}|$ of the proposed K-band 10-element series-fed uniform and Che-

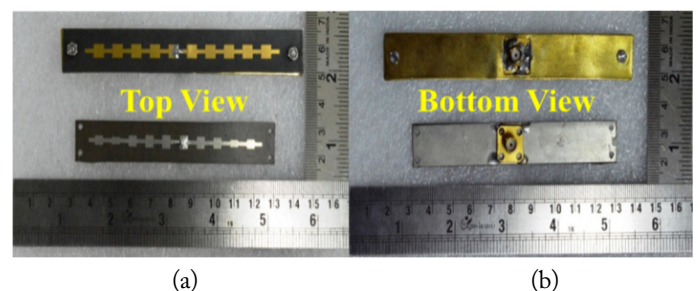


Fig. 2. Photograph of the fabricated prototypes: (a) Top view of the ULA and CLA and (b) Bottom view of the ULA and CLA.

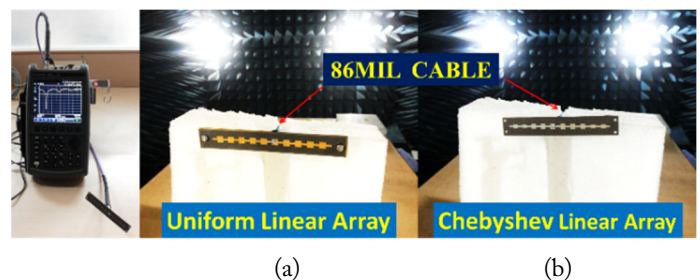


Fig. 3. S -parameters and radiation pattern measurement setup: (a) ULA and (b) CLA.

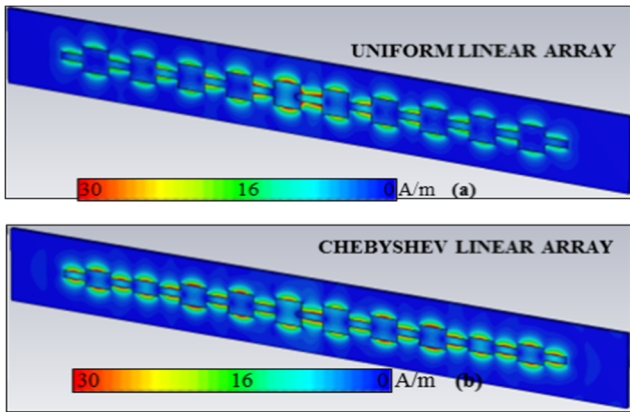


Fig. 4. (a) Uniform amplitude distribution–surface current distribution at 21 GHz and (b) Chebyshev amplitude distribution–surface current distribution at 21 GHz.

Chebyshev linear arrays is presented in Fig. 5. The measured -10 dB impedance bandwidth varies at 20.912–21.192 GHz (1.33%) for the uniform array and at 20.89–21.196 GHz (1.45%) for the Chebyshev array with a resonant frequency of 21 GHz for each design.

2. Radiation Characteristics

Figs. 6 and 7 show the radiation performance of the simulated and measured results of ULA and CLA, respectively, for the K-band. The radiation is a linear vertical polarization with a

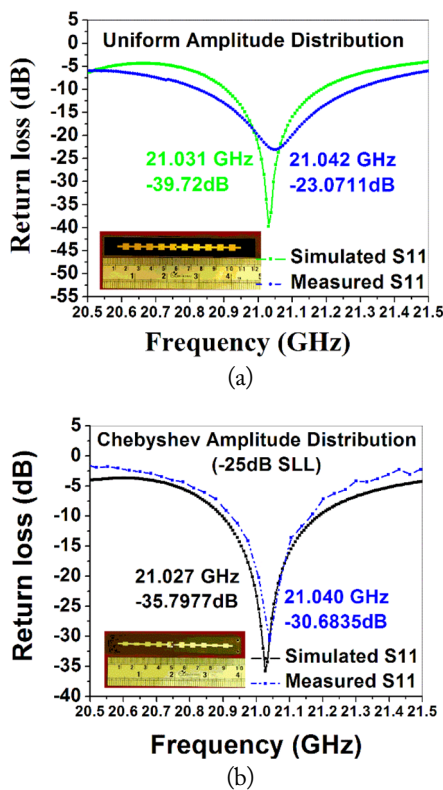


Fig. 5. Simulated and measured reflection coefficients: (a) ULA and (b) CLA.

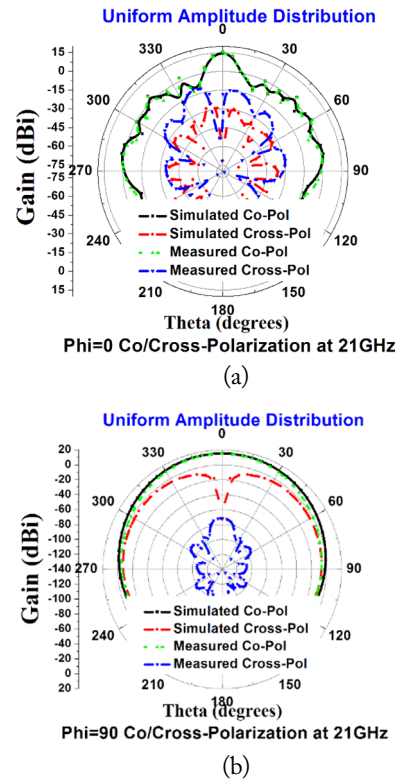


Fig. 6. Simulated and measured radiation patterns for the ULA at 21 GHz: (a) $\phi = 0^\circ$ E-plane (co-pol and cross-pol) and (b) $\phi = 90^\circ$ H-plane (co-pol and cross-pol).

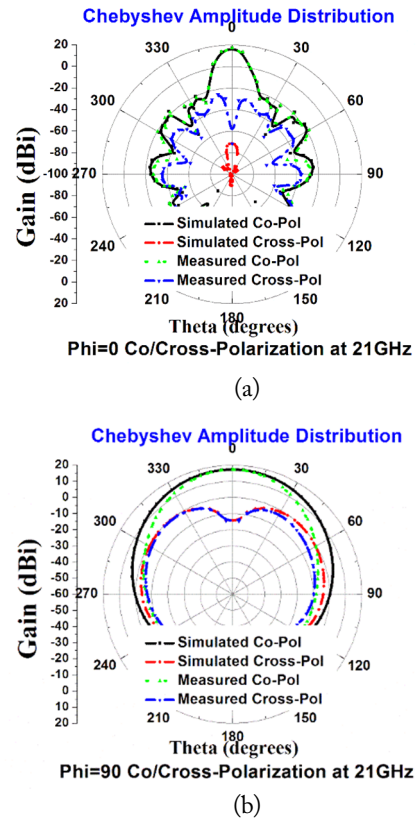


Fig. 7. Simulated and measured radiation patterns for the CLA at 21 GHz: (a) $\phi = 0^\circ$ E-plane (co-pol and cross-pol) and (b) $\phi = 90^\circ$ H-plane (co-pol and cross-pol).

high front-to-back ratio and a highly symmetric profile in both the $x-z$ and $y-z$ planes.

For the ULA design, the measured antenna gain is 15.3 dBi with HPBW of 10.4° and 64.4° for the $\phi = 0^\circ$ (E-plane) and $\phi = 90^\circ$ (H-plane), respectively. The maximum SLLs are -10.4 dB and -26.4 dB for the $\phi = 0^\circ$ (E-plane) and $\phi = 90^\circ$ (H-plane) in the case of ULA. For the CLA design, the measured antenna gain is 17.4 dBi with HPBW of 9.1° and 64.9° for the E-plane and H-plane, respectively. The maximum SLLs are -26.3 dB and -26.3 dB for the E-plane and H-plane, respectively, in the case of CLA. From the measured results, the SLL reduction of greater than -12 dB and gain enhancement of greater than 2 dBi can be obtained simultaneously. The simulated radiation efficiency and the measured and simulated realized gains are shown in Fig. 8 for both the ULA and CLA arrays. Fig. 9 shows the 3D far-field gain. The results agree well with the simulated and measured antenna parameters. The radi-

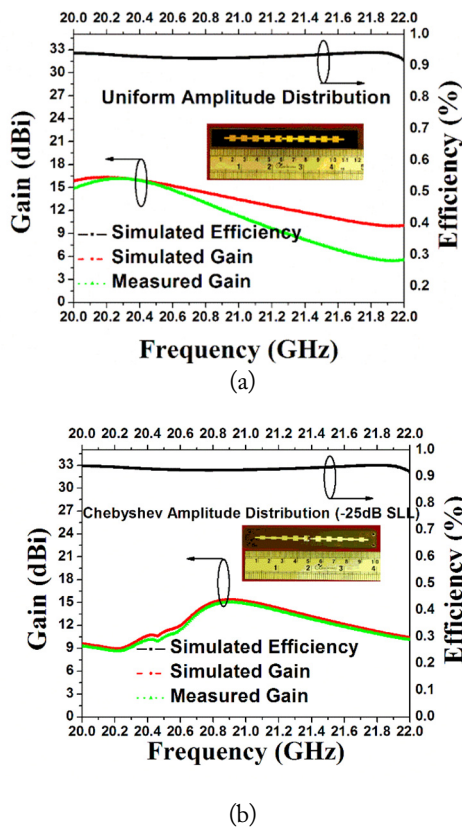


Fig. 8. Simulated radiation efficiency and measured gain: (a) ULA and (b) CLA.

Table 2. Comparison with the uniform amplitude distribution

Ref.	Year	No. of elements	SLL (dB)	HPBW (°)	Resonant frequency (GHz)	Gain (dBi)	Beam scan range (°)
[19]	2004	1 × 4	-9	25	2	8.7	20
[20]	2007	1 × 5	-10	N/A	5.8	11.3	22
[21]	2010	1 × 8	-10	N/A	2	N/A	25
This work	-	1 × 10	-25	10.4	21	15.3	25

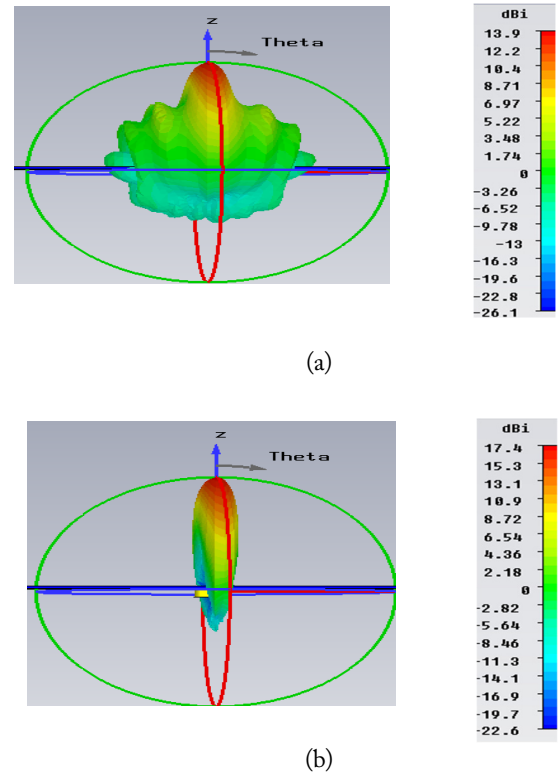


Fig. 9. Simulated 3D far-field gain: (a) $\phi = 0^\circ$ (E-plane) ULA at 21 GHz and (b) $\phi = 0^\circ$ (E-plane) CLA at 21 GHz.

tion discrepancies between the simulation and the measurement are attributed to the fabrication errors. UAD and CAD has been compared with literature in Table 2.

The results of this work are compared with those in the literature in Table 3. The proposed array has a gain of 17.4 dBi with the same number of elements, and it is higher than that in [13] with only 14.5 dBi and in [15] with approximately 15.7 dBi. In this work, the SLL is 1 dBi higher than that in [13] and 3 dB higher than that in [15]. Compared with that in [16], the antenna has better gains and SLL results.

IV. CONCLUSION

A novel SFCFOS antenna design for K-band radar applications is presented in this letter. The antenna structure shows a high gain performance and a low sidelobe level with a conformal size. The measured results are in good agreement with the simulated ones with gains of 15.3 dBi and 17.4 dBi, respectively.

Table 3. Comparison with the Chebyshev amplitude distribution

Ref.	Year	No. of elements	SLL (dB)	HPBW (°)	Resonant frequency (GHz)	Gain (dBi)	Beam scan range (°)
[14]	2013	1 × 22	-30	NA	9.2	19	NA
[15]	2016	1 × 10	-27.5	NA	60	15.7	NA
[16]	2017	1 × 8	-23.1	NA	7.54	15.7	NA
[13]	2017	1 × 10	-25.3	8.3	9	14.5	NA
This work	-	1 × 10	-26.3	9.1	21	17.4	25

The gain enhancement greater than 1.5 dBi can be obtained with an SLL of -25 dB using the CLA with 10 elements in the operating frequency band of 20.9–21.19 GHz. The HPBWs for the CLA/ULA at both E-plane and H-plane are 9.1°/10.4° and 64.4°/64.9°, respectively. With these advantages, the proposed antenna array is a good candidate for use in radar systems.

REFERENCES

- [1] W. Menzel, "A 40 GHz microstrip array antenna," in *Proceedings of IEEE MTT-S International Microwave Symposium Digest*, Washington, DC, 1980, pp. 225–226.
- [2] T. Metzler, "Microstrip series arrays," *IEEE Transactions on Antennas and Propagation*, vol. 29, no. 1, pp. 174–178, 1981.
- [3] Y. B. Jung, I. Yeom, and C. W. Jung, "Centre-fed series array antenna for K-/Ka-band electromagnetic sensors," *IET Microwaves, Antennas & Propagation*, vol. 6, no. 5, pp. 588–593, 2012.
- [4] M. Hajian, J. Zijderveld, A. A. Lestari, and L. P. Ligthart, "Analysis, design and measurement of a series-fed microstrip array antenna for X-band INDRA: the Indonesian maritime radar," in *Proceedings of the 3rd European Conference on Antennas and Propagation*, Berlin, Germany, 2009, pp. 1154–1157.
- [5] J. Hautcoeur, E. M. Cruz, J. Bartholomew, J. Sarrazin, Y. Mahe, and S. Toutain, "Low-cost printed antenna array built with hybrid feed for urban microwave links," *IET Microwaves, Antennas & Propagation*, vol. 4, no. 9, pp. 1320–1326, 2010.
- [6] H. Iizuka, K. Sakakibara, T. Watanabe, K. Sato, and K. Nishikawa, "Millimeter-wave microstrip array antenna with high efficiency for automotive radar systems," *R&D Review of Toyota CRDL*, vol. 37, no. 2, pp. 7–12, 2002.
- [7] M. Barba, "A high-isolation, wideband and dual-linear polarization patch antenna," *IEEE Transactions on Antennas and Propagation*, vol. 56, no. 5, pp. 1472–1476, 2008.
- [8] B. Lee, S. Kwon, and J. Choi, "Polarisation diversity microstrip base station antenna at 2 GHz using t-shaped aperture-coupled feeds," *IEE Proceedings-Microwaves, Antennas and Propagation*, vol. 148, no. 5, pp. 334–338, 2011.
- [9] B. Li, Y. Z. Yin, W. Hu, Y. Ding, and Y. Zhao, "Wide-band dual-polarized patch antenna with low cross polarization and high isolation," *IEEE Antennas and Wireless Propagation Letters*, vol. 11, pp. 427–430, 2012.
- [10] J. Xiao, G. Dong, and M. Zhu, "A novel aperture coupled microstrip antenna array with low cross-polarization, low sidelobe and backlobe," in *Proceedings of the 4th International Conference on Microwave and Millimeter Wave Technology (ICMMT)*, Nanjing, China, 2004, pp. 223–226.
- [11] Y. P. Saputra, F. Oktafiani, Y. Wahyu, and A. Munir, "Side lobe suppression for X-band array antenna using Dolph-Chebyshev power distribution," in *Proceedings of the 22nd Asia-Pacific Conference on Communications (APCC)*, Yogyakarta, Indonesia, 2016, pp. 86–89.
- [12] C. Niu, J. She, and Z. Feng, "Design and simulation of linear series-fed low-sidelobe microstrip antenna array," in *Proceedings of the Asia-Pacific Microwave Conference (AP-MC)*, Bangkok, Thailand, 2007, pp. 1–4.
- [13] J. Yin, Q. Wu, C. Yu, H. Wang, and W. Hong, "Low sidelobe-level series-fed microstrip antenna array of unequal interelement spacing," *IEEE Antennas and Wireless Propagation Letters*, vol. 16, pp. 1695–1698, 2017.
- [14] M. R. Nikkhah, J. Rashed-Mohassel, and A. A. Kishk, "A low sidelobe and wideband series-fed dielectric resonator antenna array," in *Proceedings of the 21st Iranian Conference on Electrical Engineering (ICEE)*, Mashhad, Iran, 2013, pp. 1–3.
- [15] W. Shen, J. Lin, and K. Yang, "Design of a V-band low sidelobe and wideband linear DRA array," in *Proceedings of the Progress in Electromagnetic Research Symposium (PIERS)*, Shanghai, China, 2016, pp. 477–480.
- [16] J. Lin, W. Shen, and K. Yang, "A low-sidelobe and wideband series-fed linear dielectric resonator antenna array," *IEEE Antennas and Wireless Propagation Letters*, vol. 16, pp. 513–516, 2017.
- [17] R. Bayderkhani and H. R. Hassani, "Wideband and low sidelobe linear series fed Yagi-like antenna array," *Progress In Electromagnetics Research*, vol. 17, pp. 153–167, 2009.
- [18] R. Bayderkhani and H. R. Hassani, "Wideband and low sidelobe slot antenna fed by series-fed printed array," *IEEE Transactions on Antennas and Propagation*, vol. 58, no. 12, pp. 3898–3904, 2010.

- [19] A. Tombak and A. Mortazawi, "A novel low-cost beam-steering technique based on the extended-resonance power-dividing method," *IEEE Transactions on Microwave Theory and Techniques*, vol. 52, no. 2, pp. 664–670, 2004.
- [20] E. Ojefors, S. Cheng, K. From, I. Skarin, P. Hallbjorner, and A. Rydberg, "Electrically steerable single-layer microstrip traveling wave antenna with varactor diode based

phase shifters," *IEEE Transactions on Antennas and Propagation*, vol. 55, no. 9, pp. 2451–2460, 2007.

- [21] D. Ehyae and A. Mortazawi, "A new approach to design low cost, low complexity phased arrays," in *Proceedings of IEEE MTT-S International Microwave Symposium Digest*, Anaheim, CA, 2010, pp. 1270–1273.

Venkata Kishore Kothapudi (S, 14 M, 2018)



was born in Tenali Town, Guntur district, Andhra Pradesh, India, in 1987. He received a degree in Electronics and Communication Engineering from TPIST, JNTU, Hyderabad, India, in 2008 and M.Tech. degree in Communication and Radar Systems from the Koneru Lakshmaiah Education Foundation (KLEF), India, in 2012. He is currently pursuing a Ph.D. degree with the Microwave Division, department of Communication Engineering, School of Electronics Engineering (SENSE), Vellore Institute of Technology (VIT), Vellore, Tamil Nadu India. He has more than 7+years of Research and Industry experience in RF and Microwave engineering in ECIL as a GEA, in NARL-ISRO as a project student, Astra Microwave Products as an Engineer, Research Associate and Teaching Cum and Research Associate in Microwave Division, department of Communication Engineering, School of Electronics Engineering (SENSE), Vellore Institute of Technology (VIT). He has rich experience in radar systems design, which includes transmit/receive modules (HF, VHF, L, S, and C-Band), RF and microwave feeder network and beam forming, RF and microwave active and passive components, RF power amplifiers, and antenna systems, which include Yagi-Uda and microstrip patch antenna as a phased array with different configurations using analysis and synthesis techniques. He has published more than 15 research papers in international journals and national and IEEE international conferences. He has been the author and co-author of many IEEE Proceedings papers. He has published research papers in *IEEE Access*, with a 3.557 impact factor; the *Progress in Electromagnetic Research (PIER)* international journal, *Journal of Electromagnetic Engineering and Science (JEES)*, and IEEE international conferences. He is reviewer for several reputed journals (IEEE Access, JEES, ACES, Advanced Electromagnetics JESTR.) He travelled to Sri Lanka and Singapore for the IEEE SYWC 2015 meeting and the IEEE APSAR 2015 conference, respectively, to present his research work and as a part of his research. His research interests include Shared Aperture Antenna Technology (Single-Layer and Multi-Layer-P/L/S/C/X/Ku/K/Ka-bands) for Radar Engineering, Airborne and Space borne Synthetic Aperture Radar, and Radar Wind Profilers. He is a member of Institute of Electrical and Electronics Engineering (IEEE), American Institute of Aeronautics and Astronautics (AIAA), and Applied Computational Electromagnetics Society (ACES). He is associated with IEEE societies (AP-s., MTT-s., AES-s., GRS-s., IP-s., ComSoc & EMC-s.).

received his M.Sc. degree in electronics from the Magadh University, India, in 2003. He obtained his M.Tech. degree in microwave remote sensing systems from BIT Mesra, Ranchi, in 2005 and his Ph.D. in microwave system engineering from IIT Bombay, Mumbai, in 2011. He worked as research associate in IIT Bombay and focused on Synthetic Aperture Radar interferometry and polarimetry for snow and ice studies in the Himalayas. He worked as a scientist investigator sponsored by the DST Government of India at CSRE, IIT Bombay in 2009–2013. He was a visiting researcher at Earth Observation Group, Northern Research Institute in 2009–2010. Kumar is an associate professor at the School of Electronics Engineering, VIT University and Vellore, TN, India beginning from 2013 until the present. He is associated with the photonics and microwave group at VIT. His research interests are microwave imaging and radar and SAR imaging system development and applications in Earth observation and reconnaissance from spaceborne, airborne, and UAV platforms. He is the author and contributing author of more than 20 SCI peer-reviewed papers and 30 conference proceedings on radiating system designs for radar applications, miniaturized antenna design using metamaterials, and MIMO antenna systems for UWB applications with reconfigurable notch band characteristics. He worked on active devices such as LNA and PAs for the UHF-range wind profiler radars. He completed two Ph.D. guidelines on MTM loaded antenna design and shared aperture beamforming array for radar applications. He guided five M.Tech theses on antenna design area. He completed three funded projects on antennas for radar applications, SAR processing, and multi-aperture SAR interferometry techniques. His current research interests are microwave active and passive device designs, THz antennas, and trans-receiver system for automotive radar applications. He is a life member of Indian Society of Remote Sensing (ISRS) and International Society for Optics and Photonics (SPIE) and is actively associated with IEEE societies Antennas and Propagation Society (APS), Tera Hertz (THz), and Geoscience and Remote Sensing (GRSS).

Vijay Kumar (S'07-M'11-SM'18)



received his M.Sc. degree in electronics from the Magadh University, India, in 2003. He obtained his M.Tech. degree in microwave remote sensing systems from BIT Mesra, Ranchi, in 2005 and his Ph.D. in microwave system engineering from IIT Bombay, Mumbai, in 2011. He worked as research associate in IIT Bombay and focused on Synthetic Aperture Radar interferometry and polarimetry for snow and ice studies in the Himalayas. He worked as a scientist investigator sponsored by the DST Government of India at CSRE, IIT Bombay in 2009–2013. He was a visiting researcher at Earth Observation Group, Northern Research Institute in 2009–2010. Kumar is an associate professor at the School of Electronics Engineering, VIT University and Vellore, TN, India beginning from 2013 until the present. He is associated with the photonics and microwave group at VIT. His research interests are microwave imaging and radar and SAR imaging system development and applications in Earth observation and reconnaissance from spaceborne, airborne, and UAV platforms. He is the author and contributing author of more than 20 SCI peer-reviewed papers and 30 conference proceedings on radiating system designs for radar applications, miniaturized antenna design using metamaterials, and MIMO antenna systems for UWB applications with reconfigurable notch band characteristics. He worked on active devices such as LNA and PAs for the UHF-range wind profiler radars. He completed two Ph.D. guidelines on MTM loaded antenna design and shared aperture beamforming array for radar applications. He guided five M.Tech theses on antenna design area. He completed three funded projects on antennas for radar applications, SAR processing, and multi-aperture SAR interferometry techniques. His current research interests are microwave active and passive device designs, THz antennas, and trans-receiver system for automotive radar applications. He is a life member of Indian Society of Remote Sensing (ISRS) and International Society for Optics and Photonics (SPIE) and is actively associated with IEEE societies Antennas and Propagation Society (APS), Tera Hertz (THz), and Geoscience and Remote Sensing (GRSS).



Important Dates

- Abstract submission deadline **January 4, 2019**
- Notification of acceptance **February 1, 2019**
- IEEE compliant abstract due **February 22, 2019**
- Advance registration ends **March 31, 2019**

Preparation of Abstracts

Prospective authors are invited to submit a 2-page abstract of the work to be reported including as many details as possible. The inclusion of figures, tables and especially numerical data is strongly recommended.

- Abstracts submission link: <http://ivec2019.org>

Technical Subject Categories

1. **Vacuum Electron Devices**
 - Traveling-wave tubes (all types)
 - Crossed-field devices (oscillators and amplifiers)
 - Klystrons
 - Multiple-beam devices
 - Inductive output tubes
 - Fast-wave devices (gyrotrons, gyro-amplifiers)
 - Free electron lasers and masers
 - Pulse compression devices
 - Plasma filled amplifiers and oscillators
 - High power microwave devices / RF directed energy
 - Triodes, tetrodes and pentodes
 - Power switches
2. **Vacuum Microelectronics / Nanoelectronics**
 - Microwave, millimetre-wave & THz amplifiers and oscillators
 - Field emitter arrays
 - Flat panel displays
 - Sensors and detectors
3. **Systems and Subsystems**
 - Microwave and millimeter-wave power modules
 - Electronic power conditioners, modulators, and supplies
 - Linearizers
 - Amplifier/antenna coupling
 - Power combining system
 - Device and system integration
 - Reliability
4. **Technologies**
 - Cathodes and other electron emitters
 - Component parts (e.g. guns, circuits, windows, collectors)
 - Analysis and computer modeling
 - Micro-fabrication techniques (e.g. LIGA, DRIE, 3-D printing, CNC)
 - Novel materials (e.g. dielectrics, coatings, magnetic materials)
 - Electron emission
 - RF breakdown
 - Linearity, intermodulation and noise
 - Novel measurement techniques
 - Miniaturization
 - Thermal power management and control
5. **Applications of Vacuum Electron Devices**
 - Defense
 - Radar
 - Telecommunications
 - Medicine
 - Particle accelerators
 - Nuclear fusion
 - Plasma
 - RF interference
 - Instruments and lithography
 - Materials processing
 - Television
 - Displays
 - Electric propulsion

Technical Program Committee

Jin Joo	Choi (Co-Chair)	Kwangwoon University	Korea
EunMi	Choi (Co-Chair)	Ulsan National Institute of Science and Technology	Korea
Kangwook	Kim (KIEES Liaison)	Gwangju Institute of Science and Technology	Korea
David K.	Abe	U.S. Naval Research Laboratory	USA
Young-soon	Bae	National Fusion Research Institute	Korea
Tsun-Hsu	Chang	National Tsing Hua University	Taiwan
Jun	Chen	Sun Yat-sen University	China
Boklae	Cho	Korea Research Institute of Standards and Science	Korea
Heungsik	Choi	LG Electronics Inc.	Korea
Zhaoyun	Duan	University of Electronic Science and Technology of China	China
Jinjun	Feng	Beijing Vacuum Electronics Research Institute	China
S.K.	Ghosh	Central Electronic Engineering Research Institute	India
Seong-Tae	Han	Korea Electrotechnology Research Institute	Korea
Min Sup	Hur	Ulsan National Institute of Science and Technology	Korea
John	Jelonnek	Karlsruhe Institute of Technology	Germany
Jung-Il	Kim	Korea Electrotechnology Research Institute	Korea
Jung Ho	Kim	LIG Nex1 Co., Ltd.	Korea
Shin	Kubo	National Institute for Fusion Science	Japan
Byung-Joon	Lee	Pohang Accelerator Laboratory	Korea
Hae June	Lee	Pusan National University	Korea
Woosang	Lee	Agency for Defense Development	Korea
Kartikeyan	Machavaram	Indian Institute of Technology Roorkee	India
Sun-Hong	Min	Korea Institute of Radiological & Medical Sciences	Korea
Masayoshi	Nagao	National Institute of Advanced Industrial Science and Technology	Japan
Hae-Yun	Park	Vitro Tech	Korea
Kyu Chang	Park	Kyung Hee University	Korea
Seong Hee	Park	Korea University	Korea
Nikita M.	Ryskin	Saratov Branch, Institute of Radio Engineering and Electronics, Russian Academy of Sciences	Russia
Young-Min	Shin	Communications & Power Industries LLC	USA
Jagadishwar	Sirigiri	Bridge 12 Technologies Inc.	USA
Heather	Song	University of Colorado at Colorado Springs	USA
David R.	Whaley	L-3 Communications, Electron Devices Division	USA
Moohyun	Yoon	Pohang University of Science and Technology	Korea

International Advisory Committee

Gun-Sik	Park (Chair)	Seoul National University	Korea
John	Booske	University of Wisconsin - Madison	USA
Moohyun	Cho	Pohang University of Science and Technology	Korea
EunHa	Choi	Kwangwoon University	Korea
Jin Soo	Choi	Agency for Defense Development	Korea
Mikhail	Glyavin	Institute of Applied Physics Russian Academy of Sciences	Russia
Lee-Ho	Hwang	Vitro Tech	Korea
Toshitaka	Idehara	University of Fukui	Japan
Shenggang	Liu	University of Electronic Science and Technology of China	China
Yeong-Kook	Oh	National Fusion Research Institute	Korea
Claudio	Paoloni	Lancaster University	UK
Etl	Schamiloglu	University of New Mexico	USA
R. K.	Sharma	Central Electronic Engineering Research Institute	India
Hyyong	Suk	Gwangju Institute of Science and Technology	Korea
Richard	Temkin	Massachusetts Institute of Technology	USA
Manfred	Thumm	Karlsruhe Institute of Technology	Germany

EDS Vacuum Electronics Technical Committee

Claudio Paoloni (Chair)	Lancaster University	United Kingdom
David K. Abe	Naval Research Laboratory	USA
Natanael Aylon	European Space Agency, ESA/ESTEC	The Netherlands
Monica Blank	Communications & Power Industries LLC	USA
John Booske	University of Wisconsin - Madison	USA
Yaogen Ding	Institute for Electronics, CAS	China
Jinjun Feng	Beijing Vacuum Electronics Research Institute	China
Dan M. Goebel	Jet Propulsion Laboratory, NASA	USA
John Jelonnek	Karlsruhe Institute of Technology	Germany
Baruch Levush	Naval Research Laboratory	USA
Neville C. Luhmann Jr.	University of California Davis	US
Machavaram Kartikeyan	Indian Institute of Technology Roorkee	India
William L. Menninger	L-3 Communications, Electron Technologies Inc.	USA
Gun-Sik Park	Seoul National University	Korea
Nikita M. Ryskin	Saratov Branch, Institute of Radio Engineering and Electronics, Russian Academy of Sciences	Russia
Jagadishwar R. Sirigiri	Bridge 12 Technologies Inc.	USA
Heather Song	University of Colorado at Colorado Springs	USA
Philippe Thouvenin	Thales Electron Devices	France
Jack Tucek	Northrop Grumman Corporation	USA
David R. Whaley	L-3 Communications, Electron Devices Division	USA
Dev Palmer	Lockheed Martin, Advanced Technology Laboratory	USA
Manfred Thumm	Karlsruhe Institute of Technology	Germany
Richard True	L-3 Communications, Electron Devices Division	USA

Instructions for Authors

Journal of Electromagnetic Engineering and Science (J. Electromagn. Eng. Sci.; JEES) is an official English journal of the Korean Institute of Electromagnetic and Engineering Science (KIEES). The objective of *JEES* is to publish academic as well as industrial research results and findings on electromagnetic engineering and science. The journal covers all aspects of researches and technology related to electromagnetics: Electromagnetic Compatibility/Electromagnetic Interference, Microwave and Millimeter-Wave Engineering, Antenna and Propagation, Electromagnetic Theory, Wireless Communication, Lightwave and Electro-Optics, Materials and Components, Software Defined Radar, Radar, Bioelectromagnetics, and etc.

I. Copyright and Creative Commons Attribution Licensing

The copyright and the transfer rights of the digital content of published papers and the journal is owned by the KIEES. All published materials are also assigned a Creative Commons Attribution License (<http://creativecommons.org/licenses/by-nc/4.0/>). The journal accepts manuscripts for consideration with the understanding that the manuscript has not been published previously and is not currently under consideration for publication elsewhere, and in addition, that the authors (or their employer, if it holds the copyright) are authorizing the transfer of the copyright to the Institute when the manuscript is submitted. Author should check the copyright transfer conditions and forms at <http://www.jees.kr>.

II. Research and Publication Ethics

Research published in *JEES* must have followed institutional, national, and international guidelines. For policies on research and publication ethics that are not stated in these instructions, please refer to the *Committee on Publication Ethics (COPE) Guidelines* (<http://publicationethics.org/resources/code-conduct>).

1. Originality and Duplicate Publication

A manuscript submitted for publication in *JEES* should be an original work with technical values. It must not have been previously published and is not under consideration for publication elsewhere. *JEES* assumes that the materials submitted for its publications are properly available for general dissemination for the readership of those publications. It is the responsibility of the authors, not *JEES*, to determine whether disclosure of their materials requires prior consent of other parties and, if so, to obtain it. If an author uses charts, photographs, or other graphics from any previously printed materials, he/she is responsible for obtaining written permissions from the publisher to use them in his/her manuscript. Responsibility for the contents of published papers rests upon the authors, not *JEES*.

2. Conflict of Interest

Authors are required to complete a declaration of conflict of interests. All conflict of interests that are declared will be listed at the end of published articles.

3. Authorship

Authorship should be restricted to those individuals who have met each of the following three criteria:

1) made a significant contribution to the conception and design of the project, or the analysis and interpretation of the data, or other substantial scholarly effort; 2) participated in drafting, reviewing and/or revising the work; and 3) approved the final version for publication. After the initial submission of a manuscript, any changes whatsoever in authorship (adding author(s), deleting author(s), or re-arranging the order of authors) must be explained by a letter to the editor from the authors concerned. The content of this

letter must be acknowledged and agreed upon by all of the authors of the paper.

If you accept the policies on research and publication issued by KIEES, authors must click the response of “The Code of Research Ethics” through online.

III. Submission of Manuscripts

Authors are expected to be members of the KIEES except for some special cases approved by the Editorial Board of KIEES. All manuscripts should be submitted electronically through the online submission and review site (<https://mc03.manuscriptcentral.com/jees>). For the first submission, you may be required to create an account on the submission site. A manuscript can be submitted at any time of the year. When submitting a manuscript, authors need to make sure that their manuscripts do not provide any of their identities such as authors' names and affiliations as the review is double-blinded. More detailed submission instruction is available in the upper right corner of the submission site. All manuscripts submitted to the Journal must comply with the instruction and the standard format of the Journal. Otherwise, it will result in return of the manuscript and possible delay in publication. For assistance, please contact us via e-mail (admin-jees@kiees.or.kr).

IV. Peer Review Process

The manuscript will be forwarded to three reviewers selected for their expertise in the field of the submitted manuscript. The acceptance criteria for all papers are based on the quality and originality of the research and its clinical and scientific significance. During the review process, the author is often asked to expand, rewrite, or clearly explain the specific contents of his/her paper. It is not uncommon that an author is asked to provide another draft with the suggested changes for further review. A revised manuscript should be submitted to the homepage within a month from the date on which any change of the manuscript is requested to the author. Once a manuscript has received the final approval of the reviewers and Editor-in-Chief, the author will be notified and asked to prepare the manuscript for final publication and to possibly complete an additional information form.

V. Publication Type

The papers are classified into five categories.

Regular Paper should be an original work that contributes to the academic interests of the KIEES members with technical values. The paper should also be written within 12 pages with A4 size including figures, charts, and tables (The main body of text consists of two columns).

Letter consists of reports of preliminary results or short reports on completed work that are of current interest to many researchers in the field. Comments on material previously published in the journal, suggestions for new directions, and errata could be included. Their length must be less than 3 pages (with a two-column format) including paper title, author affiliation, reference, etc.

Review Paper will be published by direct submission as well as from invited experts. In both cases, the work will be subject to editorial review. Review papers should critically review topics not only to inform the reader of the background, but also to communicate the state of the art and outstanding research problems.

Technical Report is on innovative technical achievements of interest to the community and usually a report of an extensive series of measurements. Report is often involving display in the form of tables or graphs, with text describing the conditions and procedures of measurement.

Editorial is a brief report of research findings adequate for the journal's scope and of particular interest to the community.

VI. Manuscript Preparation

All manuscripts must be written in MS-Word and adhere to the following guidelines:

1. A cover of each paper manuscript should include a title, authors' names (main author and co-authors), author's organizations, contact information (e-mail and phone number), and the author's area of expertise.
2. The first page of a main text should only contain title, abstract with a length of about 150 words, and key words with around five words.
3. The contents of the manuscript should be arranged in the order of abstract, main text, acknowledgments, references, and appendix.
4. The numbers corresponding to chapters in the manuscript should be written in Roman numerals (I, II, III, IV...) and the numbers corresponding to sections should be written in Arabic numerals (1, 2, 3, 4...).
5. Equation numbers should be given in Arabic numerals enclosed in parentheses on the right-hand margin. They should be cited in the text as, for example Eq. (1) or Eqs. (1)-(3).
6. All tables should be numbered consecutively with Arabic numerals. They should be referred to in the text and should be numbered according to their order of mention in the text. In addition, all tables should, not only list all abbreviations in the table in footnotes at the end, but also have a title that is concise and describes the table's contents. Vertical lines are not used. The table should be self-explanatory and supplement, not duplicate, the text. If the table or any data therein have been published, a footnote to the table must give permission information to the original source. The structure should be clear, with simple column headings giving all units. A table should not exceed one page when printed. Use lowercase letters in superscripts ^{a,b,c...} for special remarks.
7. All figures should be of high quality meeting with the publishing requirement with legible symbols and legends. In preparing the figures, authors should consider a size reduction during the printing process to have acceptable line clarity and character sizes. Use only figures that are necessary to illustrate the meaning of the text. Figures must be black and white of high contrast. All figures should be referred to in the text as, for example, Fig. 1, Fig. 2(a), or Figs. 1-3.
8. Only those references cited in the text should be listed in the references. Authors are responsible for the accuracy and completeness of their references and the correct text citations. In the text the reference should be numbered in bracket in ascending order (e.g., [1, 3], or [4-6]; Lee [2] and Kim and Park [5]; Jang et al. [7]). In case of the paper title, only the first letter is to be capitalized. However, in case of journal and book titles, the first letter of each word should be capitalized and all of the letters should be italicized. See the example below.

Books

- [1] F. Giannini and G. Leuzzi, *Nonlinear Microwave Circuit Design*. NewYork, NY: John Wiley & Sons Inc., 2004.

Journals

- [2] H. Ahn and B. Kim, "Equivalent transmission-line sections for very high impedances and their application to branch-line hybrids with very weak coupling power," *Journal of Electromagnetic Engineering and Science*, vol. 9, no. 2, pp. 85-97, Jun. 2009.

Report

- [3] E. E. Reber, R. L. Michell, and C. J. Carter, "Oxygen absorption in the earth's atmosphere," Aerospace Corp., Los Angeles, CA, Tech. Rep. TR-0200 (4230-46)-3, Nov. 1988.

Conference Proceedings

- [4] S. P. Bingulac, "On the compatibility of adaptive controllers," in *Proceedings of the 4th Annual Allerton Conference on Circuit and System Theory*, NewYork, pp. 8-16, 1994.

Papers Presented at Conferences

- [5] J. G. Kreifeldt, "An analysis of surface-detected EMG as an amplitude-modulated noise," presented at the 8th International Conference on Medical and Biological Engineering, Chicago, IL, 1969.
- [6] J. Arrillaga and B. Giessner, "Limitation of short-circuit levels by means of HVDC links," presented at the IEEE Summer Power Meeting, Los Angeles, CA, Jul. 1990.

Theses (M.S.) and Dissertations (Ph.D.)

- [7] N. Kawasaki, "Parametric study of thermal and chemical nonequilibrium nozzle flow," M.S. thesis, Department of Electronic Engineering, Osaka University, Osaka, Japan, 1993.
- [8] J. O. Williams, "Narrow-band analyzer," Ph.D. dissertation, Department of Electronic Engineering, Harvard University, Cambridge, MA, 1993.

Standards

- [9] *IEEE Criteria for Class IE Electric Systems*, IEEE Standard 308, 1969.

Online Sources

- [10] R. Bartle, "Early MUD History," Nov. 1990; www.ludd.luth.se/aber/mud-history.html.

9. When citing any paper published in JEES, it should be indicated the name of the journal as *Journal of Electromagnetic Engineering and Science* or *J. Electromagn. Eng. Sci.*

10. Acknowledgment, if needed, appears before the reference. Sponsorship or financial support acknowledgment should be included here.

11. Unit and Abbreviation: If the authors describe length, height, weight, and volume, they should use standard metric units. Temperature should be given in degrees Celsius. All other units should follow the International System of Units (SI). All units must be preceded by one space except percentages (%) and temperatures (°C).

Abbreviations must be used as an aid to the reader, rather than as a convenience of the author, and therefore their use should be limited. Generally, abbreviations that are used less than 3 times in the text, including tables and figure legends, should be avoided. Standard SI abbreviations are recommended. Other common abbreviations are as follows (the same abbreviations are used for plural forms): h (hour), min (minute), s (second), d (day), wk (week), mo (month), y (year), L (liter), mL (milliliter), μ L (microliter), g (gram), kg (kilogram), mg (milligram), μ g (microgram), ng (nanogram), pg (picogram), g (gravity; not g), nm (nanometer), μ m (micrometer), mV (millivolt), mA (milliampere), mW (milliwatt), C (coulomb), μ F (microfarad), mH (millihenry), n (samplesize), SD (standard deviation of the mean), and SE (standard error of the mean).

VII. Accepted Manuscript

Once the review process has been completed with a decision of acceptance, the final manuscript accommodating all of the reviewers' comments should be submitted along with photos of the authors and their brief biographies (including major research areas). The accepted papers will be published, in principle, in the order of initially submitted dates subject to decision of the Editorial Board.

1. Page Proofs

Authors will be given an opportunity to review the laser printed version of their manuscripts before printing. One set of page proofs in PDF format will be sent by e-mail to the corresponding author. The review should be solely dedicated to detecting typographical errors.

2. Publishing Charge

The publishing charge for general publishing is KRW 150,000 (US\$150) for up to the first 6 pages. For 7 to 8 pages, an extra charge of KRW 30,000 (US\$30) per page, and for 9 pages or more, an extra charge of KRW 40,000 (US\$40) per page. Furthermore, the KIEES charges extra KRW 100,000 (US\$100) for the paper acknowledging a financial support from an institution, in addition to the above mentioned page charge. Twenty reprints without a cover will be supplied without an additional charge.

Contact Us

Editorial office of the Korean Institute of Electromagnetic Engineering and Science
217, Saechang-ro, Yongsan-gu, Seoul, 04376, Korea
Tel: +82-2-337-9666/332-9665 Fax: +82-2-6390-7550
<http://www.jees.kr>, E-mail: admin-jees@kiees.or.kr

AUTHOR CHECKLIST

Title : _____

General

- This paper has not been and will not be published in any other journal.
- This paper follows the format of the KIEES paper submission guideline, is less than 12 pages long, including figures and tables (3 pages for a letter), and has a two-column layout.
- This paper includes a cover page, an abstract, keywords, main text, appendix, and references in the correct order. Each page has a consecutive page number.

Cover page

- The cover page includes the title, authors, affiliation of all authors, identifier of the corresponding author, and provides contact information for the corresponding author (phone number, e-mail address, and mobile number).

Abstract and key words

- An abstract is provided and is less than 500 words long.
- Fewer than 5 keywords are provided.

Main text

- The reference number is written next to the quote.
- The chapter numbers are written in Roman numerals (I, II, III, IV...) and subheading numbers are written in Arabic numerals (1, 2, 3, 4...).

References

- Sufficient Korean as well as international literature is referenced in the paper.
- Only the references used in the main text are included in the reference list and these are numbered according to their order of appearance.
- All reference citations follow the correct format indicated in the submission regulations.

Figures and tables

- For the figures and tables, the first letter of the very first word is capitalized.
- All figure legends include both a title and a detailed explanation to help in understanding what the figure depicts.
- All tables are self-explanatory and do not repeat the content from figures or sources included in the main text.

* Check each box after confirming that the statement is true.

The authors of this paper have confirmed the above items, following the paper submission regulations of *the Korean Institute of Electromagnetic Engineering and Science (KIEES)*, and are requesting publication of this paper.

_____ / _____ / 2019

Representative author: _____ (signature)